Ph.D. Dissertation

In Vitro Study of Microtubule Deformation by External Stimuli and its Effect on the Interaction between Microtubule and Microtubule-Associated Motor Proteins

外部刺激による微小管の変形とその変形が微小管関連タンパク質との相互作用に及ぼす効果に関する研究

Syeda Rubaiya Nasrin

Material Chemistry Laboratory
Graduate School of Chemical Sciences and Engineering
Hokkaido University, Japan

Contents

Chapter 2: Effect of Microtubule Buckling by Applied Compressive Stress on the Interaction between Microtubule and Dynein In vitro

Chapter 4: Effect of Stabilization of Microtubules by Cevipabulin on Microtubule Behavior and their Interaction with Kinesins

Chapter 1

General Introduction

1.1 Purpose

Living organisms are prevalently stimulated by mechanical stress. [1] Many of the biological processes are dependent on the mechanical stimuli, such as embryogenesis, development [2,3] and tissue homeostasis. [4,5] The cytoskeleton responds to such stimulations by altering the flexibility or adhesivity, thereby changing cell shape. [6–9] As the major cytoskeletal component, the microtubules participate in cell shape regulation, cell division, intracellular transportation, etc. [10–12] The structural integrity of the microtubules plays an important role in these cellular processes. The microtubules also help to transmit mechanical stress to activate cytoplasmic proteins and thereby rapid signal transduction occurred *via* the pre-stressed cytoskeleton. [13] However, the mechanism of mechanotransduction by the microtubules is still not clear. Since direct measurement of microtubule stiffness in cells is not accessible so far, the first step towards better understanding the structural role of microtubules is to assess their response to mechanical stimuli *in vitro*. It might involve an understanding of the interaction between microtubules and its associated motor proteins. Moreover, any evidence showing how the mechanical stress applied on microtubules may modulate their biochemical functions has not yet been addressed.

Stress-induced damage [14] and impeded cargo transportation [15] along the microtubules in neurons are cited as two of the major reasons for neurodegenerative diseases. Unfortunately, there is currently no way to slow disease progression and no known cures. The purpose of the present study is to play a role to understand what causes neurodegenerative diseases and develop new approaches for treatment and prevention through exploring the effect of microtubule deformation on the interaction between microtubule and its associated motor proteins.

In this study I aim to understand the mechano-responsiveness of the microtubules under applied compressive stress directly to deformation and systematically investigate the effect on the transport function of the mechanically deformed microtubules *in vitro*. So far, the effects on the motor protein driven transportation along the microtubule have been

addressed by considering lattice defects, loss of parts of protofilaments or polar mismatches in the disrupted protofilaments. [16–18] It should be interesting to reveal why the change in motor protein motility by mechanical stimuli arises from these reasons. For this, the high-speed atomic force microscopy (HS-AFM) [19–21], an observation technique with a high spatio-temporal resolution, was employed to monitor the single kinesin transportation along the microtubules in undeformed and in deformed conditions. A comparison between the kinesin motility behavior along the straight and the bent microtubules could reveal the effect of such mechanical deformation in the microtubules on the movement of kinesins along them.

On the other hand, the contribution of microtubule stabilization in the research of therapeutics for the treatment of neurodegenerative diseases, cancers [22,23] as well as in nanotechnological application [24–29] claims further investigation on the effect of the stabilizing agents on the properties of the microtubule. With this aim, a comparatively less explored drug, cevipabulin's effect on the mechanical property of microtubules was investigated. Therefore, altogether the results of this work may offer new insight for developing new approaches for treatment and prevention of neurodegenerative diseases.

1.2 Cytoskeleton

The eukaryotic cytoskeleton is an intracellular biopolymer scaffold. It is a highly dynamic system but is well-ordered. Therefore, the cytoskeleton maintains a high degree of internal organization in cells. [30,31] It provides the mechanical scaffold and maintains the integrity of cells. In all eukaryotic cells, cytoskeleton consists of an interconnected network of three classes of filaments: namely actin filaments, microtubules and intermediate filaments (Figure 1.1). All these three filaments are made of individual building blocks, either monomers or dimers. These polymers can grow and shrink by introduction or withdrawal of the building blocks.

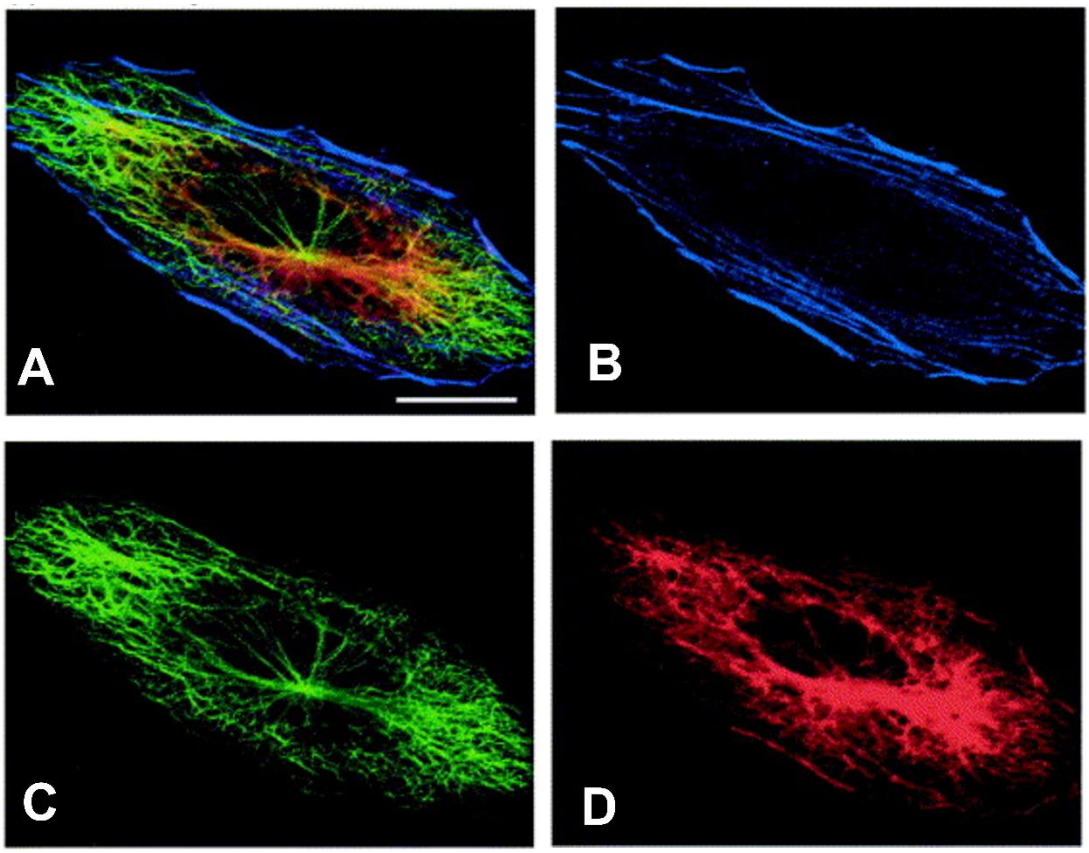

Figure 1.1 *Cytoskeleton.* (A) The cytoskeleton of a Huh7 cultured human hepatocyte cell. (B) Actin filaments, (C) microtubules (D) and intermediate filaments viewed separately. [32] Scale bar: 10 μm.

Actin can be usually found at the cell periphery, where it forms a dynamic meshwork along the plasma membrane. The microtubules typically originate from a specialized microtubule-organizing center and show a radial arrangement. Actin filaments mostly appear in the cross-linked networks, whereas the microtubules are hollow cylindrical tubes that may appear as individuals or in a bundle. [30,33] Due to the large heterogeneity within intermediate filaments, it is hard to generalize their arrangements. [34]

1.2.1 Functions of the cytoskeleton

The main function of cytoskeletal components as their name suggests is to provide shape to the cells. Apart from this, they spatially organize the cellular content and connect the cell to extracellular space. [33] The ability of a eukaryotic cell to resist external stimuli, transport intracellular cargo and change shape depends on them. [10,35] The energy for this cellular remodeling is adapted from the exothermic processes of hydrolysis of adenosine triphosphate (ATP) or guanosine triphosphate (GTP). It is established that the

cytoskeleton is also involved in mechanical signaling. [36] The interconnected network of the cytoskeletal components renders them candidates for mechanotransduction. [37,38] The cytoskeleton both senses and response to external mechanical stresses. For example, the mechanical tension generated in the actin network by the cells and tractional forces exerted on their adhesions to the extracellular matrix. [6] Cytoskeleton by altering matrix flexibility or adhesivity can change cell shape can balance the forces between cells and extracellular matrix, and switch cells between growth and differentiation. [6–9] Many of the biological processes, for example, embryogenesis, development [2,3] and tissue homeostasis [4,5], etc. are dependent on the mechanical stimuli acting on the cells. Microtubule, one of the cytoskeletal components, has been reported to contribute in the mechanotransduction in striated muscle. [39–41]

1.2.2 Microtubule

Microtubules are cytoskeletal biopolymers built from two closely related globular proteins α-tubulin and β-tubulin each of molecular weight 55 kDa with about 50% identical amino acids. [42] These two proteins form the heterodimers, which are then polymerized into the microtubules.

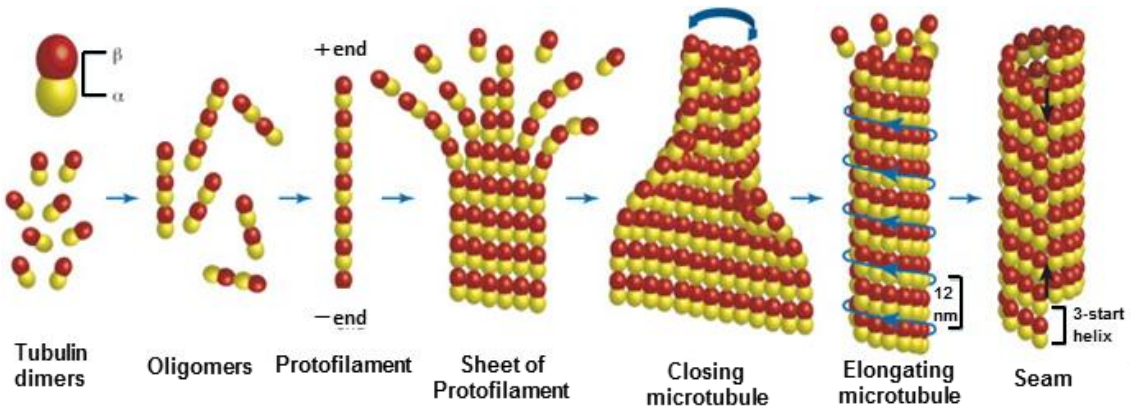

Figure 1.2 *Microtubule polymerization.* Microtubules are polymerized from heterodimers made of α and β globular proteins. Tubulin dimers assemble 'head-to-tail', to form oligomers that elongate into protofilaments. The tubulin lattice has a left-handed helical symmetry. The microtubule closes at the seam (black arrows), causing a discontinuity point in the helical lattice. [43]

The tubulin heterodimers assemble longitudinally into 'protofilaments'. These protofilaments form lateral bonds with each other and arrange into a cylindrical tube of outer diameter about 25 nm and the inner diameter of 17 nm. [44] The inter-protofilament

bonds are anisotropic and three-dimensional. [45,46] Two types of lattice: A-lattice and B-lattice of the microtubules are formed between the unequal α- β subunits or the equal α-α and β-β subunits (Figure 1.2).

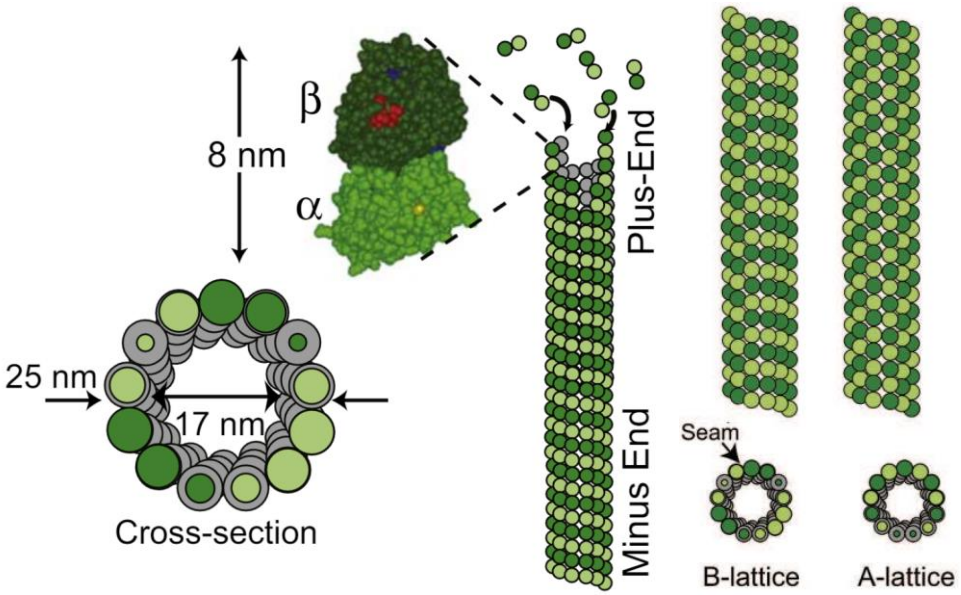

Figure 1.3 Microtubule structure.[47]

B-lattice configurations are more common *in vitro*, while *in vivo* A-lattice configurations are observed in vivo. [48]

1.2.2.1 Microtubule dynamics

Microtubules undergo assembly and disassembly by non-covalent addition and subtraction of tubulin dimers at the ends. Since in the protofilaments tubulin dimers form longitudinal contacts between α- β tubulins, the microtubule results in a polar structure. Microtubule polarity is expressed by plus and minus end which corresponds to faster-growing end with β tubulin exposed and slower-growing end with α tubulin.

The microtubule structure is stabilized by longitudinal and lateral non-covalent interactions between the tubulin subunits that have different properties. [49,50] The lateral inter-protofilament contacts are mostly electrostatic whereas that between the intra-protofilament interactions (-αβ-αβ-) are hydrophobic. [49,51] The longitudinal intra-protofilament tubulin-tubulin bonds (free energy of dissociation ~14.9 kcal/mol) are roughly two-fold stronger than of lateral inter-PF tubulin-tubulin bonds (free energy of dissociation ~6.9 kcal/mol). This differences in tubulin interactions render microtubules

mechanically highly anisotropic. [16] *In vitro*, the rate-limiting step in microtubule polymerization is nucleation. Oligomerization of tubulin dimers is slow since it is energetically unfavorable. After a sufficiently large oligomer is formed, growth becomes favorable and faster. In the absence of co-factors, the critical concentration of tubulin for spontaneous nucleation is 20 - 40 μM. [52]

1.2.2.2. Dynamic instability of microtubules

Microtubules undergo a switching between a slow growth phase and a rapid shrinking phase, termed as the dynamic instability. The transition from a growing to a shrinking end is called a catastrophe and the transition from a shrinking to a growing microtubule ends is termed rescue. [53] The microtubule dynamic instability is utilized for efficient space exploration and allows the cytoskeleton to rearrange in response to various stimuli. [54]

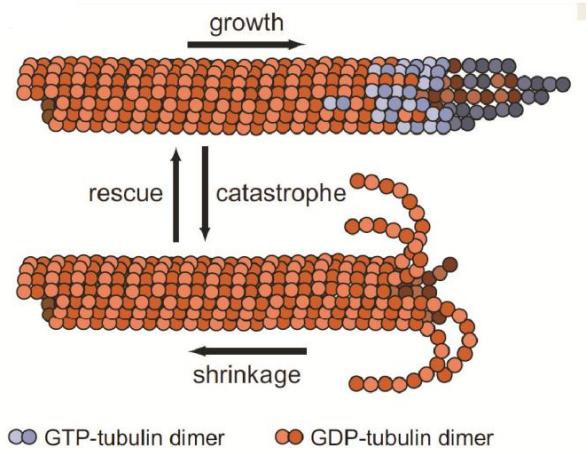

Figure 1.4 *The dynamic instability of the microtubule*. [55] Microtubules continuously undergo polymerization and depolymerization as a result of the dynamic instability in microtubule structure.

The dynamicity of microtubule is largely controlled by the changing environments or during changes in the cell cycle. [56] At higher tubulin concentration catastrophe frequency decreases whereas rescues are observed more often. [57] Therefore, the length of the stabilizing end structure increases at higher growth speeds.

1.2.2.3 Mechanical properties of microtubule

The microtubules are the most rigid cytoskeletal components. A comparison of the three cytoskeletal components is illustrated in Figure 1.5.

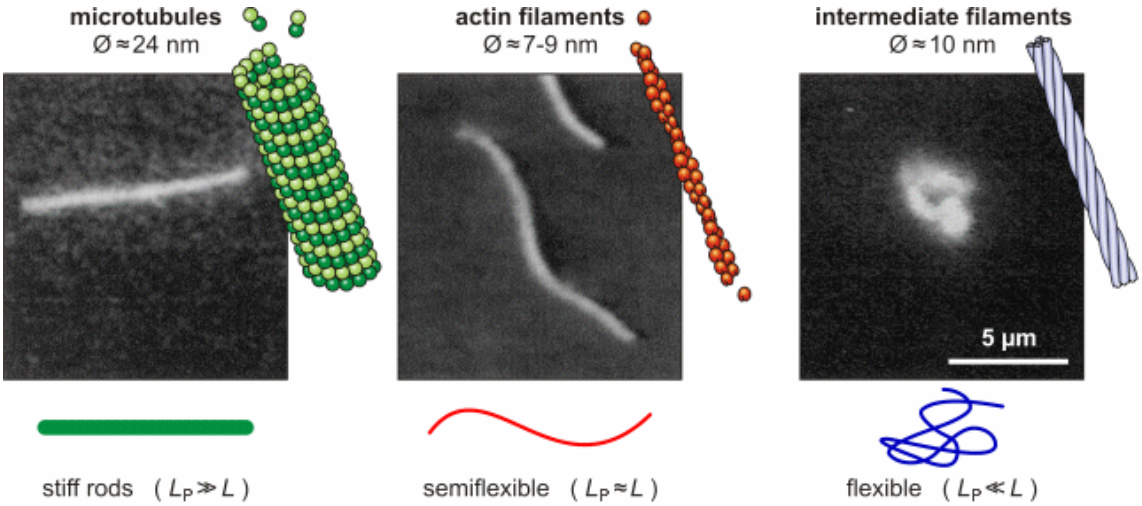

Figure 1.5 *Cytoskeletal filaments*. Fluorescence images of microtubule, actin filaments and intermediate filaments. The figure cited from http://home.uni-leipzig.de/pwm/web/?section=introduction&page=cytoskeleton

To characterize the stiffness of cytoskeletal filaments a useful parameter is the persistence length (L_p). It is the length over which a polymer bends significantly under thermal fluctuations: $\langle t(0).t(s)\rangle_t = e^{-s/Lp}$ … … … (1.1)

where, s is the distance between two points along with the polymer, $t(s)$ is the tangent vector to the curve at position s, and $\langle\rangle_t$ denotes the average over time (t) [58]

The L_p is related to the bending stiffness κ by

$L_P = \kappa/k_BT = EI/k_BT$… … (1.2)

where k_B is the Boltzmann constant, T the absolute temperature, E Young's modulus and I the moment of inertia of the polymer. For microtubules, if the length is L, and the persistence length is L_p, then $L << L_P$.

The persistence length of microtubules estimates a range of values: from 0.03 mm to 46.8 mm. [47] This difference may be a reflection of the influence of the measurement technique as well as the way microtubules are polymerized.

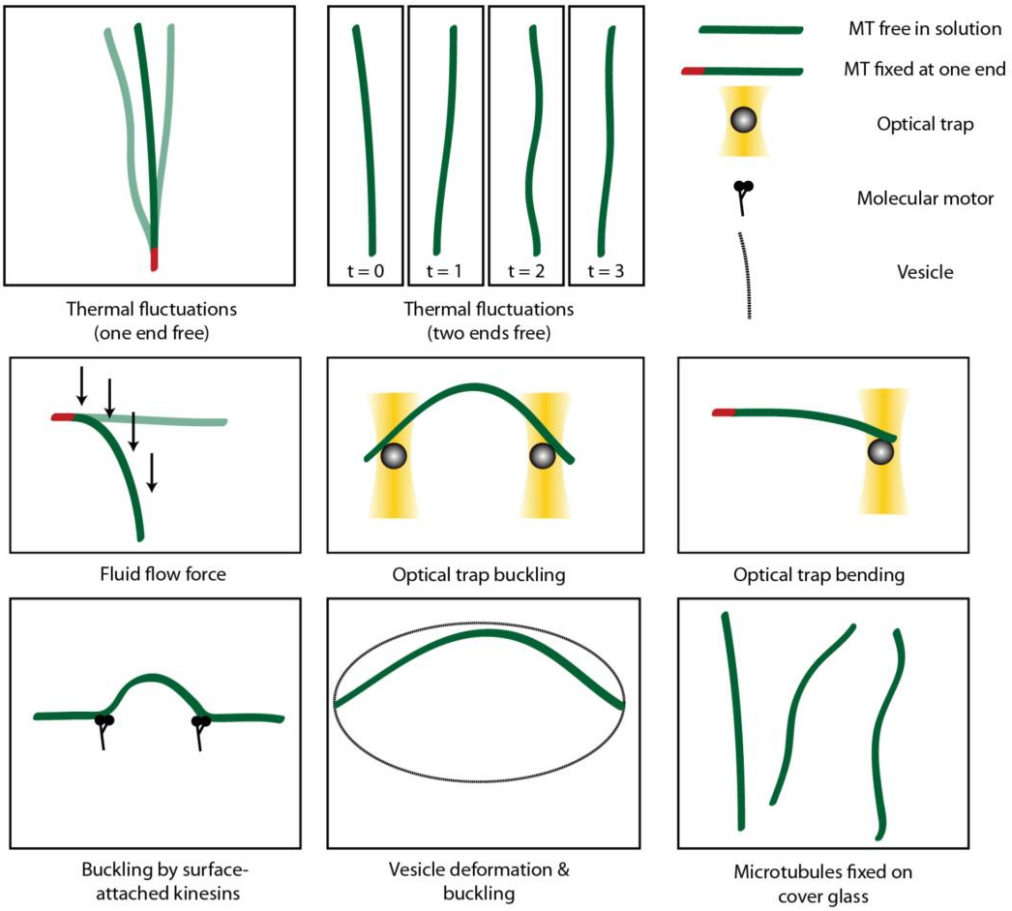

Figure 1.6. *Different techniques for measuring Lp of microtubules.* MT: microtubule.

It is reported that the L_p of microtubules exhibits a length-dependence. [59] The reason for this observation has been linked to the anisotropy of tubulin bonds.

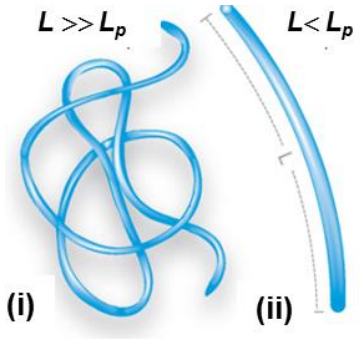

Figure 1.7 *Persistence length***.** Anisotropic mechanical properties of microtubules show the dependence of persistence length of microtubule on contour length.

The anisotropic property of microtubule strongly influences the deformation mechanism of microtubules under compressive stress. [60] Compressed microtubules are equivalent to

a system of rigid elements interconnected through a network of lateral and longitudinal elastic bonds and under compression, the deformation of microtubule occurs through a conserved, complex multistep pathway. [16]

1.3 Biomolecular motor proteins

The microtubule-associated motor-proteins are the biological machines that are responsible for most forms of movement and intracellular transportation. [61] There are two molecular motors that are associated with microtubules in eukaryotic cells: kinesin and dynein. These are two-headed since the microtubules are polar, the translocation of the kinesin and dynein are polarized to a particular direction depending on the nature of the molecular motor. The key functions carried out by the motor proteins are to move vesicles or other cargo along microtubule filaments; they move microtubules relative to each other; and they affect microtubule dynamics important for intracellular transport, cell locomotion or cell division respectively.

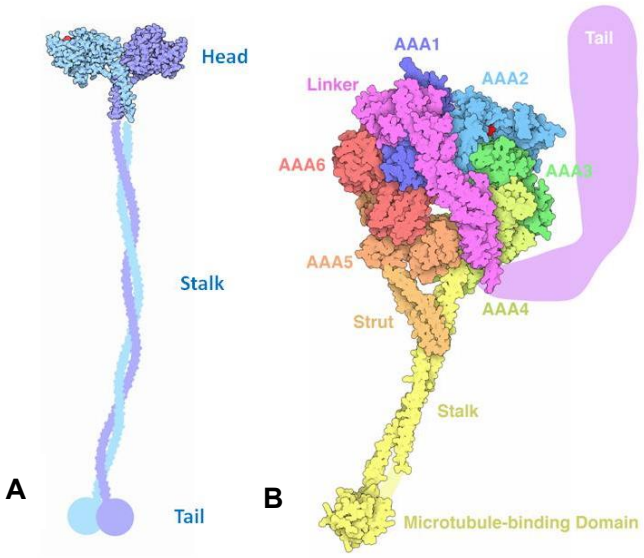

Figure 1.8 *Structures of (A) kinesin and (B) dynein.* Kinesin has a lower molecular weight compared to that of dynein.

1.3.1 Kinesin

The first kinesin protein was isolated from squid giant axons as a plus end-directed motor involved in axonal transport. [62] The conventional kinesin (kinesin-1) is a dimeric motor protein that proceeds unidirectionally toward the plus end of the microtubule in discrete, 8-long steps hydrolyzing one ATP molecule per steps. [63] The kinesin motor can be divided

into three domains as shown in Figure 1.8. The catalytic core (motor head) is the hallmark of the kinesin superfamily. A neck linker is adjacent to the catalytic core. This neck linker is a sequence of 14-18 residues in most *N*-terminal kinesins that undergoes structural rearrangements during stepping. Finally, the two heads in the dimer are connected by the neck-coil domain that connect to the distal coiled-coil and cargo-binding tail.[64] Molecular weight of a conventional kinesin molecule is 120 kDa.

A model for the chemomechanical cycle of kinesin-1 is shown in Figure 1.9. At saturating ATP, the total cycle duration is evenly split between one-head-bound (1HB) and two-heads-bound (2HB) states. [65] The 2HB portion of the cycle begins with the binding of the tethered head (State 1 in Figure 1.9).

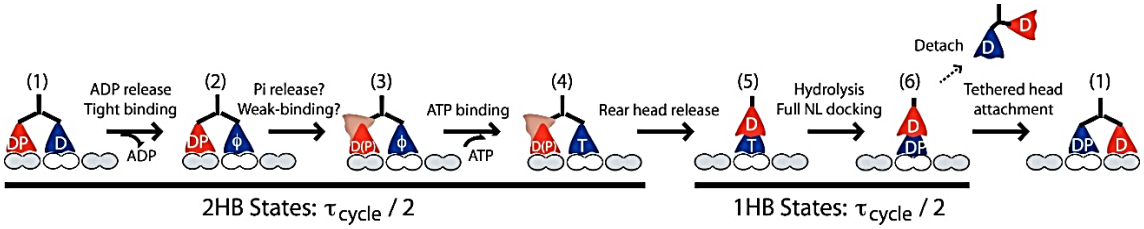

Figure 1.9 *A consensus model of the kinesin-1 chemomechanical cycle.* [66]

Upon tethered head binding, ADP release is rapid, generating a 2HB state (State 2). The rear head then transitions into an ATP waiting state (State 3), a transition that may involve *Pi* release and may involve a different interaction with the microtubule but does not cause a displacement (State 4). There are two 1HB states, one preceding ATP hydrolysis (State 5) and one following it (State 6). Implicit in this model is that ATP binding to the front head triggers a power stroke, meaning a conformational change that accelerates detachment of the trailing head. ATP hydrolysis results in a vulnerable 1HB state (State 6) in which the bound head can detach to terminate the run (<1% for kinesin-1) or the tethered head can attach to complete the step.

1.3.2 Dynein

Dyneins are molecular motors that move toward the minus ends of microtubules, whereas most kinesin motors move in the opposite direction. The molecular weight of dynein is 1.5 MDa. Cytoplasmic dynein is the only dynein isoform that functions in the cytoplasm of eukaryotic cells. It is a large protein complex of at least eight polypeptides and requires

multiple additional proteins and protein complexes for efficient motility. [67] The structure and mechanochemical cycle of dynein differ dramatically from kinesins and myosins.[68]

The mechanochemical cycle of dynein stepping is summarized in Figure 1.10. In the absence of a nucleotide in the AAA1 site (APO state, State 1 in Figure 1.10), dynein tightly attaches to a microtubule [69] and the linker is in a straight (post power stroke) conformation, which runs at the surface of the ring and exits the ring near AAA5. [70] In State 2, ATP binding to AAA1 closes the gap between AAA1 and AAA2, which triggers rigid body motions of the AAA subunits within the ring [70] ATP binding to AAA1 also forces the linker to move from its straight conformation into a bent conformation, referred to as the pre-power stroke or priming stroke. [71] In State 3, the head hydrolyzes ATP before rebinding to a microtubule, which triggers the release of the inorganic phosphate. [72] In the ADP-bound state (State 4), dynein tightly attaches to microtubule and the linker undergoes isomerization from pre to post power stroke conformation, returning to its original straight conformation (Figure 1.10). This transition is believed to generate the force required to drive dynein motility (power stroke). [73] The release of ADP from AAA1 is the rate-limiting step of the mechanochemical cycle, [72] and after ADP release, dynein is primed for ATP binding (State 1) to initiate the next cycle.

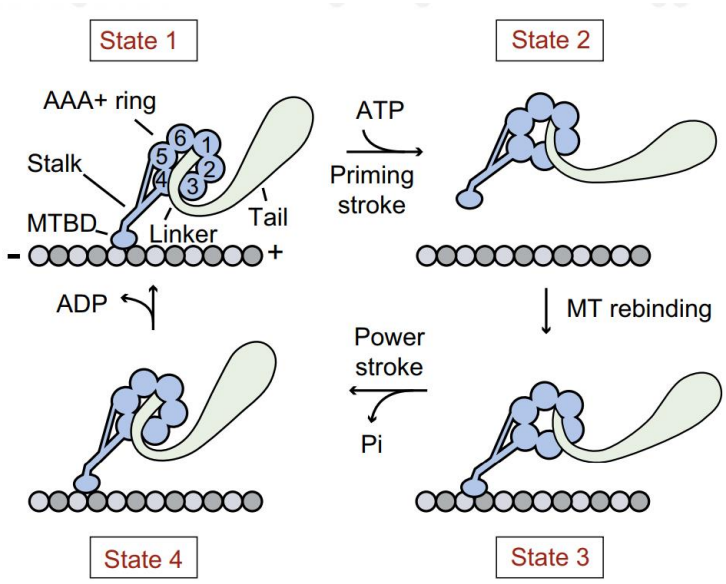

Figure 1.10 *Domain organization and the mechanochemical cycle of DHC.* The AAA+ ring is composed of six AAA domains and binds to microtubules through a coiled-coil stalk with a small MTBD. The linker undergoes ATP-dependent conformational changes.

Synchronization of these conformational changes with the microtubule binding/unbinding cycle generates force and motility. [74]

1.4 Microtubule behavior under compressive stress

In cells, microtubule may generate forces to keep their shape and also may experience forces. These forces exerted by and on the microtubules may induce their mechanical responses. [75] Forces acting on microtubules *in vivo* often make them adopt highly bent or buckled shapes, with short wavelengths on the order of a few microns and curvatures less than1 rad/μm. In addition, bent microtubule shapes appear dynamic and change on the order of seconds. [76,77]

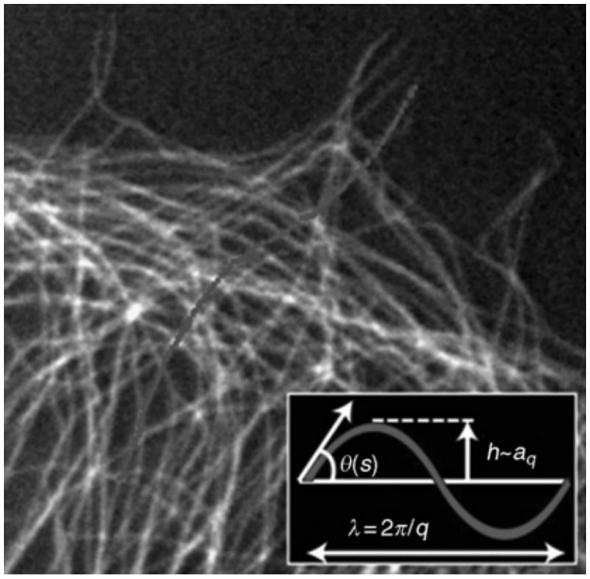

Figure 1.11 *Buckling in microtubules***.** Fluorescently-labeled microtubules showing highly bent shapes, with a single microtubule highlighted. The inset defines the parameters used to extract the amplitude, a_q, and the wavelength, λ of the Fourier modes describing the contour of the microtubule.[78]

Initially, at low compressive stress microtubules behave linearly as an elastic macroscopic tube; at this regime, microtubule lattice resists deformation although a small variation in local curvature may occur. [17] On increasing the compressive force further microtubules enter the nonlinear transition regime in which discrete structural changes occur. The lateral bonds (both α-α, β-β) dissociate first causing the microtubules split open like a zipper. Dissociation of lateral bonds is reversible; ruptured lateral contacts between

adjacent protofilaments can be efficiently annealed on the release of the compressive stress. The further increased mechanical force then results in dissociation of longitudinal interdimer bonds that triggers the microtubule transition to a collapsed state. Contrary to the lateral bonds, the disrupted longitudinal bonds cannot be repaired and inflict permanent damage on the microtubule lattice. Although compressive stress-induced alterations in the microtubule lattice are mostly localized to the lateral and longitudinal interfaces, it can cause small defects at the junction points between α and β-tubulins, on increasing stress the defects may grow in size; this can also be applicable for the preexisting defects at the microtubule lattice. This understanding has important implications in explaining the functional modulation of the deformed microtubule under compressive stress.

1.5 Experimental and theoretical study on mechanical stress induced deformation of microtubule

Computational works on mechanical stress-induced deformation of microtubules have been conducted in recent years. Isolated microtubules are expected to exhibit a classic Euler buckling instability, resulting in the formation of a single long-wavelength arc under exceedingly small forces (~1 pN) due to their large aspect ratio (>100). This is completely unlike the highly buckled appearance of microtubules observed *in vivo.* [79] This behavior of microtubule was predicted by the elastic column model *in vitro* and the increase in critical buckling force *in vivo* is attributed to the surrounding media or cross-linkers, which are often modeled as a continuous and homogenous elastic foundation. [77,80] As a result of the lateral elastic constraint, the multi-wave buckling mode characterized by uniform short buckling waves with smaller deflection is energetically favorable over the single-wave buckling mode predicted by the free-standing elastic column model. With such an elastic foundation model, the critical compressive force and associated wavelength of the buckling modes can be calculated by the conventional method of elastic buckling. [81] However, to explain the localized buckling behavior observed *in vivo,* a micromechanics model has been proposed to investigate the axially compressed buckling of a microtubule surrounded by randomly distributed discrete crosslinkers. [82] Understanding of the buckling behavior of microtubules is important for interpreting the

involvement of microtubules in sensing and responsiveness of mechanical stress and thereby mechanoregulation of cellular events.

1.6 Role of responsiveness of the microtubule in cells

A possible mechanotransduction pathway to influence cell metabolism is the mechanical compression-induced intracellular ion signaling. [83] Since extracellular mechanical forces are reported to directly affect the dynamics of the cytoskeletal components, microtubule's role in cellular mechanotransduction is obvious. [84]

Microtubules are the most rigid cytoskeletal component. Yet they undergo deformation like buckling inside cells indicating that they experience large forces within the cytoplasm. [85] Many biological activities, like, microtubule assembly, [80] organelle transportation along microtubules, [86] feature bending, looping, and buckling of microtubules. Moreover, it has been suggested that microtubule buckling and breaking is the major cause of microtubule reorganization in the central spindle and axonal compression, a common feature of traumatic injuries. [87,88] It has also been reported that mechanotransduction of mechanical stimuli through the microtubule network affects the electrical activity of the heart. [89] Mechanical stimuli also affect microtubule formation and proliferation. Microtubule proliferation has also been shown to increase the intracellular viscosity of myocytes and impede sarcomere shortening, which is required to maintain contractility of the cardiac muscle. [90]

Recent investigations suggest that the dynamics of biomolecular motor driven transportation in neurons is modulated by mechanical stress (Figure 1.12). [91,92]

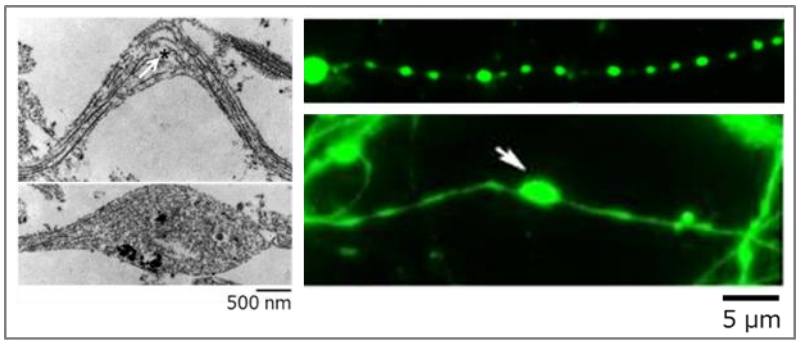

Figure 1.12 *Disruption of microtubule by stress*. In axon, microtubule disruption and impairment of transportation (white arrows) were observed by applying mechanical stress. [93]

In neurons, delivery of proteins, vesicles, etc. to specific destinations through the intracellular transportation is a vital requisite for neuron functionalities such as maintaining synaptic machinery, and regulating the synaptic plasticity, which is the basis for memory, learning, recovery of functions etc. Altered dynamics of neuronal transportation has long been suspected to be linked to several neurodegenerative diseases including Alzheimer's disease, Parkinson's disease, and Amyotrophic Lateral Sclerosis (ALS). [14,15] However, how the transportations by the biomolecular system become modulated in response to the mechanical stress is not understood yet.

1.7 Microtubule-targeting agents

The functions of microtubules are largely determined and controlled by their polymerization dynamics.[94] Such possibility renders microtubules as an attractive target for the treatment of cancers. [95] Stabilization of the polymerized microtubules can lead to mitotic arrest.[96] The principle is to suppress the microtubule dynamics and thus disrupt the metaphase-anaphase transition.[45] This has allowed the microtubule stabilization as an attractive target in the cancer research.[97] Any compound interfering with the microtubule dynamics is a potential anti-mitotic agent. [94] There are two strategies for the tubulin modulators to function: by mimicking the intrinsic assembly-disassembly process or by preventing or facilitating the lateral and/or longitudinal contacts between tubulin dimers of the microtubules.

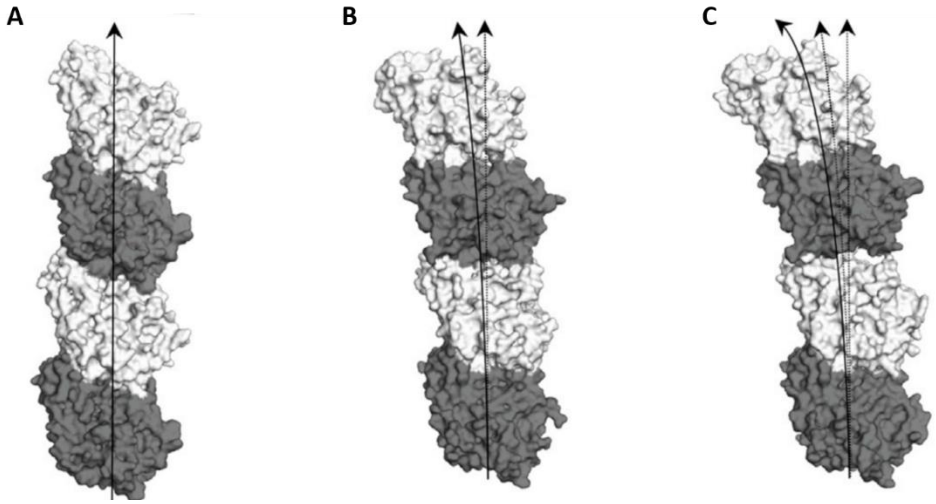

Figure 1.13 *Action of microtubule stabilizing drugs.* Microtubule interaction with (A) paclitaxel (B) triazolopyrimidines (C) vinblastins.

The most common stabilizing agent used until now is the paclitaxel. It binds to the polymerized tubulin and prevents the disassembly of the microtubule polymer.[98] Paclitaxel-site ligands mediate lateral tubulin interactions in microtubules. They bind to a hydrophobic cleft of the β-tubulin subunit and induces structuring of a key loop. [99] The other family of activators belongs to the laulimalide/peloruside class of microtubule-targeting agents. These agents bind to the inter-protofilament interface between two adjacent tubulin dimers and thus act through a tubulin crosslinking mechanism. [100] The vinblastine- and maytansine-site inhibitors, as well as eribulin, in turn, bind to the b-tubulin subunit at the interdimer interface, thus perturbing (vinblastine) or blocking longitudinal tubulin contacts (eribulin) and favoring tubulin-tubulin association but in a non-microtubule-like assembly. [101]

1.8 Instrumentation

Fluorescence microscope and the high-speed atomic force microscopes were used for the observations in the thesis. The working principle and instrumentation of the observation systems are mentioned in brief in the following sections.

1.8.1 Fluorescence Microscopy

Principle:

Fluorescence microscopy is a very powerful analytical tool that combines the magnifying properties of light microscopy with visualization of fluorescence.

Fluorescence describes a phenomenon where a molecular system absorbs, then emits light. In absorption high energy (short wavelength) light excites the system, promoting electrons within the molecule to transition from the ground state, to the excited state (Figure 1.14). Once in this state, and after a lag period of several nano-seconds (the fluorescence lifetime), the electrons will relax back to the ground state, releasing their stored energy in an emitted photon. Due to the higher energy relaxation mechanism this emitted light is of a lower energy (longer wavelength) than the absorbed light. The difference between the excitation and the emission energy (wavelength) is termed the Stokes shift.

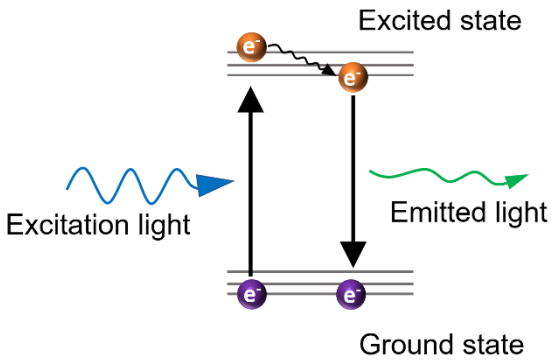

Figure 1.14 Concept of fluorescence.

Fluorescence microscopy combines the magnifying properties of the light microscope with fluorescence technology that allows the excitation and detection of emissions from fluorophores. By tagging a molecule of interest with a fluorophore that molecule can be visualized with remarkable contrast, tracked and analyzed within sample.

Components:

The major components of the fluorescence microscope include fluorophores, a xenon or mercury light source, light filters, the dichroic mirror, and the emission filter (Figure 1.15).

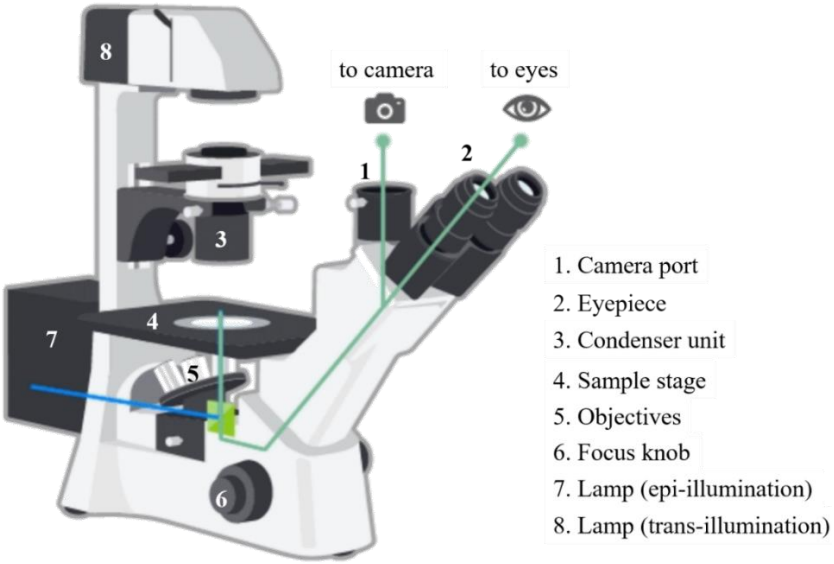

Figure 1.15 *Components of a fluorescence microscope*. The blue line shows the path of the excitation light that reaches the sample through the filter cube and the objective lens, and the emitted radiation (shown in green) simultaneously reaches the detector through

the objective lens and the filter cube. In an epi-fluorescent microscope, both excitation and emission light are transmitted through the same objective.

Application

Fluorescence microscopy is widely used in biology and medicine as well as in other fields. It reveals the position of very tiny amounts of fluorescent substances, which can be introduced into living tissues or cells. Information about the environment of fluorescent probes in the tissues can be obtained by measuring changes in fluorescence spectrum or other characteristics. Fluorescence is also widely used to demonstrate the ramifications of nerve cells, by injection or take-up of fluorochromes into or by living cells.

Limitations

- Fluorophores lose their ability to fluoresce as they are illuminated in a process called photobleaching. Photobleaching occurs as the fluorescent molecules accumulate chemical damage from the electrons excited during fluorescence.
- Cells are susceptible to phototoxicity, particularly with short wavelength light. Furthermore, fluorescent molecules have a tendency to generate reactive chemical species when under illumination which enhances the phototoxic effect.
- Unlike transmitted and reflected light microscopy techniques fluorescence microscopy only allows observation of the specific structures which have been labeled for fluorescence.

1.8.2 High-speed Atomic Force Microscopy

Principle

The HS-AFM is a nano-dynamics visualization technique. This device is realized by developing i.e. speeding up the AFM, suppressing vibration of the scanner, and obtaining high accuracy feedback control.

An AFM uses a cantilever with a very sharp tip to scan over a sample surface. As the tip approaches the surface, the close-range, attractive force between the surface and the tip cause the cantilever to deflect towards the surface. However, as the cantilever is brought even closer to the surface, such that the tip gets in contact with it, increasingly repulsive force takes over and causes the cantilever to deflect away from the surface.

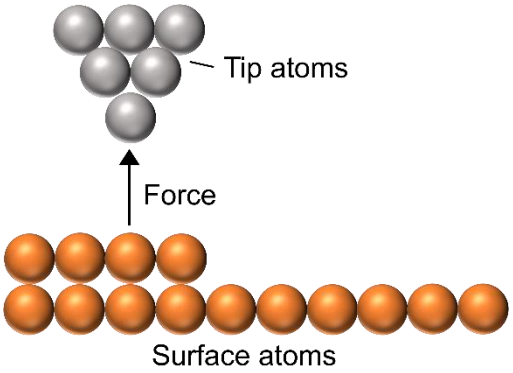

Figure 1.16 *Principle of atomic force microscopy*.

Using this principle AFM can produce accurate topographical image of a surface. HS-AFM is an AFM that can perform real-time imaging without disturbing physiological functions of proteins etc. and weak intermolecular interactions. [102].

Components

The components of HS-AFM are the same as in the AFM. The components include cantilever, scanner, sensor, amplitude measuring instrument, etc. Figure 1.17 illustrates a schematic image of the HS-AFM instruments.

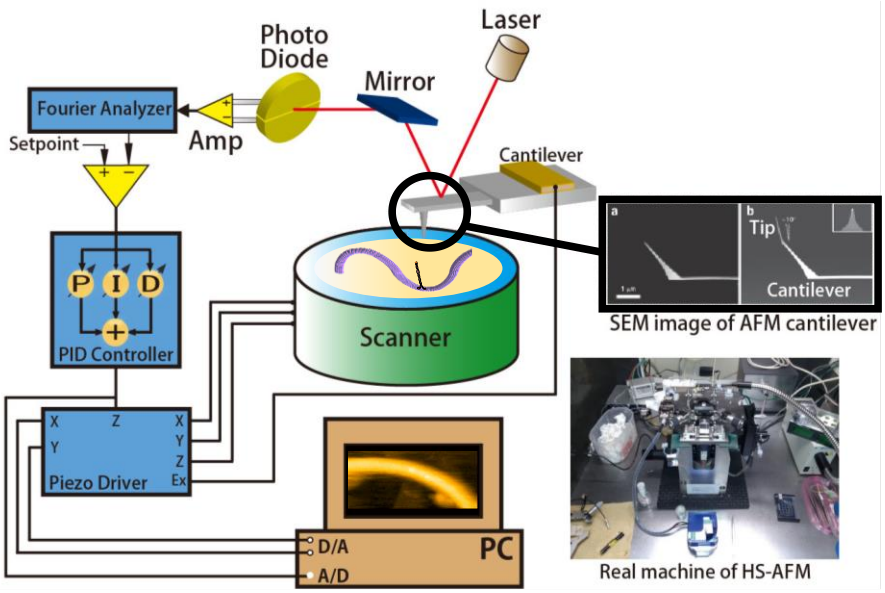

Figure 1.18 *Schematic diagram of HS- AFM.*

Application

HS-AFM being able to perform scanning of regions with about 100 nm size at a frame rate in the order of 100 ms and nanometer lateral resolution, gives the opportunity to observe the diffusion, association/dissociation behavior and conformational changes of label-free membrane proteins in biological membranes. Furthermore, the high-resolution capability and high signal-to-noise ratio of HS-AFM further allows the study of dynamic membrane protein conformational changes, in case that they are slow.

Limitation

- To visualize protein molecules on extremely soft membranes, we need non-contact AFM which has not been established using the AFM principles.
- HS-AFM imaging of the cell interior may not be realized anytime soon. Since floating molecules in cells will be expelled easily by the inserted tip and therefore will not disturb AFM imaging and will also not be imaged.
- The temporal resolution of the HS-AFM could still not reach to the resolution obtained by the fluorescence microscopy.

1.9 Outline of the dissertation

In this dissertation, *in vitro* studies on mechanical deformation of microtubules and the effect of such deformation on the microtubule-motor protein interactions have been studied in detail. Change in the mechanical properties of the microtubules due to change in the stabilizing agent has also been addressed in this dissertation. The results are summarized in 5 chapters including general introduction and concluding remarks.

In **chapter 1**, the purpose of this dissertation and the background of this study have been described.

In **chapter 2**, I studied the dynamics of one of the principal motor proteins, dynein, along microtubules deformed by external mechanical stress, compression. I observed that the deformation of microtubule due to applied compressive stress affected the dynein-driven cargo transportation in an anomalous manner. These results can corroborate that the deformation of the microtubule is regulatory of the response of the dynein movement along the track.

In **chapter 3**, the observation of transportation of single kinesins, another major microtubule-associated motor protein, along microtubule using the HS -AFM is described. A new approach to cause deformation of microtubule on mica supported lipid bilayer have been established. A comparison has been made between the transportation behavior of kinesin along undeformed and deformed microtubules. The kinetic parameters of kinesin binding to the microtubules were determined.

In **chapter 4**, I evaluate the stabilization of microtubules by cevipabulin belonging to one of the least explored class of microtubule-stabilizing agents, [1,2,4]triazolo[1,5-a]pyrimidines. I have investigated the change in mechanical properties of the cevipabulin-stabilized microtubules. Similarities and differences between the microtubules stabilized by cevipabulin and by paclitaxel were explored.

In **chapter 5**, all the important outcomes and prospects of this research work in the future have been summarized.

1.10 References

1. Discher, D. E., Janmey, P. & Wang, Y.-L. Tissue cells feel and respond to the stiffness of their substrate. *Science* **310**, 1139–1143 (2005).
2. Lecuit, T. & Lenne, P. F. Cell surface mechanics and the control of cell shape, tissue patterns and morphogenesis. *Nat. Rev. Mol. Cell Biol.* **8**, 633–644 (2007).
3. Le, H. Q. *et al.* Mechanical regulation of transcription controls Polycomb-mediated gene silencing during lineage commitment. *Nat. Cell Biol.* **18**, 864–875 (2016).
4. Matthews, B. D. Cellular adaptation to mechanical stress: role of integrins, Rho, cytoskeletal tension and mechanosensitive ion channels. *J. Cell Sci.* **119**, 508–518 (2006).
5. Barnes, J. M., Przybyla, L. & Weaver, V. M. Tissue mechanics regulate brain development, homeostasis and disease. *J. Cell Sci.* **130**, 71–82 (2017).
6. Ingber, D. Integrins as mechanochemical transducers. *Curr. Opin. Cell Biol.* **3**, 841–848 (1991).
7. Ingber, D. E. & Folkman, J. Mechanochemical switching between growth and differentiation during fibroblast growth factor-stimulated angiogenesis in vitro: role of extracellular matrix. *J. Cell Biol.* **109**, 317 LP – 330 (1989).
8. Singhvi, R. *et al.* Engineering cell shape and function. *Science (80-.).* **264**, 696 LP – 698 (1994).
9. Maniotis, A. & Schliwa, M. Microsurgical removal of centrosomes blocks cell reproduction and centriole generation in BSC-1 cells. *Cell* **67**, 495–504 (1991).
10. B. Alberts, A. Johnson, J. Lewis, M. Raff, K. Roberts, P. W. *Molecular biology of cell*. (Garland Science, New York, 2008).
11. Howard, J. *Mechanics of Motor Proteins and the Cytoskeleton*. (Sinauer Associates, Inc., Sunderland, Massachusetts, 2001).
12. Ross, J. L., Ali, M. Y. & Warshaw, D. M. Cargo transport: molecular motors navigate a complex cytoskeleton. *Curr. Opin. Cell Biol.* **20**, 41–47 (2008).
13. Na, S. *et al.* Rapid signal transduction in living cells is a unique feature of mechanotransduction. *Proc. Natl. Acad. Sci. U. S. A.* **105**, 6626–6631 (2008).
14. Chevalier-Larsen, E. & Holzbaur, E. L. F. Axonal transport and neurodegenerative disease. *Biochim. Biophys. Acta - Mol. Basis Dis.* **1762**, 1094–1108 (2006).

15. Mcguire, D. Traumatic brain injury and neurodegenerative disease. in *The Wiley Handbook on the Aging Mind and Brain* 591–618 (2017). doi:10.1002/9781118772034.ch26

16. Kononova, O. *et al.* Tubulin bond energies and microtubule biomechanics determined from nanoindentation in silico. *J. Am. Chem. Soc.* **136**, 17036–17045 (2014).

17. Schaap, I. A. T., Carrasco, C., de Pablo, P. J., MacKintosh, F. C. & Schmidt, C. F. Elastic response, buckling, and instability of microtubules under radial indentation. *Biophys. J.* **91**, 1521–1531 (2006).

18. Deriu, M. A. *et al.* Anisotropic elastic network modeling of entire microtubules. *Biophys. J.* **99**, 2190–2199 (2010).

19. Ando, T., Uchihashi, T. & Fukuma, T. High-speed atomic force microscopy for nano-visualization of dynamic biomolecular processes. *Prog. Surf. Sci.* **83**, 337–437 (2008).

20. Ando, T., Uchihashi, T. & Kodera, N. High-Speed AFM and applications to biomolecular systems. *Annu. Rev. Biophys.* **42**, 393–414 (2013).

21. Ando, T. High-speed atomic force microscopy and its future prospects. *Biophys. Rev.* **10**, 285–292 (2018).

22. Brunden, K. R., Trojanowski, J. Q., Smith, A. B., Lee, V. M. Y. & Ballatore, C. Microtubule-stabilizing agents as potential therapeutics for neurodegenerative disease. *Bioorganic Med. Chem.* **22**, 5040–5049 (2015).

23. Ballatore, C., Brunden, K. R., Trojanowski, J. Q., Lee, V. M. Y. & Smith, A. B. Non-Naturally Occurring Small Molecule Microtubule-Stabilizing Agents: A Potential Tactic for CNS-Directed Therapies. *ACS Chem. Neurosci.* **8**, 5–7 (2017).

24. U, H. H. & Vogel, V. Molecular shuttles based on motor proteins : active transport in synthetic environments. 67–85 (2001).

25. Hess, H., Bachand, G. D. & Vogel, V. Powering Nanodevices with Biomolecular Motors. *Chem. - A Eur. J.* **10**, 2110–2116 (2004).

26. Van Den Heuvel, M. G. L. & Dekker, C. Motor proteins at work for nanotechnology. *Science* **317**, 333–336 (2007).

27. Keya, J. J. *et al.* DNA-assisted swarm control in a biomolecular motor system. *Nat. Commun.* **9**, 4–11 (2018).

28. Inoue, D. *et al.* Sensing surface mechanical deformation using active probes driven by motor proteins. *Nat. Commun.* **7**, 12557 (2016).

29. Matsuda, K. *et al.* Artificial Smooth Muscle Model Composed of Hierarchically Ordered Microtubule Asters Mediated by DNA Origami Nanostructures. *Nano Lett.* **19**, 3933–3938 (2019).

30. Huber, F. *et al.* Emergent complexity of the cytoskeleton: from single filaments to tissue. *Adv. Phys.* **62**, 1–112 (2013).

31. Gupta, M. *et al.* Adaptive rheology and ordering of cell cytoskeleton govern matrix rigidity sensing. *Nat. Commun.* **6**, 7525 (2015).

32. Omary, M. B., Ku, N.-O., Tao, G.-Z., Toivola, D. M. & Liao, J. 'Heads and tails' of intermediate filament phosphorylation: multiple sites and functional insights. *Trends Biochem. Sci.* **31**, 383–394 (2006).

33. Fletcher, D. A. & Mullins, R. D. Cell mechanics and the cytoskeleton. *Nature* **463**, 485–492 (2010).

34. Wagner, O. I. *et al.* Softness, strength and self-repair in intermediate filament networks. *Exp. Cell Res.* **313**, 2228–2235 (2007).

35. Liu, A. P. & Fletcher, D. A. Biology under construction: in vitro reconstitution of cellular function. *Nat. Rev. Mol. Cell Biol.* **10**, 644–650 (2009).

36. Janmey, P. A. The cytoskeleton and cell signaling: component localization and mechanical coupling. *Physiol. Rev.* **78**, 763–781 (1998).

37. Forgacs, G. On the possible role of cytoskeletal filamentous networks in intracellular signaling: an approach based on percolation. *J. Cell Sci.* **108**, 2131 LP – 2143 (1995).

38. Maniotis, A. J., Chen, C. S. & Ingber, D. E. Demonstration of mechanical connections between integrins, cytoskeletal filaments, and nucleoplasm that stabilize nuclear structure. *Proc. Natl. Acad. Sci.* **94**, 849 LP – 854 (1997).

39. Prosser, B. L., Ward, C. W. & Lederer, W. J. X-ROS signaling: rapid mechano-chemo transduction in heart. *Science* **333**, 1440–1445 (2011).

40. Khairallah, R. J. *et al.* Microtubules Underlie Dysfunction in Duchenne Muscular Dystrophy. *Sci. Signal.* **5**, ra56 (1-10) (2012).

41. Belanto, J. J. *et al.* Microtubule binding distinguishes dystrophin from utrophin. *Proc. Natl. Acad. Sci.* **111**, 5723–5728 (2014).

42. Burns, R. G. Alpha-, beta-, and gamma-tubulins: sequence comparisons and structural constraints. *Cell Motil. Cytoskeleton* **20**, 181–189 (1991).

43. Pampaloni, F. & Florin, E.-L. Microtubule architecture: inspiration for novel carbon nanotube-based biomimetic materials. *Trends Biotechnol.* **26**, 302–310 (2008).

44. Schuyler, S. C. & Pellman, D. Microtubule 'plus-end-tracking proteins': The end is just the beginning. *Cell* **105**, 421–424 (2001).

45. Nogales, E. Structural Insights Into Microtubule Function. *Annu. Rev. Biophys. Biomol. Struct.* 277–302 (2001).

46. Sui, H. & Downing, K. H. Structural basis of interprotofilament interaction and lateral deformation of microtubules. *Structure* **18**, 1022–1031 (2010).

47. Hawkins, T., Mirigian, M., Selcuk Yasar, M. & Ross, J. L. Mechanics of microtubules. *J. Biomech.* **43**, 23–30 (2010).

48. Scheele, R. B., Bergen, L. G. & Borisy, G. G. Control of the structural fidelity of microtubules by initiation sites. *J. Mol. Biol.* **154**, 485–500 (1982).

49. Wang, H.-W. & Nogales, E. Nucleotide-dependent bending flexibility of tubulin regulates microtubule assembly. *Nature* **435**, 911–915 (2005).

50. VanBuren, V., Odde, D. J. & Cassimeris, L. Estimates of lateral and longitudinal bond energies within the microtubule lattice. *Proc. Natl. Acad. Sci.* **99**, 6035–6040 (2002).

51. Nogales, E., Whittaker, M., Milligan, R. A. & Downing, K. H. High-Resolution Model of the Microtubule. *Cell* **96**, 79–88 (1999).

52. Kollman, J. M., Merdes, A., Mourey, L. & Agard, D. A. Microtubule nucleation by gamma-tubulin complexes. *Nat. Rev. Mol. Cell Biol.* **12**, 709–721 (2011).

53. Mitchison, T., Kirschner, M. & Mitchison T, K. M. Dynamic instability of microtubule growth. *Nature* **312**, 237–42 (1984).

54. Desai, A. & Mitchison, T. J. Microtubule polymerization dynamics. *Annu. Rev. Cell Dev. Biol.* **13**, 83–117 (1997).

55. Dráber, P., Sulimenko, V. & Dráberová, E. Cytoskeleton in Mast Cell Signaling . *Frontiers in Immunology* **3**, 130 (2012).

56. Saxton, W. M. *et al.* Tubulin dynamics in cultured mammalian cells. *J. Cell Biol.*

99, 2175–2186 (1984).

57. Walker, R. A. *et al.* Dynamic instability of individual microtubules analyzed by video light microscopy: rate constants and transition frequencies. *J. Cell Biol.* **107**, 1437–1448 (1988).

58. Martin, D. S. Measuring microtubule persistence length using a microtubule gliding assay. *Methods Cell Biol.* **115**, 13–25 (2013).

59. Pampaloni, F. *et al.* Thermal fluctuations of grafted microtubules provide evidence of a length-dependent persistence length. *Proc. Natl. Acad. Sci.* **103**, 10248–10253 (2006).

60. Waterman-Storer, C. M. & Salmon, E. D. Actomyosin-based retrograde flow of microtubules in the lamella of migrating epithelial cells influences microtubule dynamic instability and turnover and is associated with microtubule breakage and treadmilling. *J. Cell Biol.* **139**, 417–434 (1997).

61. Woehlke, G. & Schliwa, M. Walking on Two Heads: the Many Talents of Kinesin. *Nat. Rev. Mol. Cell Biol.* **1**, 50–58 (2000).

62. Vale, R. D., Reese, T. S. & Sheetz, M. P. Identification of a novel force-generating protein, kinesin, involved in microtubule-based motility. *Cell* **42**, 39–50 (1985).

63. Schnitzer, M. J. & Block, S. M. Kinesin hydrolyses one ATP per 8-nm step. *Nature* **388**, 386–390 (1997).

64. Vale, R. D. The molecular motor toolbox for intracellular transport. *Cell* **112**, 467–480 (2003).

65. Weisshaar, B., Doll, T. & Matus, A. Reorganisation of the microtubular cytoskeleton by embryonic microtubule-associated protein 2 (MAP2c). *Development* **1161**, 1151–1161 (1992).

66. Hancock, W. O. The kinesin-1 chemomechanical cycle: stepping toward a consensus. *Biophys. J.* **110**, 1216–1225 (2016).

67. Cianfrocco, M. A., DeSantis, M. E., Leschziner, A. E. & Reck-Peterson, S. L. Mechanism and Regulation of Cytoplasmic Dynein. *Annu. Rev. Cell Dev. Biol.* **31**, (2015).

68. Imai, H. *et al.* Direct observation shows superposition and large scale flexibility within cytoplasmic dynein motors moving along microtubules. *Nat. Commun.* **6**, 8179 (2015).

69. Burgess, S. A., Walker, M. L., Sakakibara, H., Knight, P. J. & Oiwa, K. Dynein structure and power stroke. *Nature* **421**, 715–718 (2003).

70. Bhabha, G., Johnson, G. T., Schroeder, C. M. & Vale, R. D. How dynein moves along microtubules. *Trends Biochem. Sci.* **41**, 94–105 (2016).

71. Kon, T. *et al.* The 2.8 A crystal structure of the dynein motor domain. *Nature* **484**, 345–350 (2012).

72. Mogami, T., Kon, T., Ito, K. & Sutoh, K. Kinetic characterization of tail swing steps in the ATPase cycle of Dictyostelium cytoplasmic dynein. *J. Biol. Chem.* **282**, 21639–21644 (2007).

73. DeWitt, M. A., Chang, A. Y., Combs, P. A. & Yildiz, A. Cytoplasmic dynein moves through uncoordinated stepping of the AAA+ ring domains. *Sciene* **335**, 221–225 (2012).

74. Yildiz, A. *5 - Single-molecule dynein motor mechanics invitro*. *Dyneins* (Elsevier Inc.). doi:10.1016/B978-0-12-809470-9.00005-9

75. Schaller, V., Weber, C., Semmrich, C., Frey, E. & Bausch, A. R. Polar patterns of driven filaments. *Nature* **467**, 73 (2010).

76. Odde, D. J., Ma, L., Briggs, A. H., DeMarco, A. & Kirschner, M. W. Microtubule bending and breaking in living fibroblast cells. *J. Cell Sci.* **112**, 3283–3288 (1999).

77. Brangwynne, C. P. *et al.* Microtubules can bear enhanced compressive loads in living cells because of lateral reinforcement. *J. Cell Biol.* **173**, 733–741 (2006).

78. Gardel, M. L., Kasza, K. E., Brangwynne, C. P., Liu, J. & Weitz, D. A. B. T.-M. in C. B. Mechanical response of cytoskeletal networks. in *Biophysical Tools for Biologists, Volume Two: In Vivo Techniques* **89**, 487–519 (Academic Press, 2008).

79. Laan, L., Husson, J., Munteanu, E. L., Kerssemakers, J. W. J. & Dogterom, M. Force-generation and dynamic instability of microtubule bundles. *Proc. Natl. Acad. Sci.* **105**, 8920–8925 (2008).

80. Gupton, S. L., Salmon, W. C. & Waterman-Storer, C. M. Converging populations of F-actin promote breakage of associated microtubules to spatially regulate microtubule turnover in migrating cells. *Curr. Biol.* **12**, 1891–1899 (2002).

81. Ansel C. Ugural; Saul K, F. *Advanced mechanics of materials and applied elasticity*. (Pearson Education, Inc., 2012).

82. Jin, M. Z. & Ru, C. Q. Localized buckling of a microtubule surrounded by

randomly distributed cross linkers. *Phys. Rev. E* **88**, 12701 (2013).

83. Rodriguez, O. C. *et al.* Conserved microtubule-actin interactions in cell movement and morphogenesis. *Nat. Cell Biol.* **5**, 599–609 (2003).

84. *Cellular Mechanotransduction diverse perspectives from molecules to tissues*. (Cambridge University Press, 1977).

85. Brangwynne, C. P., MacKintosh, F. C. & Weitz, D. A. Force fluctuations and polymerization dynamics of intracellular microtubules. *Proc. Natl. Acad. Sci.* **104**, 16128–16133 (2007).

86. Jolly, A. L. *et al.* Kinesin-1 heavy chain mediates microtubule sliding to drive changes in cell shape. *Proc. Natl. Acad. Sci.* **107**, 12151 LP – 12156 (2010).

87. Stichel, C. C. & Müller, H. W. Experimental strategies to promote axonal regeneration after traumatic central nervous system injury. *Prog. Neurobiol.* **56**, 119–148 (1998).

88. Hubbard, R. D., Quinn, K. P., Martinez, J. J. & Winkelstein, B. A. The role of graded nerve root compression on axonal damage, neuropeptide changes, and pain-related behaviors. *Stapp Car Crash J.* **52**, 33–58 (2008).

89. White, E. Mechanical modulation of cardiac microtubules. *Pflugers Arch.* **462**, 177–184 (2011).

90. Cooper, G. 4th. Cytoskeletal networks and the regulation of cardiac contractility: microtubules, hypertrophy, and cardiac dysfunction. *Am. J. Physiol. Heart Circ. Physiol.* **291**, H1003-14 (2006).

91. Ahmed, W. W. *et al.* Mechanical tension modulates local and global vesicle dynamics in neurons. *Cell. Mol. Bioeng.* **5**, 155–164 (2012).

92. Ahmed, W. W. & Saif, T. A. Active transport of vesicles in neurons is modulated by mechanical tension. *Sci. Rep.* **4**, 4481 (2014).

93. Tang-Schomer, M. D., Johnson, V. E., Baas, P. W., Stewart, W. & Smith, D. H. Partial interruption of axonal transport due to microtubule breakage accounts for the formation of periodic varicosities after traumatic axonal injury. *Exp. Neurol.* **233**, 364–372 (2012).

94. Jordan, M. A., Thrower, D. & Wilson, L. Effects of vinblastine, podophyllotoxin and nocodazole on mitotic spindles. *J. Cell Sci.* **102**, 401–416 (1992).

95. Mukhtar, E., Adhami, V. M. & Mukhtar, H. Targeting Microtubules by Natural

Agents for Cancer Therapy. *Mol. Cancer Ther.* **13**, 275 LP – 284 (2014).

96. Jordan, M. A., Toso, R. J., Thrower, D. & Wilson, L. Mechanism of mitotic block and inhibition of cell proliferation by taxol at low concentrations. *Proc. Natl. Acad. Sci.* **90**, 9552–9556 (2006).

97. Kavallaris, M. Microtubules and resistance to tubulin-binding agents. *Nat. Rev. Cancer* **10**, 194–204 (2010).

98. Zhou, J. & Giannakakou, P. Targeting microtubules for cancer chemotherapy. *Curr. Med. Chem. Anticancer. Agents* **5**, 65–71 (2005).

99. Prota, A. E. *et al.* Molecular mechanism of action of microtubule-stabilizing anticancer agents. *Science* **339**, 587–590 (2013).

100. Prota, A. E. *et al.* Structural basis of microtubule stabilization by laulimalide and peloruside A. *Angew. Chem. Int. Ed. Engl.* **53**, 1621–1625 (2014).

101. Doodhi, H. *et al.* Termination of Protofilament Elongation by Eribulin Induces Lattice Defects that Promote Microtubule Catastrophes. *Curr. Biol.* **26**, 1713–1721 (2016).

102. Shibafuji, Y. *et al.* Single-molecule imaging analysis of elementary reaction steps of trichoderma reesei cellobiohydrolase i (Cel7A) hydrolyzing crystalline cellulose Iα and IIII. *J. Biol. Chem.* **289**, 14056–14065 (2014).

Chapter 2

Effect of Microtubule Buckling by Applied Compressive Stress on the Interaction between Microtubule and Dynein *In vitro*

Abstract

Mechanical stress is a frequent stimulation influencing several biological processes, like cell shape regulation, the formation of tissue pattern, development, etc. In recent years, microtubule, an important cytoskeletal component, has been drawing attention for their mechanosensing properties, although any direct evidence is lacking yet. In this chapter, I studied the dynamics of one of the principal motor proteins, dynein, along the microtubules deformed by external mechanical stress, compression. I observed that the deformation of the microtubules due to applied compressive stress affected the dynein-driven cargo transportation in an anomalous manner. These results can corroborate that the deformation of the microtubules is regulatory of the response of the dynein movement along the track. Moreover, this finding will provide further opportunity to explore the role of microtubules in mechanoregulation of cellular processes.

2.1 Introduction

Mechanical stress is a prevalent stimulus in living organisms. Many of the biological processes like embryogenesis, development [1,2] and tissue homeostasis [3,4], etc. are dependent on the mechanical stimuli. For sensing the mechanical stimuli, mechanosensitive channels of small and large conductance (MscS, MscL), transient receptor potential cation channel (TRPV4), [5,6] p130Cas, talin, [7,8] are known to be responsible. A recent report suggests that cytoskeletal filamentous proteins, e.g. actin and microtubule, also contribute to the pathway of mechanosensing to activate cellular signaling. [9] For example, actin filament shows variable affinity to an actin severing protein, cofilin, under tensile mechanical stress, which in turn affects severing of the actin filament. [10] Increased interaction between the actin filament and its associated motor protein, myosin II, under mechanical stimulation also supports the mechano-sensitivity of actin. [11] Compared to actin, mechanosensing behavior of the microtubules has remained elusive. It has been reported that the dynamic instability of the microtubules is altered in response to mechanical stimulation. [12] Mechanical stress tunes the rigidity of microtubules, [13] and influences their growth, rescue, and self-healing. [14] Furthermore, mechanical stress helps microtubules modulate the intercellular transport processes of vesicles in neurons. [15]

In this chapter, I address how mechanical deformation, i.e. the change in the shape of the microtubules due to external compressive stress affects the transportation of quantum dots (Qdots) as cargo by dynein, *in vitro*. To deform the microtubule mechanically in a controlled manner I used external mechanical stimuli (compressive stress) on a two-dimensional elastic medium. [16,17] It was found that buckling of the microtubules altered the dynamics of dynein-driven transportation along the microtubules. This work confirms

the connection between microtubule deformation and modulation of the motor protein-based transportation which might help understand the mechanical stress-induced modulation of intracellular transportation. [18] The responsiveness of the microtubules to compressive stress suggests that the microtubule in cells can serve as a mechanosensor.

2.2 Results and Discussion

2.2.1. Experimental set up to deform microtubules on a two-dimensional elastic medium by applied compressive stress

I used a custom-made experimental setup '*micro-stretcher*' in order to cause deformation of the microtubules (Figure 2.1). [16,17] A soft elastomeric substrate, polydimethylsiloxane (PDMS) was first fixed on the *micro-stretcher* and stretched 100%. On the pre-stretched fixed PDMS, the kinesins were adsorbed. No adenosine triphosphate (ATP) was present at that instant. The fluorescent dye-labeled microtubules were introduced into the flow cell by shear flow. The adsorbed kinesins were aligned on the same plane and fixed perpendicularly to the microtubules deposited at the PDMS. [17] Thus, the kinesins on the PDMS worked as anchors to the microtubules on the substrate (Figure 2.1).

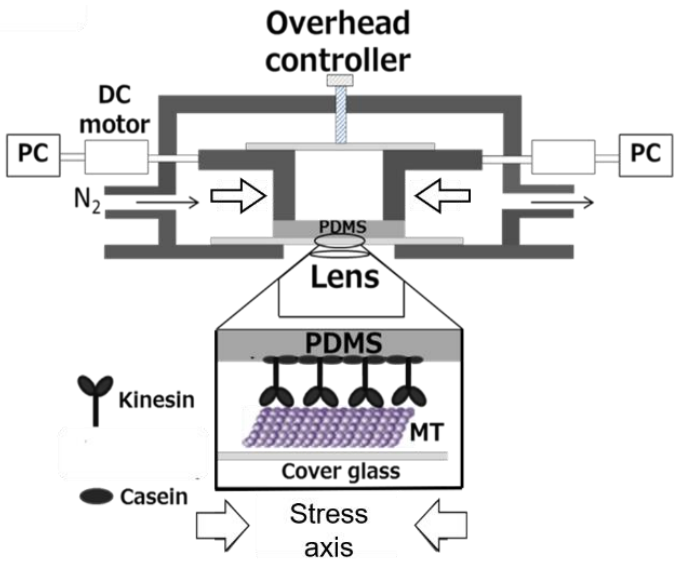

Figure 2.1. *Experimental setup*. Schematic illustration showing experimental setup for applying external stress (e.g. compressive stress) to the microtubules attached on a kinesin coated PDMS substrate using the *micro-stretcher*. [17] Computer-controlled motors were used for applying a uniaxial extension to the fixed PDMS. The experiment was performed

inside the chamber with an inert atmosphere using humid nitrogen gas. [MT: microtubule, PDMS: polydimethylsiloxane, DC: direct current, PC: personal computer.]

Compressing the pre-stretched PDMS had caused applied compressive strain on the microtubules immobilized on the substrate. Continuous increase in the compressive stresses applied on the PDMS using computer-controlled program consequently had resulted in buckling of the microtubules.

2.2.2 Buckling of microtubules caused by applied compressive stress

The microtubules attached on the PDMS through interaction with kinesins were subject to compressive stress when the tension acting on the pre-stretched PDMS was released. To calculate the % applied strain on the microtubule, the length of the PDMS before (L_o) and after (L_f) applying the compressive stress were measured and the % applied strain was calculated from the formula,

$$\%applied\ strain = \frac{L_o - L_f}{L_o} \quad \ldots\ldots\ldots\ldots\ldots\ldots (2.1)$$

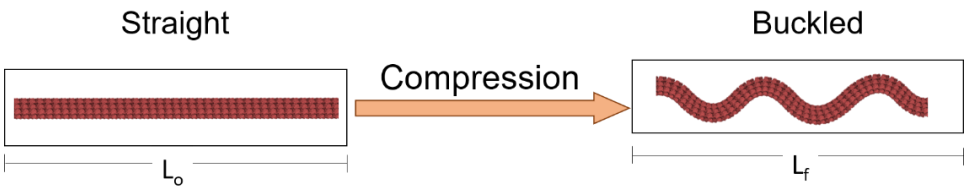

$$\%applied\ strain\ = \frac{L_o - L_f}{L_o} \times 100\%$$

Figure 2.2. *Microtubule buckling scheme*. Schematic images showing the calculation of % applied strain from the initial length L_0 and final length L_f of PDMS substrate before and after applying compression, respectively.

2.2.2.1 Demonstration of the buckling of microtubules by applied compressive strain on PDMS

Compression of the PDMS substrate developed compressive stress at the microtubules deposited to the substrate, which resulted in mechanical deformation of the microtubules manifested by buckling, as shown by the following fluorescence microscopy images in Figure 2.3.

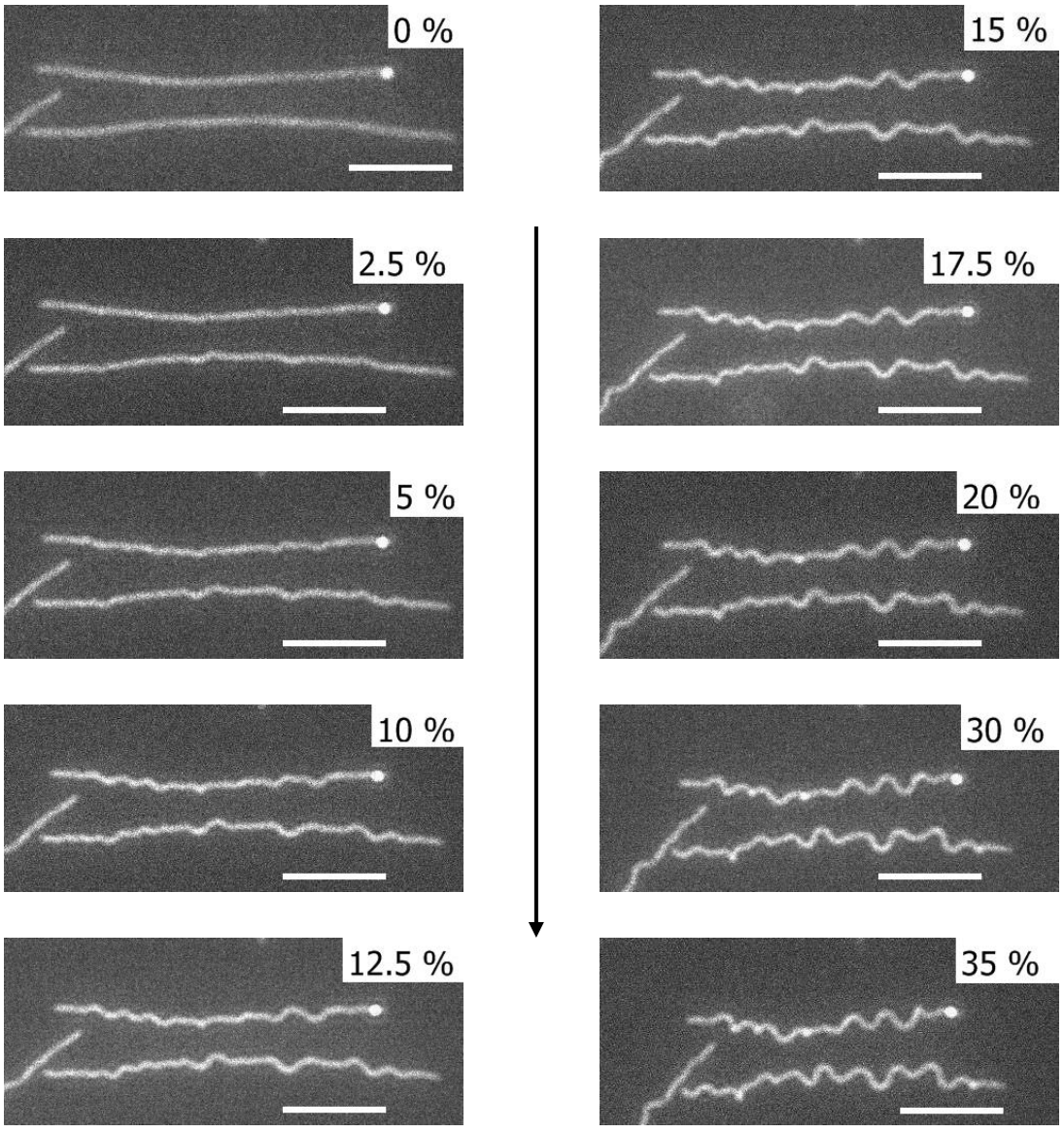

Figure 2.3. *Microtubule buckling*. Fluorescence microscopy images showing the buckling of microtubule caused by increasing compressive strain on the microtubules fixed on the PDMS using 100 nM kinesin. Strain rate: 0.42 %/s. Scale bar: 10 μm.

2.2.2.2. Characterization of the buckled microtubules at a fixed kinesin concentration

From the fluorescence microscopy images of the microtubules under different compressive strains, multi-wave mode of buckling of microtubule could be observed. Such observation is reminiscent of the demonstration of laterally constrained microtubules with both ends clamped as described previously. [19] The length scale of the buckling of the microtubules in this study corresponds well with that observed inside cells. [20–22] By controlling the compression of the stretched PDMS the applied compressive strain on the microtubules could be tuned. This became evident from the change in buckling wavelength and amplitude of the microtubules buckled at different applied compressive strain (Figure 2.4).

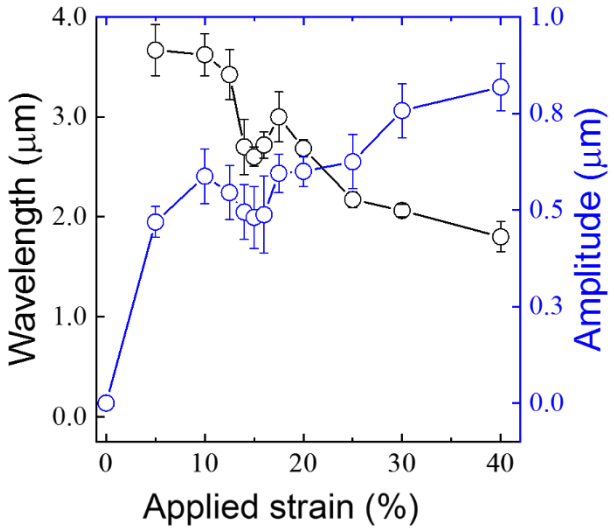

Figure 2.4. *Change in buckling wavelength and amplitude.* Change in buckling wavelength (black open circles) and amplitude (blue open circles) of the microtubules as a response to increasing of applied compressive strain. The concentration of kinesin for

attaching microtubule to PDMS was 100 nM. Error bar: standard deviation. The number of data considered for each point was 20.

The trend in change in wavelength and amplitude of the microtubules in response to the applied compressive stress was typical for a bending beam, except around 15.0 % compressive strain a drop was observed. This may be attributed to the mode of mechanical deformation of the microtubules which will be discussed in detail later.

2.2.3 Effect of the microtubule deformation by applied compressive strain on the dynein-driven Qdot transportation

2.2.3.1 Experimental assay for observation of dynein-driven cargo transportation along microtubules

In order to investigate the effect of compressive stress on microtubule-associated cargo transportation, I studied the Qdot transportation by multiple dynein motors along the microtubules deformed by applied compressive strain. For this, the dynein motors were conjugated to the benzylguanine modified Qdots [23] (mixed at a molar concentration ratio 10 nM dynein to 1 nM Qdot) and were allowed to transport along the buckled microtubules in presence of 1 mM ATP at different compressive strains (Figure 2.5). The number of dynein molecules bound to a Qdot was estimated as ≤ 3. [24] Since the presence of ATP causes gliding of the microtubules over anchor kinesins, [25] it was important to immobilize the microtubules on PDMS. To accomplish this, after the microtubule buckling had taken place by applying different compressive strain on the PDMS, the buckled microtubules were crosslinked with the anchor kinesins using 0.1 % (v/v) glutaraldehyde. The glutaraldehyde fixation reaction was quenched by 0.1 M glycine. After that, pre-incubated solution of Qdot-dynein in presence of 1 mM ATP was

introduced to the observation system for investigating the Qdot transportation by dyneins along these immobilized- deformed microtubules.

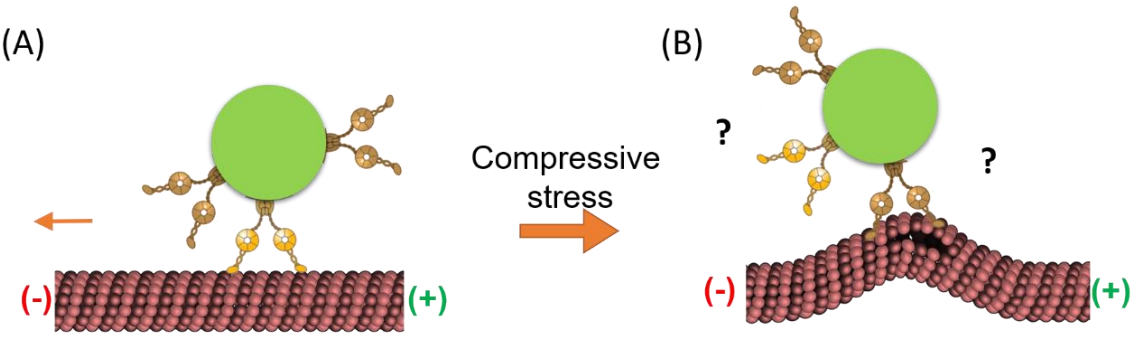

Figure 2.5. *Schematic illustration of dynein-driven Qdot transportation assay*. Schematic illustration of dynein-driven Qdot transportation assay along (A) undeformed microtubule and (B) buckled microtubule. To observe Qdot transportation along buckled microtubules, the microtubules were buckled prior to addition of dynein-Qdot conjugates.

2.2.3.2 Effect of microtubule-kinesin crosslinking on the Qdot transportation

The immobilization of the microtubules using glutaraldehyde treatment was validated to impose no harmful effect on cargo transportation along the microtubule. For this, Qdot transportation by the kinesin molecules was studied as control along the microtubules that were immobilized on PDMS in the absence and in presence of varying glutaraldehyde concentrations. Velocities of the Qdots transported by kinesins were checked and it was found that the velocity did not differ significantly in the presence of 0.1 % glutaraldehyde compared to that in the absence of glutaraldehyde. [26–28] Therefore, the glutaraldehyde treatment of microtubule using 0.1 % glutaraldehyde (v/v) is expected to not influence the Qdot transportation by motor proteins.

Figure 2.6. shows the observation of the effect of glutaraldehyde-fixation of microtubules on the velocity of kinesin-driven Qdot transportation.

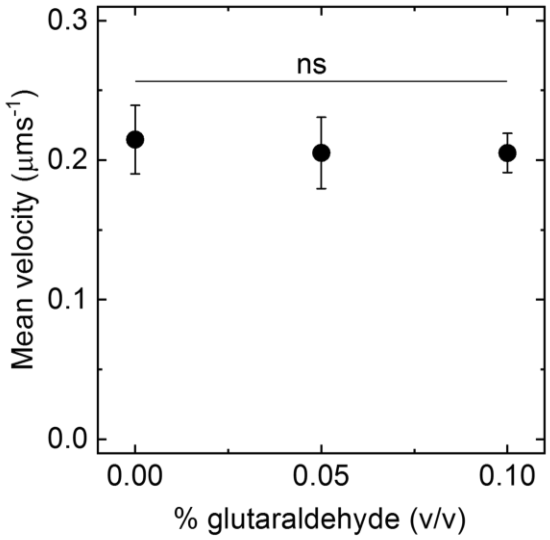

Figure 2.6. *Kinesin driven transportation along immobilized microtubules.* The velocity of kinesin-driven Qdots along microtubules fixed on the substrate using protein A - anti-tubulin antibody in the presence of varying concentrations of glutaraldehyde. No statistically significant difference was observed in the velocity of kinesin using a varying concentration of glutaraldehyde (One-way ANOVA followed by Tukey's multiple comparison test, P>0.001). ns = non-significant. Error bars: standard error of the mean.

2.2.4 Dynein-driven Qdot transportation along microtubules deformed by external compressive strains

A single cargo conjugated to several dynein motors is known to move unidirectionally generating a robust motion towards the minus end of the microtubule in an *in vitro* condition. [29,30] The time-lapse fluorescence microscopy images showing the transportation of Qdot by dyneins along an undeformed microtubule in presence of ATP are shown in Figure 2.7.

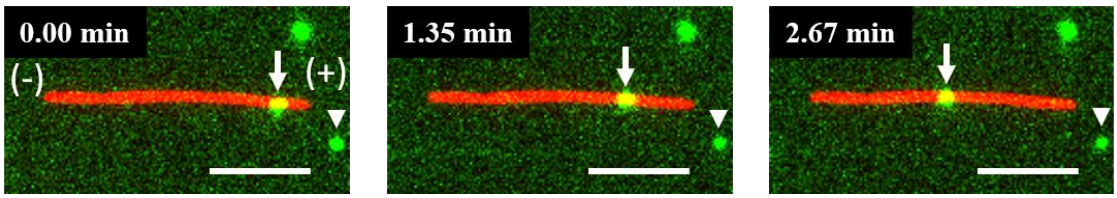

Figure 2.7. *Time lapse fluorescence microscopy images of straight microtubules.* Time lapse fluorescence microscopy images of dynein-driven Qdot transportation along undeformed microtubule immobilized on PDMS in presence of 1 mM ATP. The plus and minus ends of the microtubule are denoted in the first image of the series. The positions of the Qdot that is being transported by dynein along the microtubule in each image are indicated by the vertical white arrows. An immobile Qdot lying on the flow cell is indicated by the white arrowheads as reference. Scale bar: 10 μm.

To observe the effect of microtubule buckling on the dynein-driven Qdot transportation, microtubules were buckled at varying compressive stresses up to 40.0 %. A series of time-lapse images from the observation of Qdot transportation by dyneins along buckled microtubule compressed under 20.0 % compressive stress is shown in Figure 2.8.

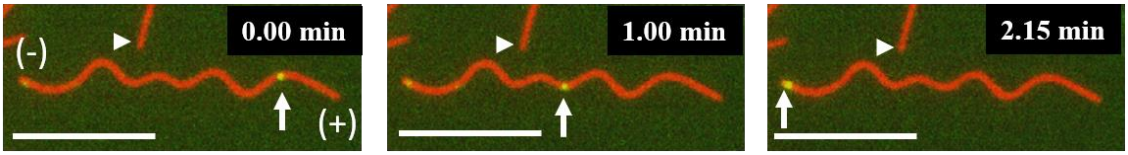

Figure 2.8. *Time lapse fluorescence microscopy images of buckled microtubules.* Time-lapse fluorescence microscopy images of dynein-driven Qdot transportation along buckled microtubule immobilized on PDMS under 20.0 % compressive stress in presence on 1 mM ATP. The plus and minus ends of the microtubule are denoted in the first image of the series. The positions of the Qdot that is being transported by dynein along the microtubule in each image are indicated by the vertical white arrows. End of another immobile microtubule is indicated by the white arrow heads for reference. Scale bar: 10 μm.

2.2.4.1 Effect of applied compressive strain on the microtubules on the time-displacement relation of dynein-driven Qdot transportation

The movement of the Qdots by dyneins was recorded with a frame interval of 3 seconds. It was observed that the Qdots conjugated to multiple dyneins moved unidirectionally towards to minus end of microtubules, which supports the cooperative nature of dyneins

reported previously. [31] Therefore, the effect of microtubule buckling on dynein-based Qdot transportation could be perceived from the time-displacement profile of the dynein-driven cargo transportation along undeformed microtubules and microtubules buckled under various compressive strains (Figure 2.9).

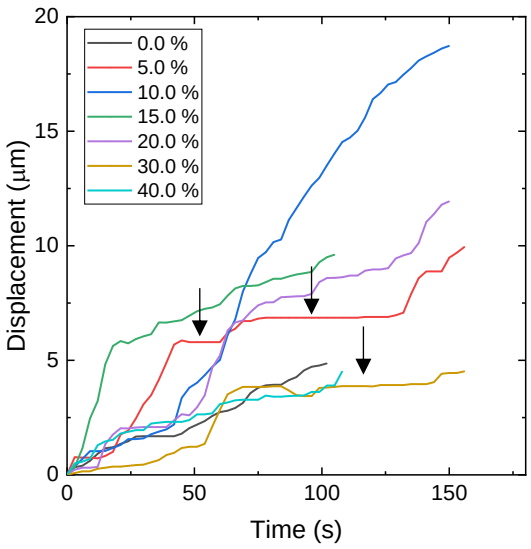

Figure 2.9. *Time-displacement profile.* Time-displacement profiles of dyneins conjugated to Qdot while transporting along the microtubules buckled by different compressive stresses (0.0 % to 40.0 %). Representative events for each case are shown in the plot. Presence of pauses while transporting along the buckled microtubules are indicated using the vertical black arrows.

The time-displacement profiles of the representative events of dynein-driven Qdot transportation along microtubules under different compressive strains are shown in Figure 2.9. This figure shows that the transportation behavior of the dynein-driven Qdots along the deformed microtubules is accompanied by several pausing phases. However, from the profiles in Figure 2.9. any correlation between the pausing events with the increase in the compressive strain could not be established.

2.2.4.2 Effect of applied compressive strain on the microtubules on the velocity of dynein-driven Qdot transportation

The velocities of the Qdots driven by the dyneins along microtubules exposed to different compressive stresses were determined. The distributions of the dynein-driven Qdot velocities along microtubules are given in Figure 2.10. The velocities of the dynein conjugated Qdots are calculated from analysis of the displacement by the dynein-driven Qdot per unit time. It was found that the histogram of velocities of Qdots conjugated to multiple dynein motors along undeformed straight microtubules followed the Gaussian distribution with a mean velocity of about 50 nms^{-1} (n= 92) (Figure 2.10). The cooperative behavior of multiple dyneins has been reported earlier which is consistent with the shape of the distribution.[29] The mean velocity obtained here is consistent with the velocity of multiple dynein motors reported previously. [32] On the other hand, for Qdot transportation along the microtubules buckled at each applied compressive strain, one additional peak at higher velocity was located in the distribution of velocities. It was found that the distribution of the population of dynein-driven Qdot velocities along buckled microtubules was the best fit with a sum of two Gaussian peaks. Such results indicated the presence of at least two groups of population functioning along the buckled microtubules (Figure 2.10). The fact that no such additional peak in the histogram of moving Qdot velocities along straight microtubule was present indicates that the introduction of buckling may have accelerated a fraction of population of dynein which ultimately had exhibited higher velocity while transporting Qdots.

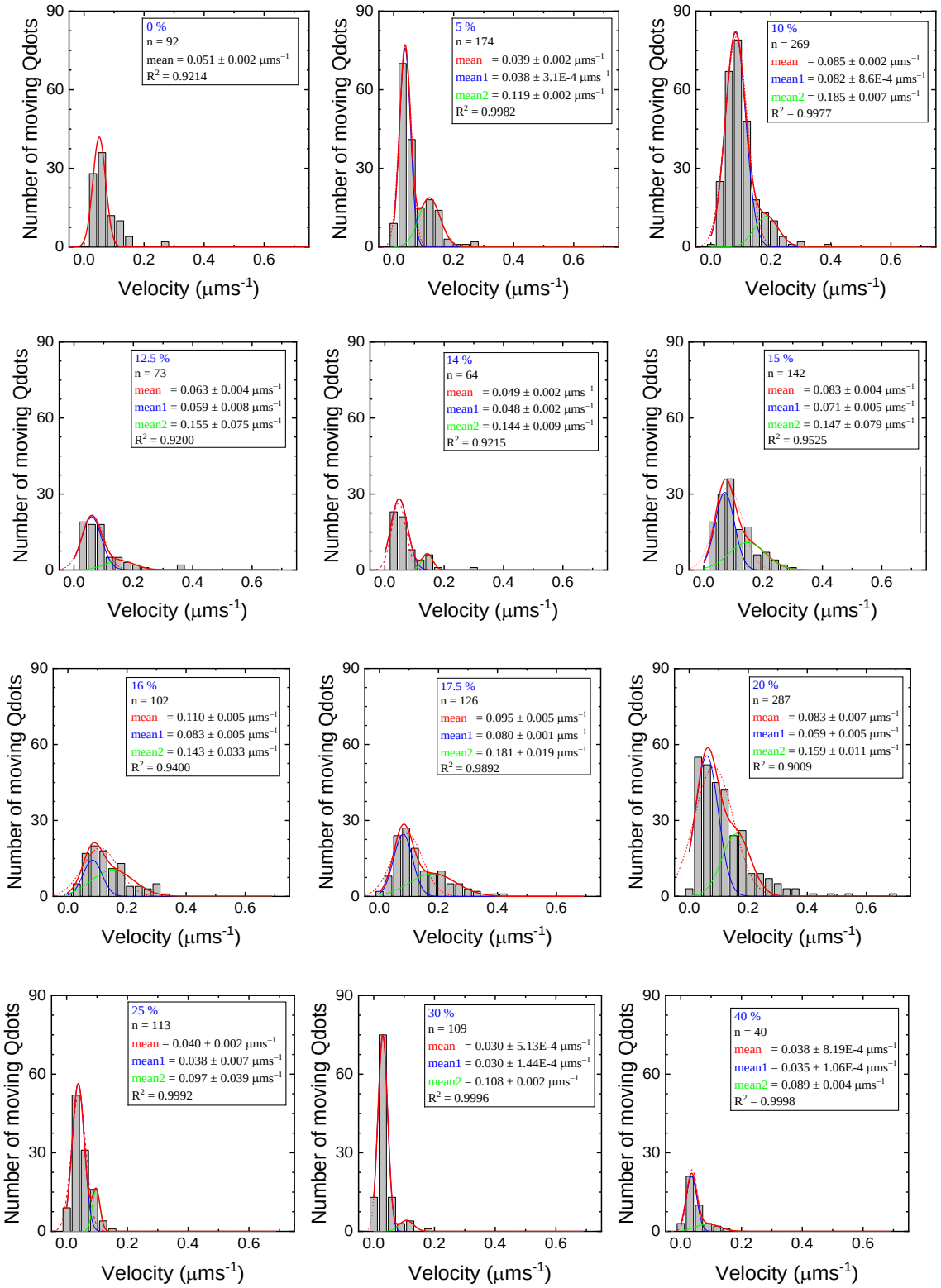

Figure 2.10. *Distribution of velocity of dynein-driven Qdots along microtubule under different compressive strains.* For the cases of deformed microtubule, the distributions showed two peaks. Therefore, the distributions were fitted to 2 peak Gaussian distribution

using equation, $y = \frac{A}{w\sqrt{\frac{\pi}{2}}} e^{-2\frac{(x-x_C)^2}{w^2}}$, where A, w and x_c are area, width and centers of the peaks, respectively. The solid red line is the convoluted peak from the first and second peaks represented using the blue and green solid lines respectively. Bin size = 0.03 μms^{-1}. Number of events analyzed, mean velocities and goodness of fit are mentioned in respective plots. "mean1" and "mean2" correspond to the 2-peaks that were obtained from the multiple peak curve fitting whereas, "mean" in each plot represents the mean velocity obtained from single peak Gaussian fittings of the distributions (red dashed lines).

Two velocity populations were resulted from the histograms in Figure 2.10 (at compressive strains 5.0% to 40.0%). By considering the area of the peaks, fractions of the total population that showed low and high velocities were determined (Figure 2.11).

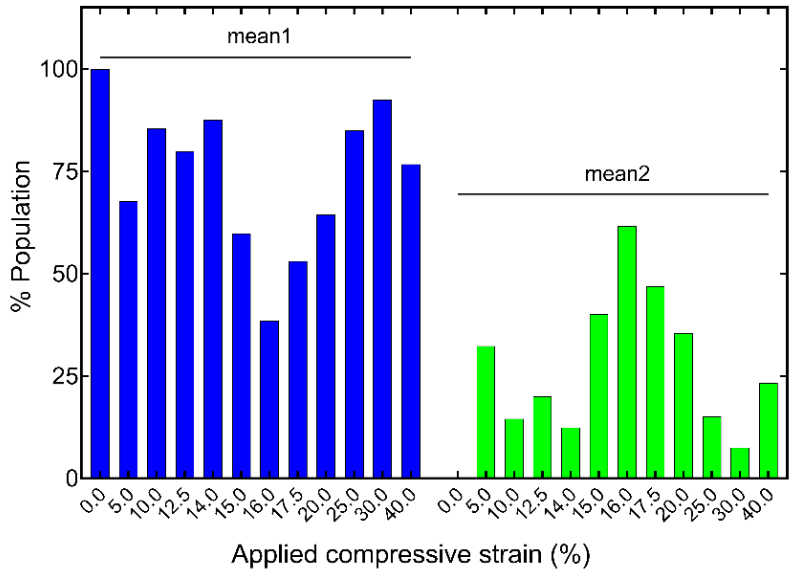

Figure 2.11. The fraction of the total population of Qdot transported by dyneins found in each velocity category, calculated from the area under each Gaussian fit from Figure 2.10. To calculate % population the sum of area in each fit was considered as 100%, and the fraction was expressed as percent of total population. For the Qdot transportation along undeformed microtubules, the mean velocity of transported Qdots from single peak fitting was in the lower velocity criteria and was considered to be exhibited by 100% of population.

The population of Qdots driven by dyneins with high velocity along only the deformed microtubules may indicate that the buckling of the microtubules by compressive strain have accelerated dynein motility. The velocities obtained by fitting the distributions of the velocity of the dynein-driven Qdot transportation along microtubules in Figure 2.11 were plotted against the compressive stress applied (Figure 2.12). The tendency of velocities exhibited by both population appeared to follow the same nature.

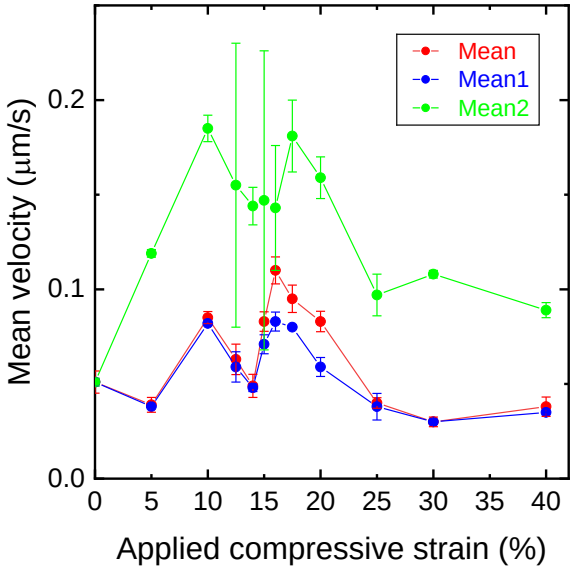

Figure 2.12. *Mean velocities of the dynein driven Qdots.* Mean velocities of the dynein droven Qdots obtained from the fiiting of velocity distributions to single peak Gaussian equation (Mean, red), and 2-peak Gaussian from Figure 2.10 (Mean1, blue and Mean2, green).

Dynein while walking processively along the microtubules exhibit pauses. [32] In the present observation, while transporting Qdot by multiple dynein motors, pausing events were found. Therefore, velocities with and without considering pauses were determined and plotted against the applied compressive strain.

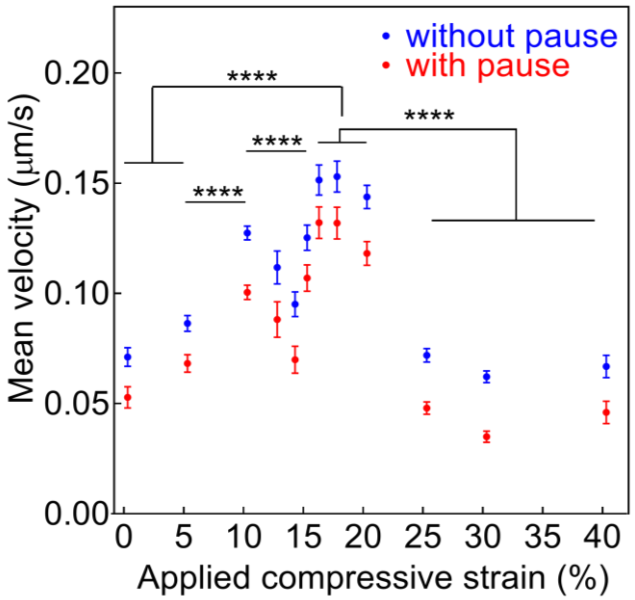

Figure 2.13 *Effect on dynein-driven Qdot velocities.* Change in velocities of dynein-driven Qdot transportation with the change of applied compressive stress on microtubule. The trend in change in velocity remains identical when determined excluding the pausing events. The velocities are found to be significantly different at ***P < 0.001 and ****P < 0.0001 when compared with each other using Kruskal-Wallis test followed by Dunn's multiple comparison test. Error bar: standard error. Numbers of events analyzed are 92, 174, 269, 73, 64, 142, 102, 126, 287, 113, 109 and 40 for % applied compressive strains 0.0, 5.0, 10.0, 12.5, 14.0, 15.0, 16.0, 17.5, 20.0, 25.0, 30.0 and 40.0, respectively.

The velocities of dynein-driven Qdots were favored up to 20.0 % strain with a drop around 15.0 % strain. At and above 25.0 % compressive strain, the dynein-driven transportation slowed down. The gradual increase in the velocity of dynein-driven transportation up to 10.0 % compressive strain (P < 0.0001, Kruskal-Wallis test followed by Dunn's multiple comparison test) might be accounted for by its stochastic [33,34] and diffusing stepping tendency to a larger searching region [35,36] along the deformed microtubule. However, the reason for the drop of the mean velocity observed at ~15.0 % strain remains inexplicable.

The buckling of the microtubules resulted from the compressive strains acting on them can be characterized in terms of the segment curvature of the buckled microtubules.

Curvature of an arc is a measure of how much the curve deviates from a straight line. Therefore, it can be a suitable approach to quantify the extent of buckling in microtubules due to applied compressive strain. In this analysis, I considered the buckled microtubules (compressed at applied strain 5.0 % to 40.0 %) as a series of several curved segments. Curvature of each segment was determined using a custom MATLAB program. The maximum and minimum values of the curvatures obtained were 0.004 and 1.360 μm^{-1}. Next, the curvatures were categorized in to bins of size 0.10 μm^{-1}. Mean velocities of the dynein-driven Qdots along segments having curvatures in each bin were determined and then plotted against their curvature (Figure 2.14).

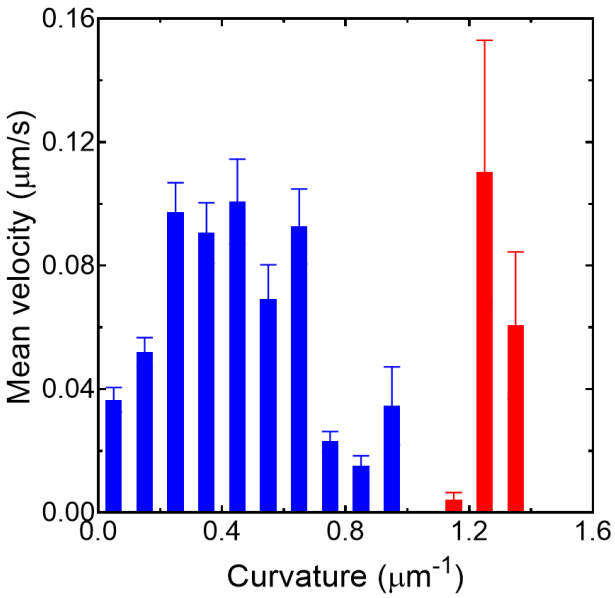

Figure 2.14 *Velocities vs. curvature of buckled microtubule.* Velocities of Qdots transported by dyneins along microtubules buckled at different compressive strains ranging from 5.0 % to 40.0 %. The microtubule segment curvatures were divided into bins of 0.10 μm^{-1}. Means of velocities of dynein-driven Qdots along microtubule segments with curvatures in each bin were determined. For this plot, 1084 instantaneous velocities of Qdot transportation events obtained from displacement between every two consecutive frames along 24 buckled microtubules at different compressive strains were analyzed. The red bars are to denote the most buckled microtubule segments included in

the analysis. Error bar: standard deviation.

Mean velocity versus curvature showed a similar response as in Figure 2.14, i.e. rise in velocities with a drop in between. Therefore, it is evident that an anomalous drop in the velocity of dynein-driven Qdots in response to the buckling deformation of the microtubule is characteristic of its nature. The clear separation between the two peaks of the velocities indicates that it is the difference in the mode of the microtubule deformation that regulates the response of dynein-driven transportation.

2.2.4.3 Effect of applied compressive strain on microtubules on the pause frequency of dynein-driven Qdot transportation

Single dynein molecules are reported to exhibit pauses while processively moving along a microtubule in presence of ATP. [32] As a team, such pause is exhibited also exhibited by multiple dynein motors attached to cargo. [24] In the present study, I have observed pausing events during the dynein-driven Qdot transportation along the undeformed and buckled microtubules (Figure 2.15).

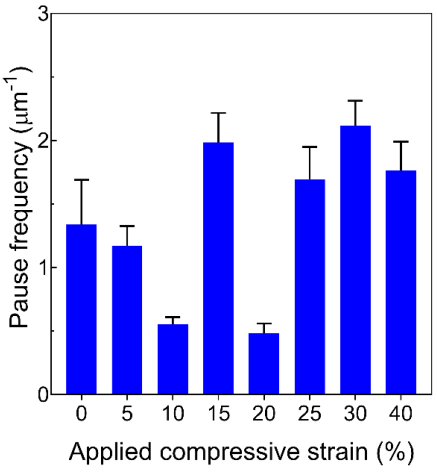

Figure 2.15 Effect of applied compressive strain on the pause frequency of dynein-driven cargo transportation along microtubules. No statistically significant change in the pausing frequency by dynein driven Qdots on buckled microtubules was observed when compared

to that on undeformed microtubules (Kruskal-Wallis non-parametric test and Dunn's multiple comparisons test at $P < 0.001$). Error bar: standard error.

The pause frequency of dynein during Qdot transportation along microtubules undergoing different applied compressive strains are shown in Figure 2.16. The pause frequency is defined by the number of pauses (i.e. stopping of the Qdot movement for at least 3 consecutive frames) per run exhibited by the Qdots while being transported.

2.2.4.4 Effect of applied compressive strain on microtubules on the run lengths of dynein-driven Qdot transportation

Next, I investigated how buckling of microtubule influenced the run length of dynein, the results of which are shown in Figure 2.17. To determine the mean run lengths of dyneins, cumulative distribution probability functions were used.

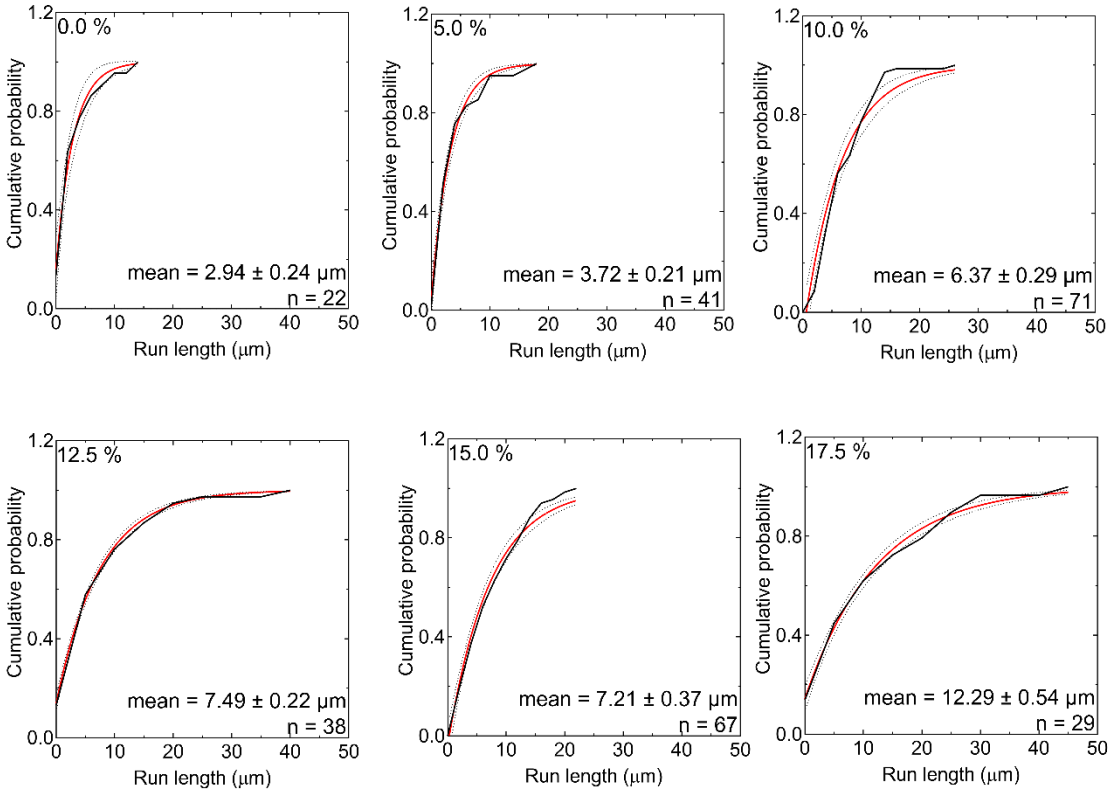

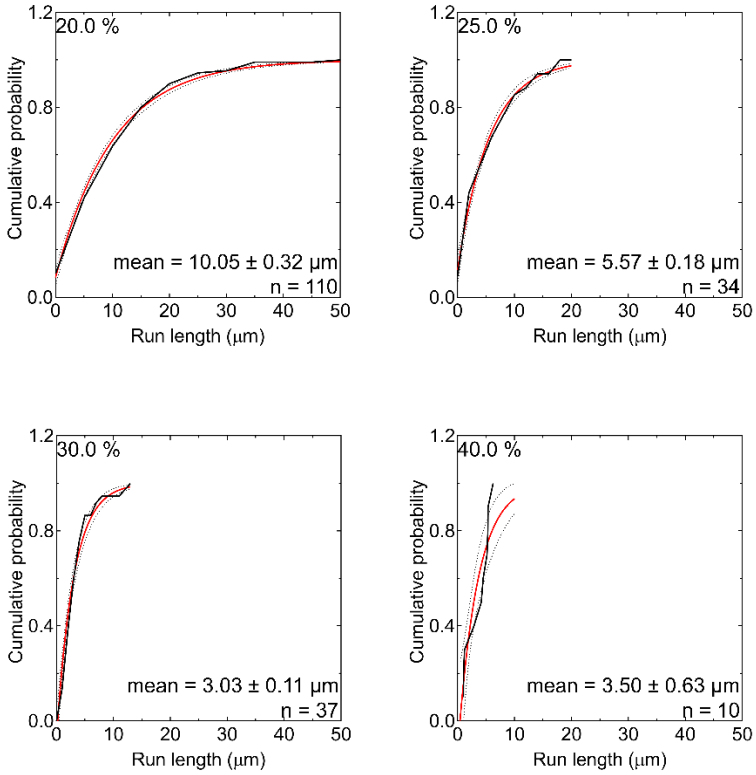

Figure 2.16 The cumulative probability distributions of run lengths of Qdot transported by dynein along undeformed (0.0 %) and buckled microtubules at different applied compressive strains (5.0 to 40.0 %). Mean run lengths are determined by non-linear least-squares fitting of the cumulative probability distribution of data to function: $Y = (1 - e^{\frac{x_o - x}{t}})$; where x_0 was set equal to the minimum value of the run-length analyzed in each case. The only fit parameter, decay constant, *t* is the required mean run length. Red solid lines represent the fitted curves and dotted lines denote the deviation in the fitting. The number of events analyzed and mean run lengths obtained from fitting are mentioned in the figure legends.

The run length of dynein-driven Qdots along undeformed microtubule obtained from fitting the cumulative probability of run length was 3.0 ± 0.2 µm (mean ± standard error, n = 22), which ensured the participation of multiple dynein motors to transport Qdot. [37]

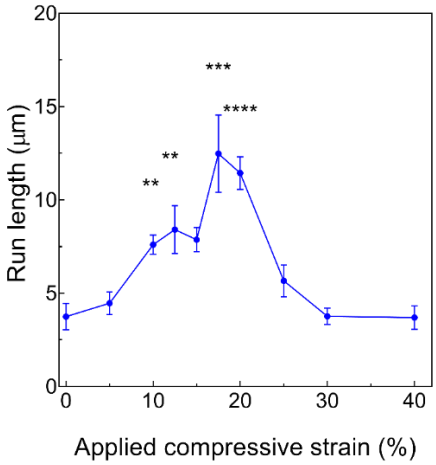

Figure 2.17 Change of run length of dynein upon buckling of microtubules under varied amount of applied strain. The differences in run lengths of dynein-driven Qdots along undeformed microtubules and those along buckled microtubules at different compressive strains were found to be statistically significant at **P < 0.01, ***P < 0.001 and ****P < 0.0001 using Kruskal-Wallis test followed by Dunn's multiple comparisons test. Mean run lengths were determined from the cumulative probability distribution of run lengths of dynein (Figure 2.20).

2.2.4.5 Binding affinity of dyneins to microtubules buckled at different compressive strains

The dyneins' affinity to bind to microtubules may be expected to be altered due to the deformation induced by buckling. For this, I determined the binding affinity of the Qdot conjugated dyneins as response to the buckling of microtubule. The binding affinity can be described by three important kinetic parameters of dynein- microtubule interaction, binding rate constant k_{on}, dissociation rate constant k_{off} and dissociation constant K_d.

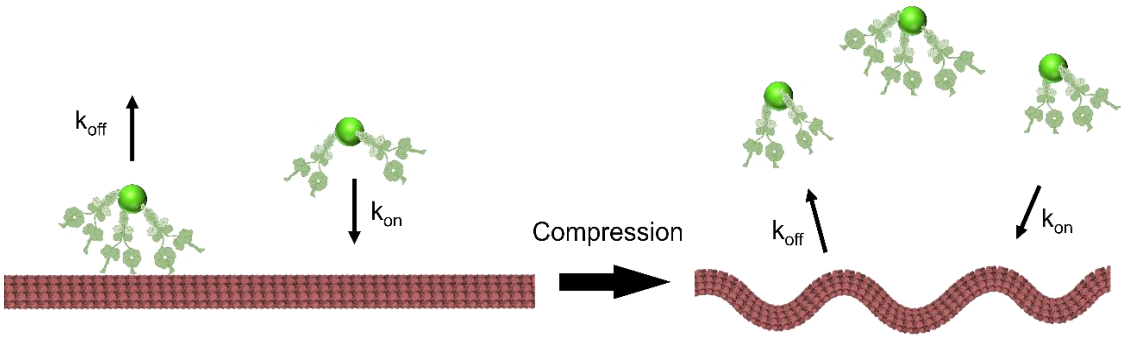

Figure 2.18 *Microtubule-Qdot binding*. Schematic model of the elementary reaction steps and kinetic parameters for binding of Qdot conjugated dyneins on microtubules. k_{on} is the association or binding rate constant and k_{off} is the dissociation or unbinding rate constant.

For a simple reversible reaction between proteins A and B, one can write:

$$A + B \rightleftharpoons AB \ldots\ldots\ldots\ldots\ldots (2.1)$$

Therefore,

$$[\mathrm{A}] + [\mathrm{B}] \underset{k_{\mathrm{off}}}{\overset{k_{\mathrm{on}}}{\rightleftharpoons}} [\mathrm{AB}] \ldots\ldots\ldots\ldots\ldots (2.2)$$

Here, [A] and [B] denote the concentrations of the free proteins (reactants), whereas [AB] denotes the concentration of their bound complex (product). k_{on} and k_{off} represent the association rate constant and the dissociation rate constant, respectively. In this study the k_{on} was defined as the number of dynein conjugated Qdots bound on the microtubule in a unit of Qdot concentration, microtubule length and time ($M^{-1}\mu m^{-1}s^{-1}$), as previously reported. [38,39] The dissociation rate constant, k_{off} was calculated as the reciprocal of mean binding time. [38,39]

When the system is at equilibrium, dissociation constant K_d is defined as

$$K_{\mathrm{d}} = \frac{[\mathrm{A}][\mathrm{B}]}{\mathrm{AB}} = \frac{k_{\mathrm{off}}}{k_{\mathrm{on}}} \ldots\ldots\ldots\ldots\ldots\ldots (2.3)$$

Now to determine the parameter k_{on}, number of dynein conjugated Qdots were counted from the fluorescence signal intensity on the microtubules. Length of each microtubule considered and time of observation of the Qdot on the microtubule were recorded. The concentration of Qdot applied in each experiment was 1 nM. The formula:

$$k_{on} = \frac{Number\ of\ Qdot-dynein\ conjugates\ on\ microtubule}{Concentration\ of\ Qdot \times Length\ of\ microtubule \times Time\ duration} \frac{1}{M.\mu m.s} \quad \ldots (2.4)$$

The k_{on} of Qdot-dynein binding to microtubules compressed at different compressive strains as determined are shown in the Figure 2.19.

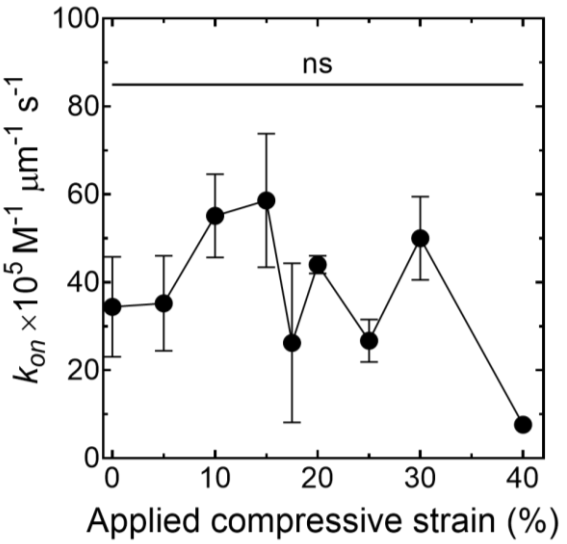

Figure 2.19 K_{on} values of Qdot-dynein binding to the microtubules in presence of different compressive strains. No significant difference in the values could be seen (One-way ANOVA). Number of microtubules analyzed in each case was 10.

Next, to determine k_{off} the mean binding time is required. The binding time was defined by the duration of time starting from attachment of the Qdots attached to dyneins to the microtubule to until when they were detached from the microtubules, or the imaging was finished. To determine the mean binding times, bin-independent cumulative probability distributions of the binding times were plotted (Figure 2.20). The distributions were fitted

to the function: $y = e^{\frac{x_0 - x}{t}}$; where, x_0 is the shortest binding time measured during analysis. The only fit parameter, the decay constant, t, gave the mean binding time in the distribution.

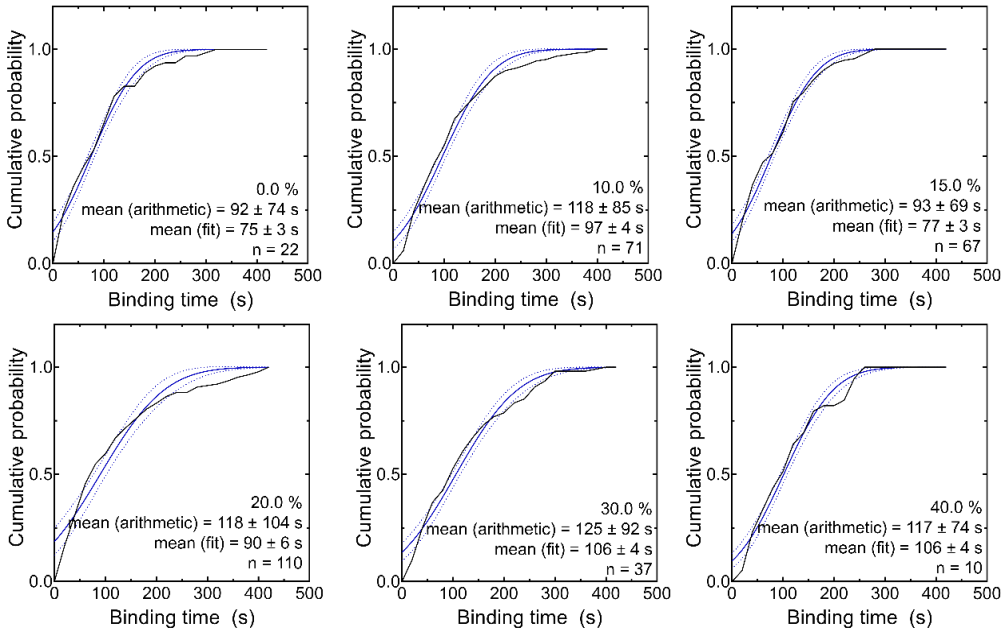

Figure 2.20 *The cumulative probability distribution of binding time.* The cumulative probability distribution of binding time of the Qdots conjugated with multiple dyneins on the microtubules at different compressive strains. The results obtained from analysis of the cases with applied compressive strains 0.0%, 10.0%, 15.0%, 20.0%, 30.0% and 40.0 % are shown in the figure as representatives. Events considered for this analysis are from one movie of each case.

The mean binding times obtained from each case were plotted in Figure 2.22 as a function of applied compressive strains which remained almost same for all cases.

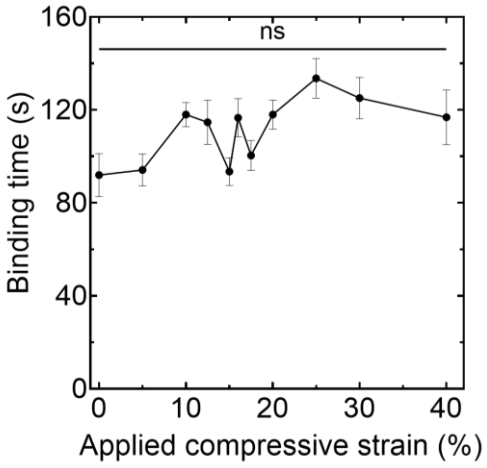

Figure 2.21 *Change of the mean binding time*. Change of the mean binding time of dynein as an effect of buckling of the microtubules under varied amount of applied strain. The differences in the binding time of dynein-conjugated Qdots on undeformed microtubules to those along the buckled microtubules at different compressive strains were found to have no statistical significance. Kruskal-Wallis test followed by Dunn's multiple comparisons test at P< 0.0001. ns = non-significant.

According to the equation 2.3, the dissociation constants, K_d at all compressive strains were determined and are presented in the Figure 2.22. The K_d values reflected altered binding affinity of Qdot-dynein conjugates with change in the buckling of microtubules.

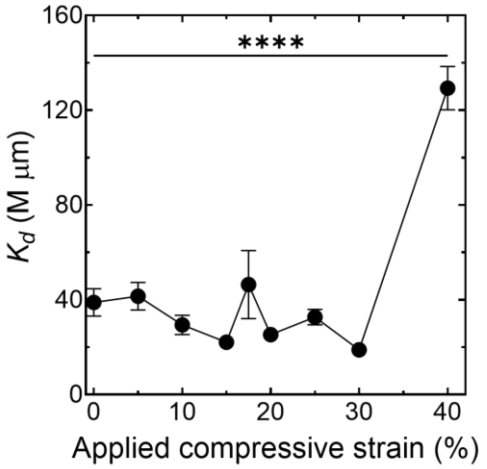

Figure 2.22 Change in K_d of Qdot-dynein conjugate binding to microtubules with increase in the applied compressive stain on the microtubule.

Interestingly, the K_d value did not vary significantly with increase in compressive strain on the microtubule until 40 % compressive strain was applied. Abrupt increase in the K_d value was significantly higher compared to the K_d at undeformed microtubule.

From the presented results, the response of dynein appears to be resilient in withstanding the effect of the transportation track. Dynein has a stochastic stepping mechanism with variable step sizes (8 - 40 nm) [33,34]. The highly scattered movement of dynein along the buckled microtubule may be related to its unusual stepping mechanism which might help dynein in withstanding the effect of adverse condition of microtubule track caused by buckling. Several mechanisms are thought to synergize with one another to indorse dynein molecules to step along microtubule. [36] The dynein motors are capable of switching to an adjacent protofilament track. [32] Therefore, dyneins exhibit robust behavior. [24,40] On the other hand, the microtubule, when buckled due to compression, are subject to expansion in their lattice. A recent study showed that expansion of a microtubule lattice could result into 0.13 nm increment in spacing per tubulin dimer [41]. The long 14 nm-stalk of dynein might allow it for a larger displacement of the microtubule binding domain [35] and thus help transportation along the deformed microtubule. Also, the presence of a flexible joint gives rise to an angle between the microtubule binding domain and binding stalk of the dynein [42]. Concomitantly the distorted geometry of the tubulin-sites in a deformed microtubule can affect the dynein molecule to adjust the angle between its microtubule binding domain and stalk and finally sustain its motility along the track. How the spatial arrangement of tubulins in a deformed microtubule favors the dynein's transportation behavior remains unclear at this moment and requires further investigation. Moreover, the anomalous nature in the change in dynein motility with applied compressive strains indicate toward the difference in the modes of the microtubule

deformation. This study may help understand the significance of buckled or curved microtubule in the cellular activities, as in many instances the microtubules are found buckled or curved in cells. [21,43] Since buckling of the microtubules often occurs at the periphery of cells, [43] these buckled microtubule interacting with dynein may play significant role in the precise positioning of the microtubule asters. [44,45] Moreover, the spatiotemporal synchronization of dynein and the buckled microtubule may also control the actomyosin network, movement of centrosomes and movement of nuclei, which consequently may affect the temporal synchronization of the movement of the cellular substances [46].

It has been reported that dynein-driven cargo transportation is more likely to overcome obstructions like passing through intersections than to switch track or reverse direction. [47] But how microtubule deformation caused by external stress can affect the dynein-driven transportation of the Qdots has not been addressed yet. The results discussed in this chapter might provide evidence for dynein's structural flexibility [48] and robustness [24,40] during their motility along the deformed microtubule tracks.

2.3 Conclusion

In conclusion, by employing a simple *in vitro* system, I systematically investigated the response of the microtubules to compressive stress applied along their horizontal axis and its consequent impact on their functionalities in the dynein-driven transportation. The results show that microtubule may possess mechano-sensing property, by which they can affect the dynamics of motor protein driven transportation. The modulated dynamics of dynein-driven transportation upon buckling of the microtubule seems to be the signature of altered dynamics of the dynein motors along the deformed microtubule. This altered dynamics might also be considered as the basis for other regulatory mechanisms such as the regulation of cellular activities by post-translational modifications of tubulins. [49] This work offers a technical advantage for systematic study of the correlation between deformation of microtubule and its biological functions i.e., cargo-transportation, as well as an opportunity to explore the interaction of deformed microtubule with microtubule associated proteins such as MAP1, MAP2, MAP4, Tau, Katanin etc. These results will expectedly enrich the current understanding of cellular mechanotransduction [50] and foster the design principle for mechanoresponsive functional materials inspired by nature. [51]

2.4. Experimental procedures

2.4.1. Purification, labeling, and polymerization of tubulin

Tubulin was purified from the fresh porcine brain using a high-concentration PIPES buffer (1 M PIPES, 20 mM EGTA, 10 mM $MgCl_2$; pH adjusted to 6.8 using KOH). [52] Rhodamine-labeled tubulin (RT) was prepared using 5/6-carboxy-tetramethyl-rhodamine succinimidyl ester (TAMRA-SE; Invitrogen) according to the standard technique. [53] The labeling ratio was 1.0 as determined from the absorbance of tubulin at 280 nm and tetramethyl-rhodamine at 555 nm. A mixture of RT and non-labelled tubulin (WT) (where, RT:WT = 4:1; final tubulin concentration = 55.6 μM) was polymerized at 37 °C in presence of 5 mM GTP, 20 mM $MgCl_2$, 25% DMSO in BRB80. The microtubule was paclitaxel-stabilized (50 μM paclitaxel in BRB80; pH 6.8).

2.4.2. Expression and purification of motor protein

Recombinant conventional kinesin-1 construct consisting of human kinesin (residues 1-573) was expressed and purified to serve as anchor kinesin to fix microtubule on the substrate. Another kinesin-1 construct consisting of human kinesin (residues 1-465). The expression and purification of kinesins were done as described in previously published reports with partial modification. [23] SNAP-tagged full-length dynein was purified as described in literature. [29]

2.4.3. Preparation of PDMS thin film

The precursor of PDMS (Silpot 184®, Dow Corning Toray Co. Ltd.) and cross-linker (Catalyst of Silpot 184®) were mixed at a ratio of 10:1 (w/w). The mixture was diluted to 1:10 (w/w) using hexane. After shaking followed by degassing in vacuum for an hour,

the mixture was spin coated on a Teflon® sheet at 1500 rpm for 30 seconds to ensure even coating. The spin coated sheets were cured at 60 ºC for 4-6 hours to allow polymerization in to PDMS and complete evaporation of hexane. The thin PDMS film was peeled off from the Teflon® sheet and was etched by a plasma etcher (SEDE-GE; Meiwafosis Co. Ltd.) (6-8 Pa, 8 mA, 4 minutes) prior to an experiment.

2.4.4. Qdot transportation assay by dynein

In vitro Qdot assays along microtubule were performed on PDMS using a recently developed micro-stretcher. [16,17] The micro-stretcher consists of a cover plate and a base plate containing a computer-controlled stretcher/compressor. First, a small piece of PDMS with approximate dimension 4.0×5.0×0.05 mm^3 (L×W×T) was fixed horizontally on the stretcher of the chamber. Then the film was elongated 100% by applying tensile force with the computer-controlled stretcher. The length of the PDMS film was doubled at this point. The elongated PDMS was masked with two 18×18 cover glasses leaving a narrow channel to be used as flow cell. This channel was exposed to air plasma for 4 minutes (10 Pa, 8 mA) in a plasma etcher (SEDE-GE; Meiwafosis Co. Ltd.) to increase its hydrophilicity, thus was ready to be used for preparing flow cell. At first, 10 µL of 100 nM *anchor kinesin* in preKG solution (~80 mM PIPES, ~40 mM NaCl, 1 mM EGTA, 1 mM $MgCl_2$, 1 mM DTT, 10 mM paclitaxel; pH 6.8) was introduced to the flow cell and incubated for 5 minutes. The flow cell was washed with motility buffer (~80 mM PIPES, 1 mM EGTA, 1 mM $MgCl_2$, 0.5 mg/mL casein, 1 mM DTT, 10 mM paclitaxel; pH 6.8). Next, paclitaxel-stabilized, rhodamine labelled 280 nM 20 µL microtubule solution was introduced and incubated for 5 minutes, followed by washed with motility buffer. In this work, microtubule was deposited on the PDMS substrate via interaction with the *anchor*

kinesins in absence of any nucleotide. Shear flow was used to apply microtubule solution from one end of the narrow flow cell so that the microtubules align parallelly to the stretch axis. Therefore, when the tensile stress at the elongated PDMS was released by compression of stretcher (strain rate 0.42% s^{-1}) it consequently produced compressive stress on the microtubule attached to the PDMS. The parallel arrangement of microtubule allowed them to undergo buckling i.e. deformation along their longitudinal axis. After the buckling was ensured, microtubules were chemically immobilized by exposure to 0.1% (v/v) glutaraldehyde for 4 minutes. The glutaraldehyde fixing reaction was quenched by 0.1 M glycine and incubation of 5 minutes. The glutaraldehyde treatment was mild enough to microtubule such that it had no effect on the motor protein-based cargo transportation (Section 2.2.3.2). To observe Qdot transportation by dynein along these buckled microtubule, pre-incubated solution of Qdot-dynein conjugates (details of preparation given later) was passed into the flow cell. The micro-stretcher was then sealed, and humid nitrogen gas was continuously purged through the micro-stretcher until the experiment was completed. All experiments were performed at 25 °C.

2.4.5. Preparation of dynein-cargo conjugate

For dynein based Qdot transportation, the cargo was benzylguanine-functionalized Qdots (BG-Qdot) that can covalently bind to the SNAP-tagged dynein motors through BG-SNAP interaction. To obtain Qdot-dynein conjugates, dynein and Qdot were mixed at a molar concentration ratio ≈ 1:10 and incubated at room temperature for 30 minutes. The applied concentrations of Qdot and dynein to the flow cell were 1 and 10 nM respectively as diluted by ATP solution (1 mM ATP, 1% Pluronic F127, 1 mg/mL casein, 20 mM

DTT, 10 µM paclitaxel in BRB80, and assay buffer having 20 mM PIPES, 4 mM $MgSO_4$, 10 mM K-acetate, 1 mM EGTA; pH 6.8).

2.4.7. Microscopy image capture and data analysis

Samples were illuminated with a 100 W mercury lamp and visualized by two-color epi-fluorescence microscope (Eclipse Ti; Nikon) equipped with an oil-coupled Plan Apo 60×1.40 objective (Nikon). Filter blocks with UV-cut specification (TRITC: EX540/25, DM565, BA606/55; Q525: EX435/40, DM510, 525/15; Nikon) were used in the optical path of the microscope that allowed visualization of samples eliminating the UV part of radiation and minimized the harmful effect of UV radiation on samples. Images were captured using a cooled CMOS camera (Neo CMOS; Andor) connected to a PC. To capture images of microtubule and Qdots for several minutes, ND4 (25% transmittance) and ND1 (100% transmittance) respectively were inserted into the illuminating light path of the fluorescence microscope to avoid photobleaching. Observation of Qdot assay was performed by capturing images and movies at a rate of 1 frame/3 s with exposure time of 300 ms for dynein-based experiments. All movies captured by the epi-fluorescence microscope were analyzed by image analysis software (ImageJ 1.46r). The trajectories of the Qdots transported by the motors were tracked manually using an ImageJ plug-in MTrackJ. The Qdots that could be traced on microtubule for over 4 frames were tracked for analysis. For measurement of strain, length of pre-stretched PDMS (8.0 mm) was considered as the initial length and the percentage of the strain experienced by microtubule on PDMS was calculated accordingly.

2.4.7. Estimation of mean velocity, run length, and pause frequency of dynein

Velocities were determined by tracking the movement of Qdots using ImageJ software. Mean run length of dynein during transporting Qdot along undeformed and deformed microtubule at different compressive strain have been determined using the bin-independent cumulative probability distribution. To determine the run length (x), non-linear least-squares fitting of the cumulative probability distribution to the function [54]: $Y = 1 - \exp(\frac{(x_0 - x)}{t})$, was performed. x_0 is the lowest run length measured during analysis. The only fit parameter, the decay constant, t, gave the mean run length in the distribution. Pause frequency was calculated according to the literature where the total number of the pause (at 3s time interval the Qdot displacement ≤0.110 μm) was divided by the total distance travelled by the Qdot (run length) [26]. The Qdot displacement of ≤0.110 μm corresponds to the minimum pixel which is available in our experimental system.

2.4.8. Curvature analysis

For this analysis, the coordinates of equally spaced points on the centerline of the buckled microtubules were divided into several sections. A custom-written MATLAB code fitted the coordinates to a half circle and obtained the coordinate of the circle and the radius of the curvature. Curvature was obtained by inverting the radius of curvature, since, curvature $= \frac{1}{radius\ of\ curvature}$..

2.4.9. Statistical analysis

Statistical analyses were performed with GraphPad Prism (www.graphpad.com). A two-tailed Student's t-test was used to compare two groups. One-way ANOVA followed by

Tukey's multiple comparison test was used to compare among three or more groups of normally distributed data. Kruskal-Wallis test followed by Dunn's multiple comparison test was used to compare among three or more groups of non-normal data. The values for the number of events, *P*-value, and name of the statistical test performed for each analysis are included in the figure legend or in the caption.

2.5. Results of statistical analysis

Statistical analysis of all data mentioned in this chapter were carried out using the software GraphPad Prism 8.1.0. Below are the results of all relevant analysis in the sequence as they appear in the chapter.

Table 2.5.1. Results of statistical analysis of velocities of dynein-driven Qdot transportation along the microtubules under applied compressive strain**.** Kruskal-Wallis test followed by Dunn's multiple comparison test was used to compare among the velocities of dynein based Qdot transportation along microtubule compressed at different compressive stresses. (From data in Figure 2.14)

Number of families	1		
Number of comparisons per family	66		
Alpha	0.001		
Dunn's multiple comparisons tests	Mean rank diff.	Summary	Adjusted P-Value
0.0 % vs. 5.0 %	-134.9	ns	>0.9999
0.0 % vs. 10.0 %	-454.2	****	<0.0001
0.0 % vs. 12.5 %	-285.5	*	0.0207
0.0 % vs. 14.0 %	-210.7	ns	0.1834
0.0 % vs. 15.0 %	-447.6	****	<0.0001
0.0 % vs. 16.0 %	-610.4	****	<0.0001
0.0 % vs. 17.5 %	-580.8	****	<0.0001
0.0 % vs. 20.0 %	-462.1	****	<0.0001
0.0 % vs. 25.0 %	36.42	ns	>0.9999
0.0 % vs. 30.0 %	203.0	ns	0.3432
0.0 % vs. 40.0 %	66.12	ns	>0.9999
5.0 % vs. 10.0 %	-319.3	****	<0.0001
5.0 % vs. 12.5 %	-150.6	ns	>0.9999
5.0 % vs. 14.0 %	-75.86	ns	>0.9999

5.0 % vs. 15.0 %	-312.7	****	<0.0001
5.0 % vs. 16.0 %	-475.5	****	<0.0001
5.0 % vs. 17.5 %	-445.9	****	<0.0001
5.0 % vs. 20.0 %	-327.2	****	<0.0001
5.0 % vs. 25.0 %	171.3	ns	0.1691
5.0 % vs. 30.0 %	337.9	****	<0.0001
5.0 % vs. 40.0 %	201.0	ns	0.9740
10.0 % vs. 12.5 %	168.7	ns	0.4320
10.0 % vs. 14.0 %	243.5	****	<0.0001
10.0 % vs. 15.0 %	6.569	ns	>0.9999
10.0 % vs. 16.0 %	-156.2	ns	0.2814
10.0 % vs. 17.5 %	-126.6	ns	0.8334
10.0 % vs. 20.0 %	-7.900	ns	>0.9999
10.0 % vs. 25.0 %	490.6	****	<0.0001
10.0 % vs. 30.0 %	657.2	****	<0.0001
10.0 % vs. 40.0 %	520.3	****	<0.0001
12.5 % vs. 14.0 %	74.76	ns	>0.9999
12.5 % vs. 15.0 %	-162.1	ns	>0.9999
12.5 % vs. 16.0 %	-324.9	***	0.0004
12.5 % vs. 17.5 %	-295.3	**	0.0013
12.5 % vs. 20.0 %	-176.6	ns	0.2746
12.5 % vs. 25.0 %	321.9	***	0.0003
12.5 % vs. 30.0 %	488.5	****	<0.0001
12.5 % vs. 40.0 %	351.6	**	0.0095
14.0 % vs. 15.0 %	-236.9	**	0.0026
14.0 % vs. 16.0 %	-399.7	****	<0.0001
14.0 % vs. 17.5 %	-370.0	****	<0.0001
14.0 % vs. 20.0 %	-251.4	****	<0.0001
14.0 % vs. 25.0 %	247.1	**	0.0030
14.0 % vs. 30.0 %	413.7	****	<0.0001
14.0 % vs. 40.0 %	276.9	ns	0.0751
15.0 % vs. 16.0 %	-162.8	ns	0.5280
15.0 % vs. 17.5 %	-133.1	ns	>0.9999
15.0 % vs. 20.0 %	-14.47	ns	>0.9999
15.0 % vs. 25.0 %	484.0	****	<0.0001

15.0 % vs. 30.0 %	650.6	****	<0.0001
15.0 % vs. 40.0 %	513.7	****	<0.0001
16.0 % vs. 17.5 %	29.65	ns	>0.9999
16.0 % vs. 20.0 %	148.3	ns	0.4090
16.0 % vs. 25.0 %	646.8	****	<0.0001
16.0 % vs. 30.0 %	813.4	****	<0.0001
16.0 % vs. 40.0 %	676.5	****	<0.0001
17.5 % vs. 20.0 %	118.7	ns	>0.9999
17.5 % vs. 25.0 %	617.2	****	<0.0001
17.5 % vs. 30.0 %	783.8	****	<0.0001
17.5 % vs. 40.0 %	646.9	****	<0.0001
20.0 % vs. 25.0 %	498.5	****	<0.0001
20.0 % vs. 30.0 %	665.1	****	<0.0001
20.0 % vs. 40.0 %	528.2	****	<0.0001

Table 2.5.2. Results of statistical analysis of run lengths of dynein-driven Qdot transportation along deformed microtubule. One-way ANOVA followed by Tukey's multiple comparison test was used to compare among the pause frequencies of dynein based Qdot transportation along microtubule compressed at different compressive strains. (From data in Figure 2.18).

Number of families	1		
Number of comparisons per family	66		
Alpha	0.001		
Dunn's multiple comparisons test	Mean rank diff.	Summary	Adjusted P Value
0.0 % vs. 5.0 %	-72.68	ns	>0.9999
0.0 % vs. 10.0 %	-470.2	****	<0.0001
0.0 % vs. 12.5 %	-360.1	****	<0.0001
0.0 % vs. 14.0 %	-354.8	****	<0.0001
0.0 % vs. 15.0 %	-319.9	****	<0.0001
0.0 % vs. 16.0 %	-565.8	****	<0.0001
0.0 % vs. 17.5 %	-495.1	****	<0.0001
0.0 % vs. 20.0 %	-501.6	****	<0.0001
0.0 % vs. 25.0 %	-204.6	*	0.0200
0.0 % vs. 30.0 %	-20.26	ns	>0.9999
0.0 % vs. 40.0 %	-134.9	ns	>0.9999
5.0 % vs. 10.0 %	-397.5	****	<0.0001
5.0 % vs. 12.5 %	-287.5	****	<0.0001
5.0 % vs. 14.0 %	-282.1	****	<0.0001
5.0 % vs. 15.0 %	-247.2	****	<0.0001
5.0 % vs. 16.0 %	-493.2	****	<0.0001
5.0 % vs. 17.5 %	-422.4	****	<0.0001
5.0 % vs. 20.0 %	-428.9	****	<0.0001
5.0 % vs. 25.0 %	-132.0	ns	0.2034
5.0 % vs. 30.0 %	52.42	ns	>0.9999
5.0 % vs. 40.0 %	-62.24	ns	>0.9999
10.0 % vs. 12.5 %	110.0	ns	>0.9999
10.0 % vs. 14.0 %	115.3	ns	>0.9999

10.0 % vs. 15.0 %	150.3	*	0.0293
10.0 % vs. 16.0 %	-95.67	ns	>0.9999
10.0 % vs. 17.5 %	-24.92	ns	>0.9999
10.0 % vs. 20.0 %	-31.45	ns	>0.9999
10.0 % vs. 25.0 %	265.5	****	<0.0001
10.0 % vs. 30.0 %	449.9	****	<0.0001
10.0 % vs. 40.0 %	335.2	****	<0.0001
12.5 % vs. 14.0 %	5.326	ns	>0.9999
12.5 % vs. 15.0 %	40.24	ns	>0.9999
12.5 % vs. 16.0 %	-205.7	*	0.0183
12.5 % vs. 17.5 %	-134.9	ns	0.8536
12.5 % vs. 20.0 %	-141.5	ns	0.7340
12.5 % vs. 25.0 %	155.5	ns	0.3310
12.5 % vs. 30.0 %	339.9	****	<0.0001
12.5 % vs. 40.0 %	225.2	ns	0.1268
14.0 % vs. 15.0 %	34.92	ns	>0.9999
14.0 % vs. 16.0 %	-211.0	*	0.0222
14.0 % vs. 17.5 %	-140.3	ns	0.8773
14.0 % vs. 20.0 %	-146.8	ns	0.7534
14.0 % vs. 25.0 %	150.2	ns	0.6132
14.0 % vs. 30.0 %	334.6	****	<0.0001
14.0 % vs. 40.0 %	219.9	ns	0.2055
15.0 % vs. 16.0 %	-245.9	****	<0.0001
15.0 % vs. 17.5 %	-175.2	**	0.0073
15.0 % vs. 20.0 %	-181.7	**	0.0074
15.0 % vs. 25.0 %	115.3	ns	0.8924
15.0 % vs. 30.0 %	299.6	****	<0.0001
15.0 % vs. 40.0 %	185.0	ns	0.3417
16.0 % vs. 17.5 %	70.75	ns	>0.9999
16.0 % vs. 20.0 %	64.23	ns	>0.9999
16.0 % vs. 25.0 %	361.2	****	<0.0001
16.0 % vs. 30.0 %	545.6	****	<0.0001
16.0 % vs. 40.0 %	430.9	****	<0.0001
17.5 % vs. 20.0 %	-6.522	ns	>0.9999
17.5 % vs. 25.0 %	290.4	****	<0.0001

17.5 % vs. 30.0 %	474.8	****	<0.0001
17.5 % vs. 40.0 %	360.2	****	<0.0001
20.0 % vs. 25.0 %	297.0	****	<0.0001
20.0 % vs. 30.0 %	481.3	****	<0.0001
20.0 % vs. 40.0 %	366.7	****	<0.0001
25.0 % vs. 30.0 %	184.4	*	0.0131
25.0 % vs. 40.0 %	69.72	ns	>0.9999
30.0 % vs. 40.0 %	-114.7	ns	>0.9999

2.6. References

1. Lecuit, T. & Lenne, P. F. Cell surface mechanics and the control of cell shape, tissue patterns and morphogenesis. *Nat. Rev. Mol. Cell Biol.* **8**, 633–644 (2007).
2. Le, H. Q. *et al.* Mechanical regulation of transcription controls Polycomb-mediated gene silencing during lineage commitment. *Nat. Cell Biol.* **18**, 864–875 (2016).
3. Matthews, B. D. Cellular adaptation to mechanical stress: role of integrins, Rho, cytoskeletal tension and mechanosensitive ion channels. *J. Cell Sci.* **119**, 508–518 (2006).
4. Barnes, J. M., Przybyla, L. & Weaver, V. M. Tissue mechanics regulate brain development, homeostasis and disease. *J. Cell Sci.* **130**, 71–82 (2017).
5. Booth, I. R. & Blount, P. The MscS and MscL families of mechanosensitive channels act as microbial emergency release valves. *J. Bacteriol.* **194**, 4802–4809 (2012).
6. Redmon, S. N., Shibasaki, K. & Križaj, D. Transient Receptor Potential Cation Channel Subfamily V Member 4 (TRPV4). in *Encyclopedia of Signaling Molecules* (ed. Choi, S.) 5665–5675 (Springer International Publishing, 2018). doi:10.1007/978-3-319-67199-4_101977
7. Janoštiak, R., Pataki, A. C., Brábek, J. & Rösel, D. Mechanosensors in integrin signaling: The emerging role of p130Cas. *Eur. J. Cell Biol.* **93**, 445–454 (2014).
8. Yao, M. *et al.* The mechanical response of talin. *Nat. Commun.* **7**, 11966 (2016).
9. Tremblay, D., Andrzejewski, L., Leclerc, A. & Pelling, A. E. Actin and microtubules play distinct roles in governing the anisotropic deformation of cell nuclei in response to substrate strain. *Cytoskeleton* **70**, 837–848 (2013).
10. Hayakawa, K., Tatsumi, H. & Sokabe, M. Actin filaments function as a tension sensor by tension-dependent binding of cofilin to the filament. *J. Cell Biol.* **195**, 721–727 (2011).
11. Luo, T., Mohan, K., Iglesias, P. A. & Robinson, D. N. Molecular mechanisms of cellular mechanosensing. *Nat. Mater.* **12**, 1064–1071 (2013).
12. Uyttewaal, M. *et al.* Mechanical stress acts via katanin to amplify differences in growth rate between adjacent cells in Arabidopsis. *Cell* **149**, 439–451 (2012).
13. Schaap, I. A. T., Carrasco, C., de Pablo, P. J., MacKintosh, F. C. & Schmidt, C. F. Elastic response, buckling, and instability of microtubules under radial indentation. *Biophys. J.* **91**, 1521–1531 (2006).
14. Schaedel, L. *et al.* Microtubules self-repair in response to mechanical stress. *Nat. Mater.* **14**, 1156–1163 (2015).
15. Ahmed, W. W. & Saif, T. A. Active transport of vesicles in neurons is modulated

by mechanical tension. *Sci. Rep.* **4**, 4481 (2014).
16. Kabir, A. M. R. *et al.* Biomolecular motor modulates mechanical property of microtubule. *Biomacromolecules* **15**, 1797–1805 (2014).
17. Kabir, A. M. R. *et al.* Buckling of Microtubules on a 2D Elastic Medium. *Sci. Rep.* **5**, 1–12 (2015).
18. Wang, N., Butler, J. P. & Ingber, D. E. Mechanotransduction across the cell surface and through the cytoskeleton. *Science* **260**, 1124–1127 (1993).
19. Jin, M. Z. & Ru, C. Q. Localized buckling of a microtubule surrounded by randomly distributed cross linkers. *Phys. Rev. E - Stat. Nonlinear, Soft Matter Phys.* **88**, 1–8 (2013).
20. Tang-Schomer, M. D., Patel, A. R., Baas, P. W. & Smith, D. H. Mechanical breaking of microtubules in axons during dynamic stretch injury underlies delayed elasticity, microtubule disassembly, and axon degeneration. *FASEB J.* **24**, 1401–1410 (2010).
21. Robison, P. *et al.* Detyrosinated microtubules buckle and bear load in contracting cardiomyocytes. *Science* **352**, aaf0659 (2016).
22. Tang-Schomer, M. D., Johnson, V. E., Baas, P. W., Stewart, W. & Smith, D. H. Partial interruption of axonal transport due to microtubule breakage accounts for the formation of periodic varicosities after traumatic axonal injury. *Exp. Neurol.* **233**, 364–372 (2012).
23. Fujimoto, K. *et al.* Colocalization of quantum dots by reactive molecules carried by motor proteins on polarized microtubule arrays. *ACS Nano* **7**, 447–455 (2013).
24. Rai, A. A. K., Ramaiya, A. J., Jha, R. & Mallik, R. Molecular adaptations allow dynein to generate large collective forces inside cells. *Cell* **152**, 172–182 (2013).
25. Vale, R. D., Reese, T. S. & Sheetz, M. P. Identification of a novel force-generating protein, kinesin, involved in microtubule-based motility. *Cell* **42**, 39–50 (1985).
26. Conway, L., Wood, D., Tuzel, E. & Ross, J. L. Motor transport of self-assembled cargos in crowded environments. *Proc. Natl. Acad. Sci.* **109**, 20814–20819 (2012).
27. Fujimoto, K. *et al.* Colocalization of Quantum Dots by Reactive Molecules Carried by Motor Proteins on Polarized Microtubule Arrays. *ACS Nano* **7**, 447–455 (2013).
28. Sikora, A. *et al.* Behavior of Kinesin Driven Quantum Dots Trapped in a Microtubule Loop. *ACS Nano* **9**, 11003–11013 (2015).
29. Torisawa, T. *et al.* Autoinhibition and cooperative activation mechanisms of cytoplasmic dynein. *Nat. Cell Biol.* **16**, 1118–1124 (2014).
30. Mallik, R., Petrov, D., Lex, S. A., King, S. J. & Gross, S. P. Building complexity: An in vitro study of cytoplasmic dynein with in vivo implications. *Curr. Biol.* **15**,

2075–2085 (2005).
31. Shtridelman, Y., Cahyuti, T., Townsend, B., Dewitt, D. & C, J. Force-Velocity Curves of Motor Proteins Cooperating In Vivo. *Cell Biochem Biophys* **52**, 19–29 (2008).
32. Reck-Peterson, S. L. *et al.* Single-molecule analysis of dynein processivity and stepping behavior. *Cell* **126**, 335–348 (2006).
33. DeWitt, M. A., Chang, A. Y., Combs, P. A. & Yildiz, A. Cytoplasmic dynein moves through uncoordinated stepping of the AAA+ ring domains. *Sciene* **335**, 221–225 (2012).
34. Qiu, W. *et al.* Dynein achieves processive motion using both stochastic and coordinated stepping. *Nat. Struct. Mol. Biol.* **19**, 193–200 (2012).
35. Cleary, F. B. *et al.* Tension on the linker gates the ATP-dependent release of dynein from microtubules. *Nat. Commun.* **5**, 4587 (2014).
36. Bhabha, G., Johnson, G. T., Schroeder, C. M. & Vale, R. D. How dynein moves along microtubules. *Trends Biochem. Sci.* **41**, 94–105 (2016).
37. Wang, Z., Khan, S. & Sheetz, M. P. Single cytoplasmic dynein molecule movements: characterization and comparison with kinesin. *Biophys. J.* **69**, 2011–2023 (1995).
38. Shibafuji, Y. *et al.* Single-molecule imaging analysis of elementary reaction steps of trichoderma reesei cellobiohydrolase i (Cel7A) hydrolyzing crystalline cellulose Iα and IIII. *J. Biol. Chem.* **289**, 14056–14065 (2014).
39. Nakamura, A. *et al.* Rate constants, processivity, and productive binding ratio of chitinase A revealed by single-molecule analysis. *Phys. Chem. Chem. Phys.* **20**, 3010–3018 (2018).
40. Vershinin, M., Xu, J., Razafsky, D. S., King, S. J. & Gross, S. P. Tuning microtubule-based transport through filamentous MAPs: the problem of dynein. *Traffic* **9**, 882–892 (2008).
41. Peet, D. R., Burroughs, N. J. & Cross, R. A. Kinesin expands and stabilizes the GDP-microtubule lattice. *Nat. Nanotechnol.* **13**, 386–391 (2018).
42. Imai, H. *et al.* Direct observation shows superposition and large scale flexibility within cytoplasmic dynein motors moving along microtubules. *Nat. Commun.* **6**, 8179 (2015).
43. Brangwynne, C. P. *et al.* Microtubules can bear enhanced compressive loads in living cells because of lateral reinforcement. *J. Cell Biol.* **173**, 733–741 (2006).
44. Laan, L. *et al.* Cortical dynein controls microtubule dynamics to generate pulling forces that position microtubule asters. *Cell* **148**, 502–514 (2012).

45. Letort, G., Nedelec, F., Blanchoin, L. & Théry, M. Centrosome centering and decentering by microtubule network rearrangement. *Mol. Biol. Cell* **27**, 2833–2843 (2016).
46. De Simone, A., Nedelec, F. & Gonczy, P. Dynein transmits polarized actomyosin cortical flows to promote centrosome separation. *Cell Rep.* **14**, 2250–2262 (2016).
47. Ross, J. L., Shuman, H., Holzbaur, E. L. F. & Goldman, Y. E. Kinesin and dynein-dynactin at intersecting microtubules: motor density affects dynein function. *Biophys. J.* **94**, 3115–3125 (2008).
48. Chowdhury, S., Ketcham, S. A., Schroer, T. A. & Lander, G. C. Structural organization of the dynein–dynactin complex bound to microtubules. *Nat. Struct. &Amp; Mol. Biol.* **22**, 345–347 (2015).
49. Sirajuddin, M., Rice, L. M. & Vale, R. D. Regulation of microtubule motors by tubulin isotypes and post-translational modifications. *Nat. Cell Biol.* **16**, 335–344 (2014).
50. Prosser, B. L., Ward, C. W. & Lederer, W. J. X-ROS signaling: rapid mechano-chemo transduction in heart. *Science* **333**, 1440–1445 (2011).
51. Prince, E. & Kumacheva, E. Design and applications of man-made biomimetic fibrillar hydrogels. *Nat. Rev. Mater.* **4**, 99–115 (2019).
52. Castoldi, M. & Popov, A. V. Purification of brain tubulin through two cycles of polymerization-depolymerization in a high-molarity buffer. *Protein Expr. Purif.* **32**, 83–88 (2003).
53. Peloquin, J., Komarova, Y. & Borisy, G. Conjugation of fluorophores to tubulin. *Nat. Methods* **2**, 299–303 (2005).
54. Thorn, K. S., Ubersax, J. A. & Vale, R. D. Engineering the processive run length of the kinesin motor. *J. Cell Biol.* **151**, 1093–1100 (2000).

Chapter 3

High-Resolution Observation of Effect of Microtubule Bending on the Single Kinesin Moving along Microtubule

Abstract

In this chapter, the observation of translocation of single kinesins, a major microtubule associated motor protein, along microtubule using the high-speed atomic force microscopy (HS -AFM) is described. A new approach to cause deformation of microtubule on mica supported lipid bilayer has been established. The movement of kinesins on the undeformed straight microtubule and deformed microtubule were exploited by modifying the substrate conditions. A comparison has been made between the transportation behavior of kinesin along them. This study showed that kinesin-microtubule interaction was varied in a curvature dependent manner. The effect of bending of the microtubule on the kinesin-microtubule interaction was confirmed from the alteration in velocity, binding time or traveled distance of the kinesin while moving along the bent microtubules. The kinetic parameters, like, binding on and off-rate constants, (k_{on}, k_{off}) and the dissociation constant, (K_d) of kinesin binding to the microtubules were determined. The binding affinity of kinesin to the bent microtubule was higher compared to the straight one. This finding will expand the outlook of how alteration in any parameter defining the cellular environment may impose an impact on cellular activities.

3.1. Introduction

Microtubules are crucial to the survival of living cells due to their involvement in a number of cellular activities like growth, development, and migration [1–3]. They are the most rigid of all filaments of the cytoskeleton, [4] with a large aspect ratio [5] (> 100). Active participation of microtubules is required in cell contractility[6], maintenance of cell polarity[7], regulation of cell morphology and cell mechanics. [8,9] Cargo transportation is an important process which involves the transportation of materials, like protein complexes, enzymes, secretory vesicles, and organelles essential, to different parts in the cell for executing intracellular reactions. [10,11] To accomplish this function, the microtubules serve as tracks while as vehicles, the microtubule-associated motor proteins such as kinesin and dynein families carry cargos, as vehicles. Processive walk of these motor proteins along the microtubules are coupled to conversion of chemical energy from ATP hydrolysis.

In vivo microtubules are subject to bending [12,13] or buckling [14,15] while participating in cellular activities. The deformations may occur as a response to internally generated force developed primarily from deflection of tip of the microtubules [16] which may be amplified by compressive stress when the tip reaches the cell periphery [15] or even by the activity of kinesin [17–19] or dynein [20]. External mechanical impact applied on the microtubule by, for example, actomyosin contractility, [19,21,22] axonal damage or traumatic injury [23–25] may also result in their bending. The physiological importance of bending of microtubules is highlighted as it may cause breakage and contribute to the maintenance of cell polarity. [22] Bending of a microtubule can increase its lattice energy and thereby affect important microtubule-associated events, like microtubule depolymerization. [12,26] Kinesin-related protein kip3 is shown to mediate curvature sensitive bending of microtubules and facilitate the breakdown of curved microtubule assemblies during cell division. [27] The intracellular cargo transportation is also expected to be impaired by the bending of the track, since the example of how a defect in microtubule structure affects kinesin transportation is available. [28,29] Despite extensive characterization of bending [30] or buckling [31] of the microtubule, what effect these may impose on kinesin transportation remains unexplored. The kinesin-microtubule interaction in cells and *in vitro* have been addressed fairly well, [32–34] the effect of the deformation of microtubule on transportation of kinesin along them is still left unexplored. So far, using fluorescence microscopy

impeded cargo transportation by multiple kinesins or dyneins along microtubules deformed under compressive stress was observed. [35]

Nevertheless, the study of dynamics and interactions of kinesin and microtubule by single-molecule tracking techniques like fluorescence microscopy, optical microscopy, and optical tweezers is challenged by limited optical resolution and stability of the optical markers attached to biomolecules. [36] Visualization of the dynamics in the kinesin-microtubule interaction requires both the nanometer spatial resolution and the sub-second temporal resolution. High-speed atomic force microscopy (HS-AFM) offers the direct visualization of single kinesin in action at enough high spatio-temporal resolutions. [37–39] However, the direct imaging of single moving kinesin along deformed microtubules is not available yet. [40] In this chapter, I, therefore, explore the kinesin motility along the bent microtubules by the HS-AFM and observe the direct effect of the deformation on the kinesin-microtubule interaction. This chapter is one of the initial efforts to use HS-AFM for a rather straightforward approach to visualize kinesin along the microtubule. [40] The direct relation between the curvature formed in the bent microtubule and the motility behavior of kinesins is established.

3.2. Results and Discussion

3.2.1. Experimental design for observation of microtubule immobilized on mica supported lipid bilayer in HS AFM

Using the HS-AFM, the movement of single kinesins along the microtubules were monitored. For this, the microtubules were immobilized on a mica supported lipid bilayer. The preparation of the mica supported lipid bilayer was done using the vesicle fusion method [41]. First, an electrically neutral phospholipid, 1,2-dipalmitoyl-sn-glycero-3-phosphocholine (DPPC), and a positively charged phospholipid, 1,2-dipalmitoyl-3-trimethylammonium-propane (DPTAP), were mixed at desired gravimetric ratios. The small unilamellar lipid vesicles were directly deposited on freshly cleaved mica surface on the circular sample stage of the AFM microscope.

It was observed that uniform and planar lipid bilayers could be obtained for 0.50 mg/mL with the weight ratio of DPPC: DPTAP = 7:3 (Figure 3.1 A). Height of lipid bilayer was ~4 nm (Figure 3.1 B).

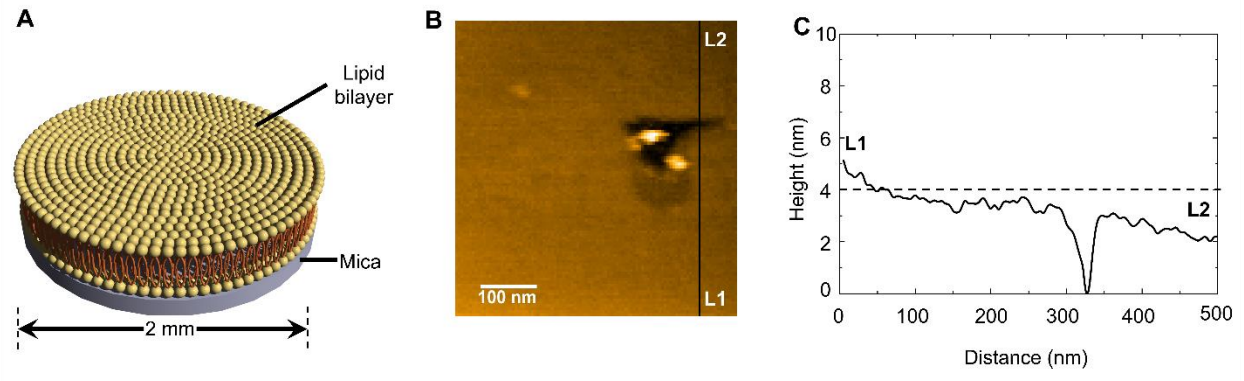

Figure 3.1. *Substrate for immobilization of the microtubules.* (A) Schematic illustration showing homogenous planar lipid bilayer formation on mica. (B) HS-AFM image of the homogenous lipid bilayer on mica. Scan area: 500×500 nm^2. A crack was created on the lipid bilayer by the cantilever. (C) Height profile of lipid bilayer from line corresponding to L1-L2 on Figure 3.1 B. Horizontal dashed line shows the average height of the lipid bilayer was ~4nm.

After the mica supported bilayer was formed, microtubule was applied and allowed to adsorb on the lipid bilayer for 10 minutes. 1.12 μM microtubule showed ~ 3 microtubules per image with area 800×800 nm^2. An AFM image of a straight microtubule immobilized on the lipid membrane is shown in Figure 3.2 A. From the height profile in Figure 3.2 B, the height of the microtubule was found to be about 25 nm, which agrees with literature. [42,43]

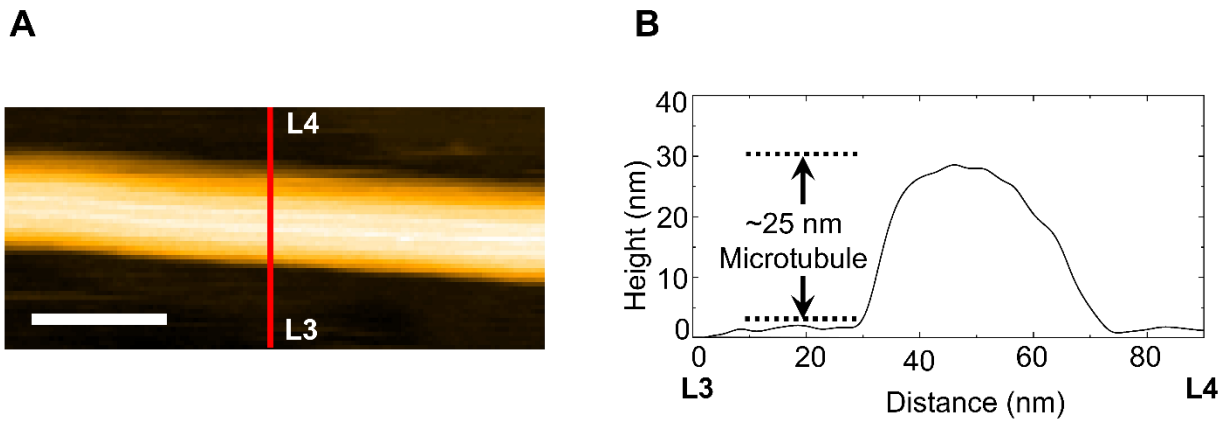

Figure 3.2. *Observation of the immobilized microtubules on the lipid bilayer.* (A) AFM image of part of a straight microtubule adsorbed on mica supported lipid bilayer. Scale bar: 50 nm. (B) Height profile of line L3-L4 indicated by the red line in (A). The height of the microtubule was found to be ~25 nm, proving the presence of 13 protofilaments in the microtubule structure.

After that, 600 nM kinesin was applied on stage and incubated for 5 minutes for ensuring binding of kinesins to the microtubules. Finally, adenosine triphosphate (ATP) was introduced in the imaging buffer to initiate kinesin movement along the microtubule. The ATP concentration used was kept considerably low, 50 µM, so that the kinesin velocity was sufficiently slow for the HS-AFM observation. [44] The expected velocity was ≤ 100 nm/s at this ATP concentration. [44]

In order to cause bending of microtubules, the lipid membrane was first, washed with Tris-HCl (pH 6.8), which caused numerous islands on the lipid surface. Then microtubules were applied on the surface and tended to bend along the boundary of the lipid bilayer islands (Figure 3.1 E). The transportation of single kinesins along the bent microtubules in the presence of 50 µM ATP was performed.

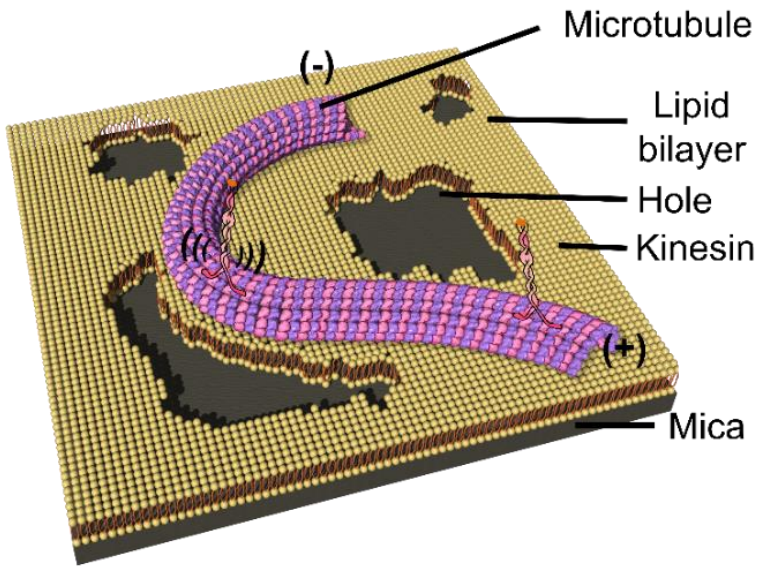

Figure 3.3. *Deformation of the immobilized microtubules.* Schematic illustration showing the bending of a microtubule by modifying the mica supported lipid bilayer substrate.

3.2.2. Effect of microtubule deformation on their interaction with kinesin

The movement of kinesins along the microtubules immobilized on mica supported lipid bilayer can be investigated from the time-lapse AFM images showing their displacements with time (Figure 3.4 A, B).

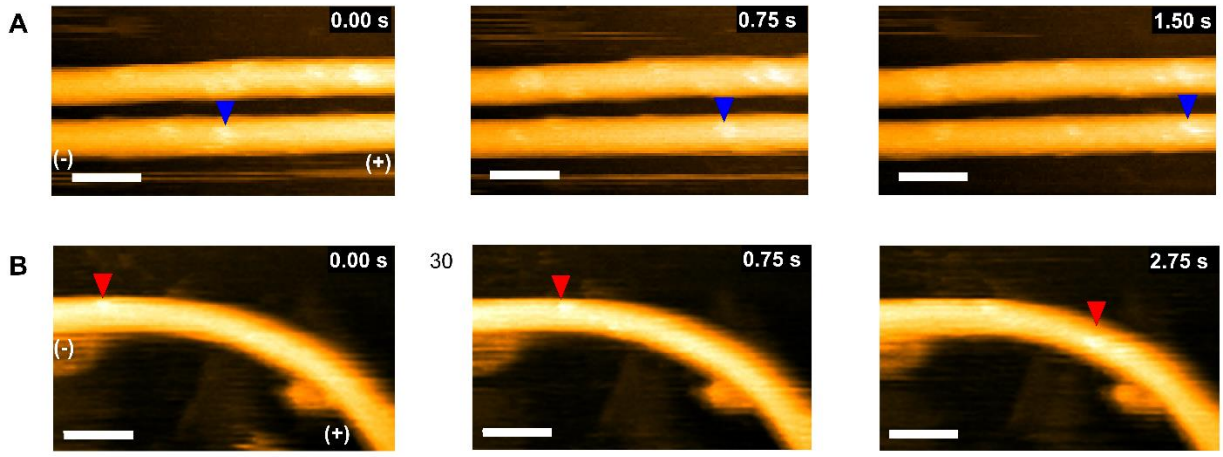

Figure 3.4. *Observation of kinesin motility along the microtubules.* (A) Time-lapse HS- AFM images showing motility of a single kinesin along the straight microtubule. The single kinesin moving along the microtubule is indicated using the blue arrowheads. (Plus and minus ends of the microtubule are shown in the first image of the series.) Scale bar: 50 nm. (B) Time-lapse HS-AFM images showing motility of a single kinesin along the bent microtubule. The positions of one

kinesin along the microtubule are shown using the red arrowheads. (Plus and minus ends of the microtubule are shown in the first image of the series.) Scale bar: 50 nm.

The time-displacement profiles are given in Figure 3.5, which show that the movement of the kinesins along the bent microtubule is accompanied by several pausing events which were not observed for the case of the straight microtubules.

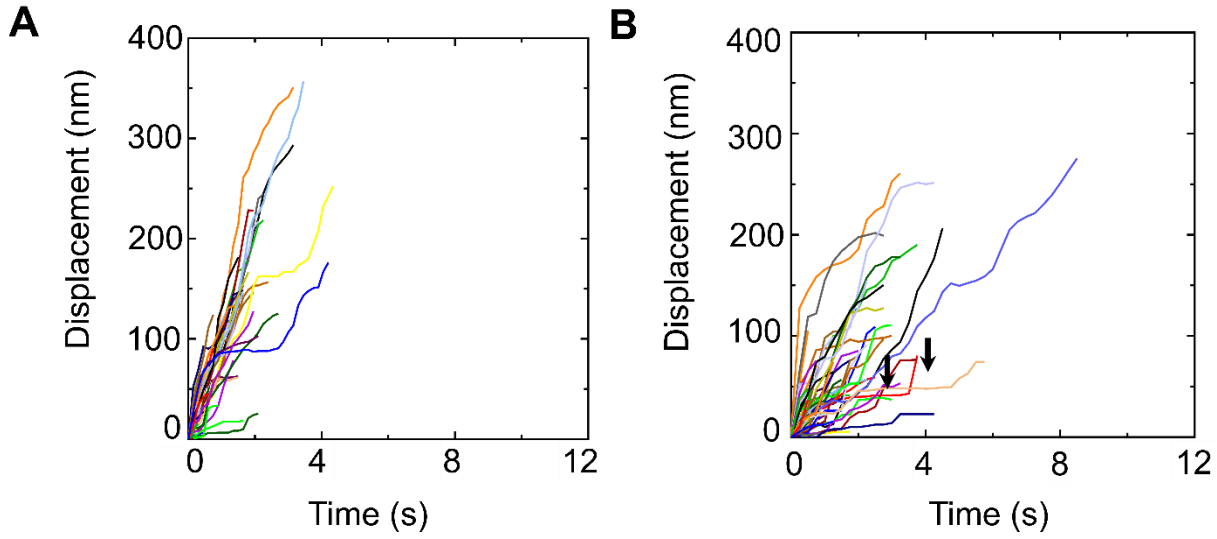

Figure 3.5. *Time-displacement plot of kinesins moving along the microtubules.* Displacement of kinesins with time along (A) the straight and (B) the bent microtubules. Analysis of kinesins traveling along one straight microtubule and one bent microtubule are included in this plot. The number of kinesin molecules traced for the analysis is 57 for both the cases. Increased number of pauses could be noticed while kinesins are traveling along the deformed microtubule. Positions of some representative pausing events are shown using vertical black arrows.

The pauses might have contributed to slowing down the kinesin movement along the bent microtubules. It is evident that along the straight microtubule kinesins' displacements were longer than along the bent microtubule. The time-displacement relation is characterized by the velocity. Therefore, I have calculated the velocity of the kinesins to reveal if the bending of microtubule has an effect on the velocities of the kinesins. To determine the velocity, I have considered the displacements made by the kinesins in every two consecutive frames and obtained the instantaneous velocities by dividing the displacements with frame interval (150 ms for the straight microtubule and 250 ms for the bent microtubule). The frequencies of the velocities were distributed as shown in Figure 3.6.

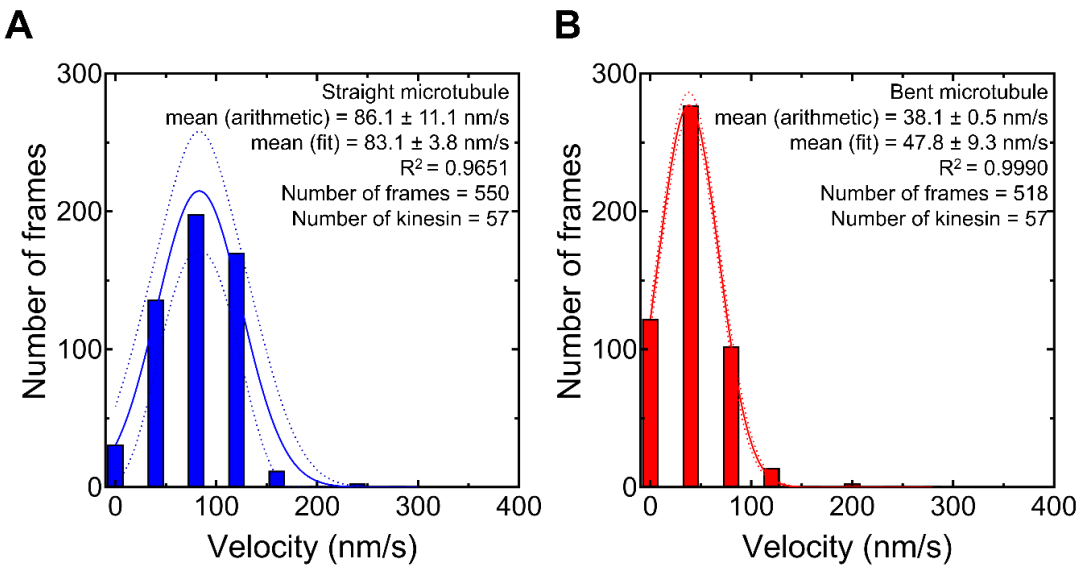

Figure 3.6. *Velocity distribution of kinesins moving along the microtubules.* Distribution of the velocities of the kinesins along the straight (A) and the bent (B) microtubule. Bin size = 40 nm/s. The distributions were fitted to the Gaussian equation. Solid lines represent the fitted lines and the dotted lines show the deviation from fitting. Fitting information, the number of data analyzed and mean velocities obtained arithmetically and from the fit are provided in the figure legends.

From Figure 3.6, it can be seen that the frequency distribution of the velocities of kinesins are normally distributed and can be fitted to the Gaussian distribution. The mean velocity of the kinesins moving along straight microtubule obtained from the Gaussian fit was 83.1 ± 3.8 nm/s (mean ± SD, n= 57) (Figure 3.6). This value corresponds to the velocity of gliding microtubules on kinesin in a similar observation system. [45] But the velocity of kinesins moving along the bent microtubules was observed to be statistically significantly lower, 47.8 ± 9.3 nm/s (mean ± SD, n= 57). As the data shown in Figure 3.6 were normally distributed, Student's t-test was carried out to check the statistical significance of the difference in the velocities of the kinesins moving along the straight and the bent microtubule (Figure 3.7, t-test, $P<0.0001$).

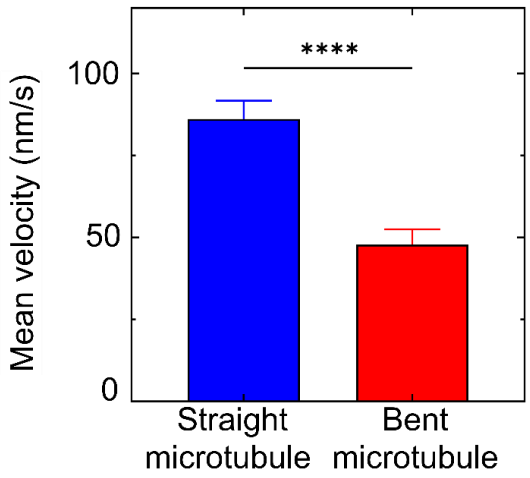

Figure 3.7. *Mean velocities of the moving kinesins along the microtubules.* Mean velocity of the kinesins moving along straight and bent microtubules. The results from the t-test showed that velocity values were statistically significantly different at P <0.0001. ****P<0.0001.

I also analyzed the distances traveled by kinesins along the microtubules. In order to determine the mean distance, bin-independent cumulative probability distributions of the distances were plotted (Figure 3.8). The distributions were fitted to the function: $y = e^{\frac{x_0 - x}{t}}$; where x_0 is the shortest distance traveled measured during analysis. The only fit parameter, the decay constant, *t*, gave the mean distance traveled in the distribution.

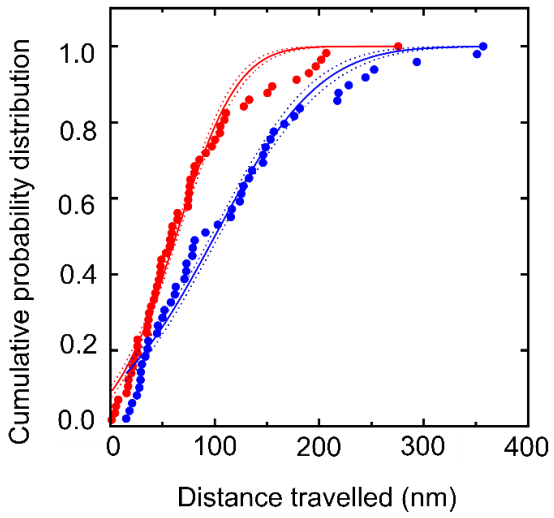

Figure 3.8. *Distance traveled by the kinesins along the microtubules.* The cumulative probability distribution of distance traveled by kinesins along straight (blue) and bent (red)

microtubules. The cumulative probability functions were fitted to $F(x) = z * dist(z)$; where, z = $(\frac{\text{x-mean}}{SD})$ and SD = x_{max}-x_{min}. The number of kinesin molecules considered for straight microtubule =57 and for bent = 57. Mean distance traveled by kinesin along straight and bent microtubules were 100.1 ± 1.8 and 62.8 ± 0.9 nm from fitting with R^2 = 0.9732 and 0.9785, respectively. The data were normally distributed checked by Kolmogorov-Smirnov test for normality test at alpha = 0.001. t-test gave P<0.001, showing that the mean distances traveled by kinesins along straight and bent microtubules were significantly different.

It was found that, the mean distance traveled by kinesins along straight microtubule was about 100 nm (n=57), statistically significantly higher than that along the bent microtubules which was about 60 nm (n=57) (Figure 3.8, Student's t-test for statistical significance test showed the results were different from each other at P<0.001).

Such observations suggest that the deformation of microtubule might have affected the kinesin-microtubule interaction. The highly processive kinesin is reported to travel about 1 µm at saturating ATP concentration in *vitro* environment. [46] The low distance traveled by the kinesin in the present observation might be due to low ATP concentration used. [44]

3.2.3. Effect of bending of the microtubule on single kinesin moving velocity

I extended the analysis to establish a correlation of kinesin motility with the bending curvature in the bent microtubule. Curvature of an arc is a measure of how much the curve deviates from a straight line. Therefore, it can be a suitable approach to quantify the extent of bending in microtubules. In this analysis, I considered the bent microtubule as a series of several curved segments. The curvature of each segment was determined using a custom MATLAB program (details in the experimental procedures). The maximum and minimum values of curvatures obtained were 2.5×10^{-4} nm^{-1} and 1.6×10^{-2} nm^{-1}.

Figure 3.9 A shows how the radius of curvature of a bent microtubule segment is defined.

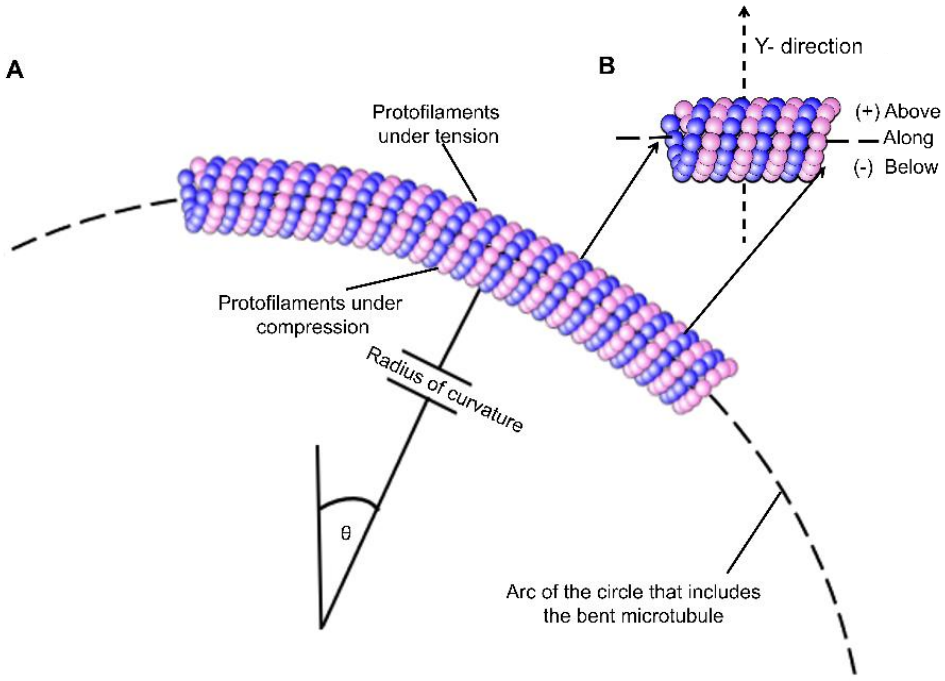

Figure 3.9. *Determination of radius of curvature of a bent microtubule.* (A)Schematic illustration showing the radius of curvature of a segment of the bent microtubule. The bent region above the neutral axis of the microtubule is apparently under tensile stress while that below the neutral axis is compressed. (B) The three horizontal sections showing the region above along and below the neutral axis of the microtubule.

For the ease of discussion, the curvatures of the bent microtubule segments were divided into three ranges: low curvature for 0-0.001 nm^{-1}, intermediate curvature for 0.001-0.01 nm^{-1} and high curvature for 0.01-0.1 nm^{-1}. Figure 3.10 shows the abovementioned three curvature ranges on the plot of the neutral axis of a bent microtubule.

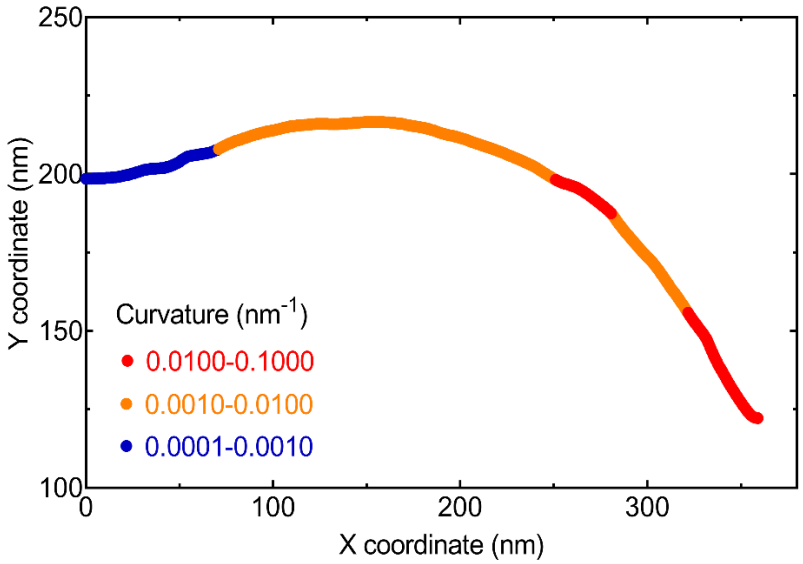

Figure 3.10. *Color-coded curvature ranges of the bent microtubule.* The low intermediate and high curvature regions are represented by the blue, orange and red colors on the plot, respectively.

Next, I plotted the velocities obtained in the low, intermediate and high curvature ranges in histograms (Figure 3.11 A-C). At low curvature range, it showed the typical normal distribution of the velocities with a mean of about 100 nm/s. In the intermediate range, the mean shifted to lower velocity which decreased more at high curvature range.

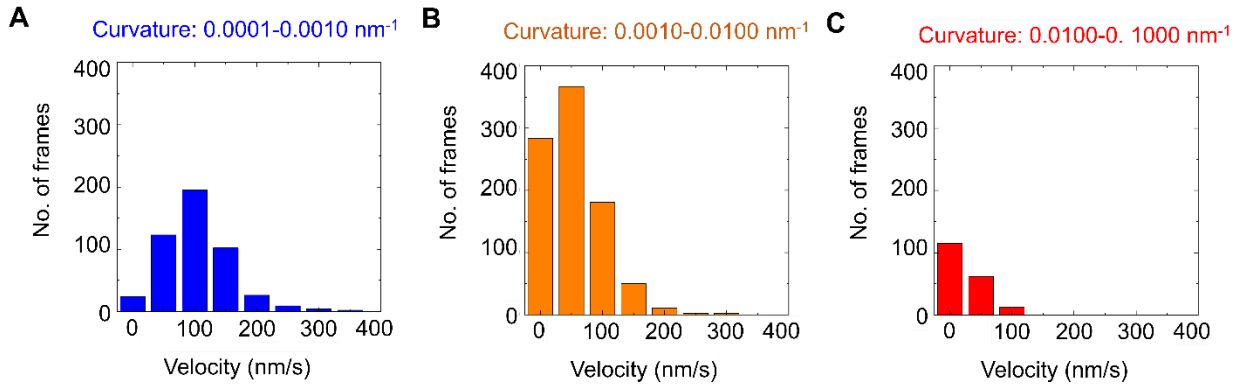

Figure 3.11. *Velocity distribution of kinesin movement along the bent microtubule.* The distribution of velocities in (A) low, (B) intermediate and (C) high curvature region of the bent microtubule shown in Figure 3.10.

Next, the curvatures were binned into bins of 0.001 nm^{-1} widths. The mean velocities of the dynein-driven Qdots along segments having curvatures in each bin were determined and then plotted against their curvature (Figure 3.12).

To get the correlation between the extent of bending of microtubule and kinesin motility first I determined the velocities of kinesins in every two consecutive frames in all the segments. The velocities were then plotted against their corresponding bins of the segment curvatures. The mean of velocities in each bin were also determined (Figure 3.11). It was found that the mean velocities obtained from this analysis could be expressed as a function of the curvature. The velocity of the kinesin appeared to decrease exponentially with an increase in the curvature of microtubule with a power of - 0.3.

The fitting equation in this case was: $y = mx^n$ … … … (1)

where, fitting parameters, m = 8.4 ± 2.5, and n = -0.3 ± 0.1.

The logarithmic plot of the graph in Figure 3.12 is given in the inset.

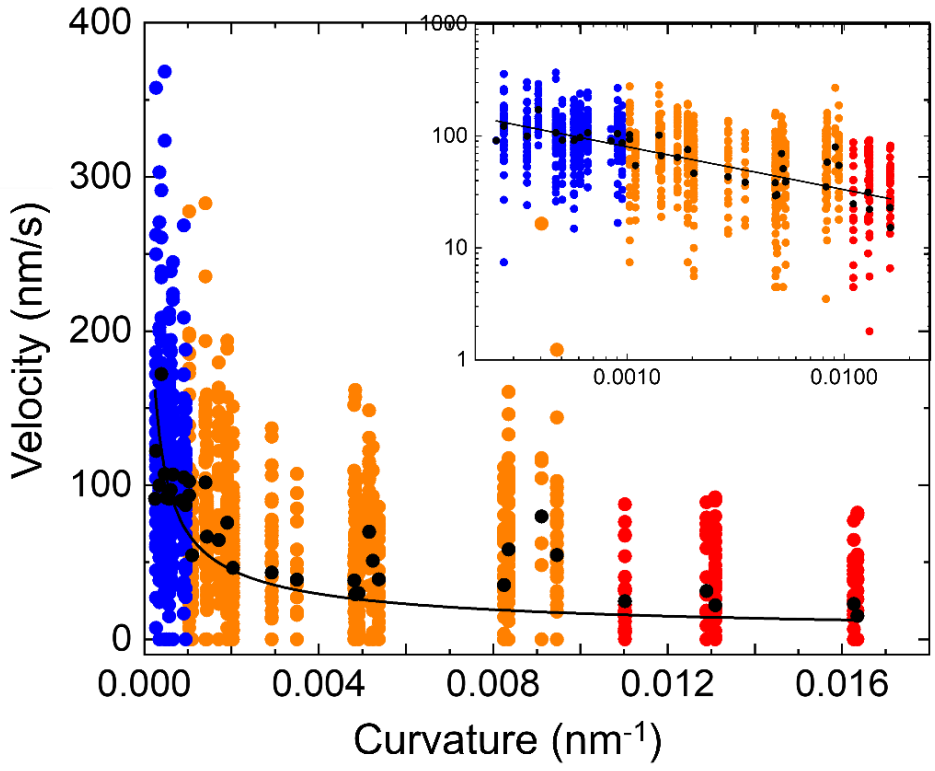

Figure 3.12. *Curvature dependent velocity distribution of kinesin along the bent microtubule.* Fit equation: $y = mx^n$. m = 8.4 ± 2.5, and n = -0.3 ± 0.1. The number of kinesins considered = 37. The total number of frames = 1568. Logarithmic plot of the graph is given in the inset. Blue,

orange and red colors are used to identify the low, intermediate and high curvature ranges. Average velocities at each bin are shown using black closed circles.

The bent microtubule has a convex (outer) side and a concave (inner) side, separated by a central or the neutral line. The outer side is stretched while the inner side is compressed. (Figure 3.9). The extent of compression or elongation of the microtubules' protofilaments depends on the extent of curvature of the microtubule. To analyze the effect of microtubule bending to kinesin motility in more detail, the bent microtubule under study was divided into three sections along the microtubules' neutral axis (Figure 3.9); the region around the neutral axis, the outer tensile region, and the inner compression region. Therefore, I analyzed the velocities of kinesin movement by considering the aforementioned three sections named along, above and below the horizontal axis of the microtubules, respectively (Figure 3.13). The mean velocities significantly differed for the straight and the bent microtubules, but along the same microtubule, the velocities remained unaltered along the three horizontal sections. This observation, together with the fact that kinesin walks along single protofilament, [47,48] infer that the bending deformation of the microtubule in the present experimental conditions may lie in the "elastic" region where only the inter-protofilament bonds are disrupted. [35,49]

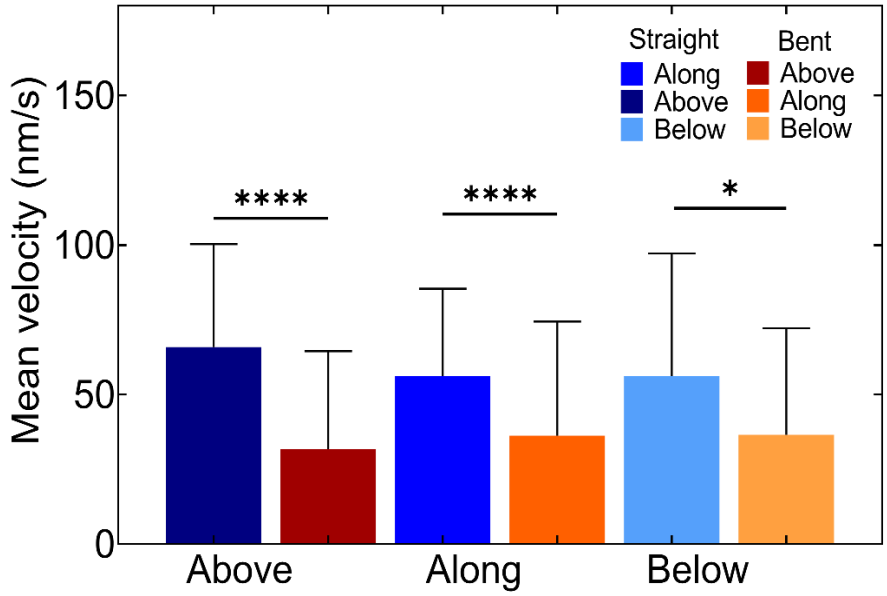

Figure 3.13. *Mean velocities of kinesins along three axial sections of the straight and the bent microtubules*. The coordinates of the central axis of the microtubules were determined. The shortest distance of the kinesin coordinate from the central axis was calculated with direction: (+) for above and (–) for below the central axis. Three axial sections above, along and below the microtubule neutral axis in the bent microtubules are the above-mentioned regions under

tensile stress, neutral state and under compressive stresses, respectively. The number of frames considered: 119, 162 and 59 for the straight and 130, 413 and 100 for the bent microtubule in three sections above, along and below the neutral axis, respectively. Error bars: standard deviation. The velocities of kinesin motility along the straight and the bent microtubules were found to be statistically significantly different (ANOVA, Tukey's multiple comparison test, ****P<0.0001 and *P<0.05). But for the same microtubule, the velocities did not significantly change above, along or below the neutral axis of the microtubule.

The decrease in the kinesin velocity has been interpreted previously due to disruption of longitudinal inter-dimer bonds along protofilaments, [50] loss of parts of the protofilaments, [50,51] and the resulting polar mismatching. [52] However, the HS-AFM in this study is capable to visualize any lattice defects occurring at the microtubule structure (Figure 3.14 A).

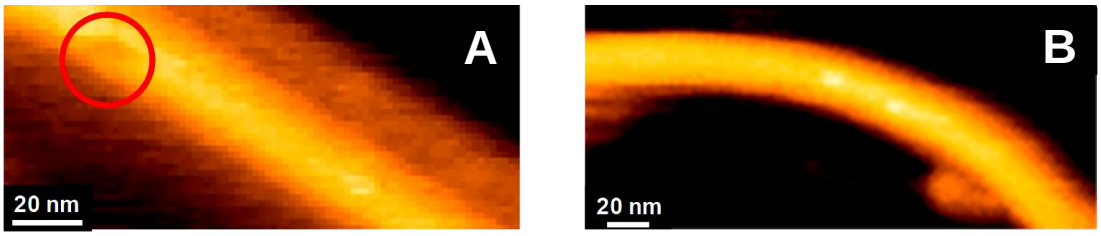

Figure 3.14. *Observation of microtubule lattice defect using the HS-AFM.* High-speed AFM image of a microtubule with defects (A). The site of the defect is marked with the red circle. For comparison, the bent microtubule under study is provided in (B).

The bent microtubule under the present study is confirmed to possess no lattice defects. Therefore, the effect on the kinesin motility caused by the bending of microtubule may not be the outcome of lattice defect only. Even the positions of the tubulin proteins on the bent microtubules may possess effect to modulate their interaction with the kinesins.

3.2.4. Kinesin's bias to deformed protofilaments of microtubule

By plotting the numbers of the traces by the kinesins in the three regions of the straight and the bent microtubules namely, above, along and below the central or the neutral line, any preference for the kinesins to bind to the three regions as mentioned could not be found (Figure 3.15).

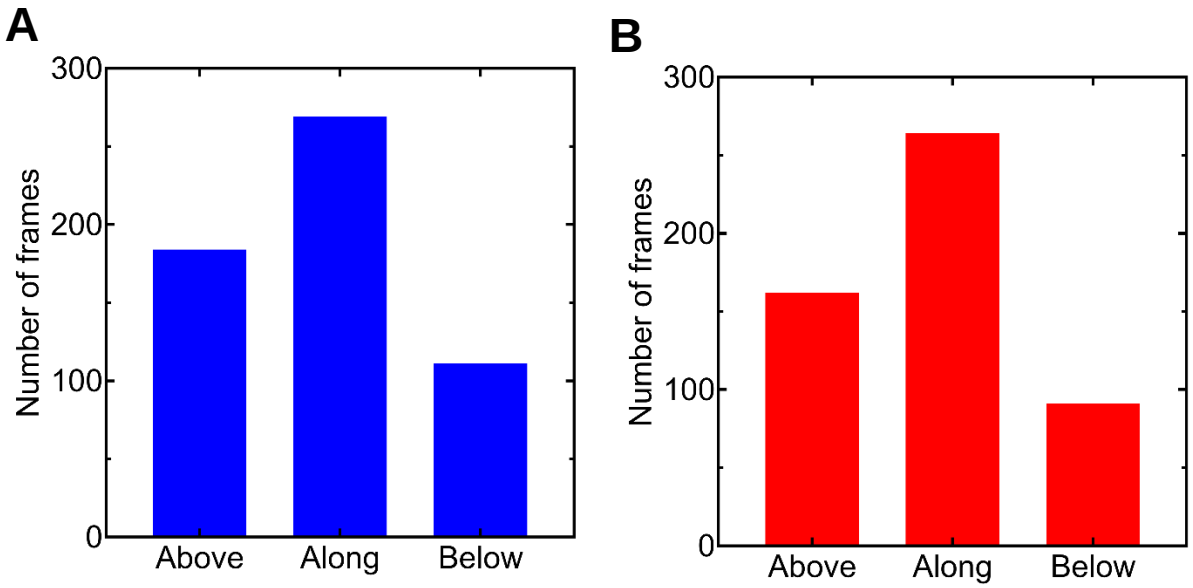

Figure 3.15. *Kinesins' bias to the microtubules.* Preference of kinesins to the section relative to the neutral axis of the (A) straight and the (B) bent microtubule. Three sections were chosen, which are: the region around the neutral axis (named "along"), the outer tensile region (named "above"), and the inner compression region (named "below"). No difference in the distribution of the number of kinesin stepping along the three region could be found along the straight and the bent microtubules. The number of kinesins considered for both (A) and (B) is 57 with the total number of frames 551 and 519, respectively.

The high spatial resolution of the HS-AFM may provide information on the kinesin's movement along the microtubule protofilaments. Using the kinesin coordinates, I measured the shortest distance of every point from the central axis. These distances are displayed in the histograms in Figure 3.16. Each bin is sized to 1 unit from -30 to 30. Positive distance represents distances above the central axis and negative distances are below the central axis.

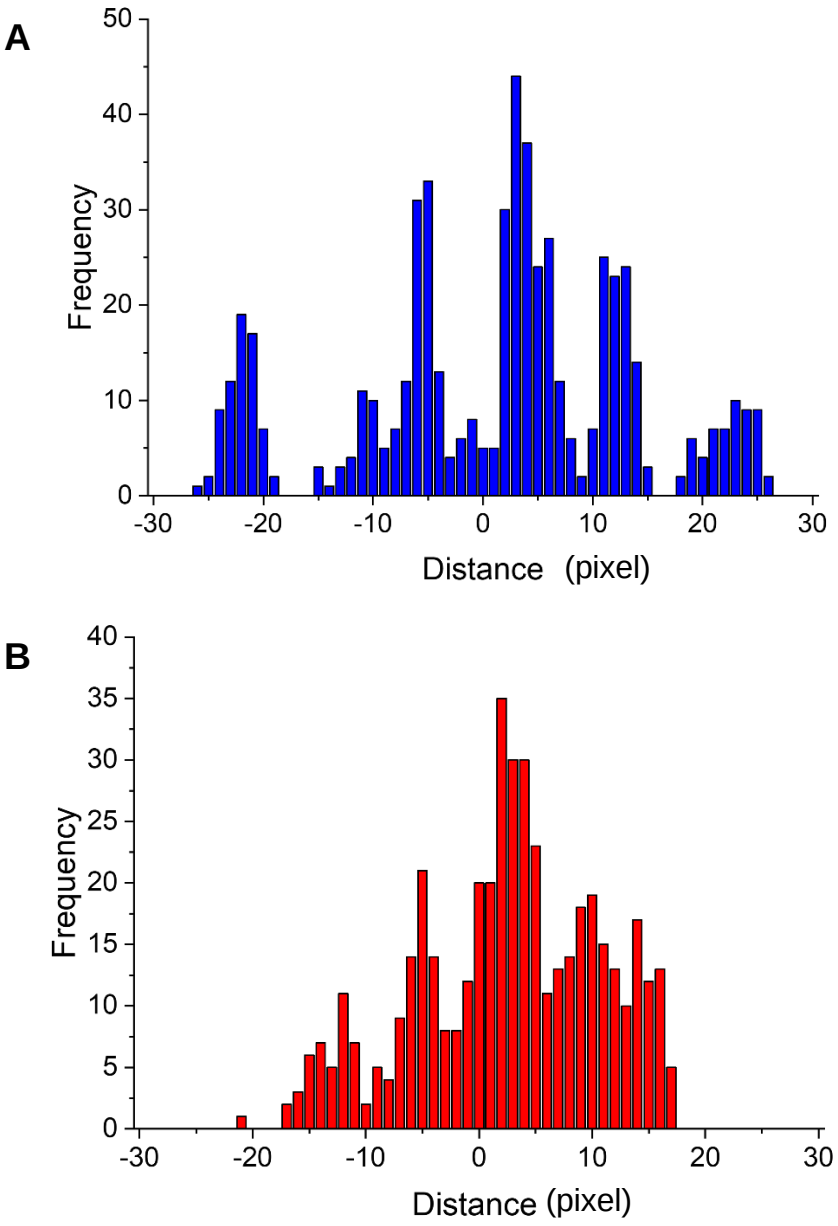

Figure 3.16. *Traces of the kinesins on the microtubule*. The histograms showing the distribution of the kinesin traces with reference to the central axis of the straight (A) and the bent (B) microtubules. Positive distance represents distances above the central axis and negative distances are below the central axis. For the bent microtubule, the region above and below the central axis represents the sides under compressive stress and tensile stress, respectively.

The prominent peaks positioned almost equally spaced refer to the protofilaments of the microtubule. While the protofilaments are distinctly visible in the case of the straight microtubule, for the bent microtubules the protofilaments seem to appear rather closely spaced.

3.2.5. Effect of bending of the microtubules on the kinetic parameters of kinesin-microtubule binding

The bending of the microtubule structure may bestow the effect on their binding interaction with kinesin. Therefore, next, I explored the binding affinity of kinesin to microtubule by analyzing of kinesins on the straight and the bent microtubules. For this, I evaluated three kinetic parameters, binding rate constant k_{on}, dissociation rate constant k_{off} and dissociation constant K_d (Table 3.1). The k_{on} was defined as the number of kinesins bound on the microtubule in a unit of kinesin concentration, microtubule length and time ($M^{-1}\mu m^{-1}s^{-1}$), by the previously reported [53,54] (details in methods). The measured k_{on} values show that, k_{on} of kinesins on the bent microtubule $k_{on}^{bent} = 3.6 \times 10^6 \pm 5.2 \times 10^4$ $M^{-1}\mu m^{-1}s^{-1}$ was ~2 times higher than that on straight microtubule ($k_{on}^{straight} = 1.5 \times 10^6 \pm 2.6 \times 10^3$ $M^{-1}\mu m^{-1}s^{-1}$). Higher k_{on} value refers to the faster binding of kinesins to the tubulins in the bent microtubule compared to those in the straight microtubule.

On the other hand, the dissociation rate constant k_{off} was characterized as the inverse of the kinesins' binding time on the microtubules. In order to obtain the binding time, the cumulative probability functions of the binding time of each kinesin were determined for the straight and the bent microtubules (Figure 3.17). The mean binding time of kinesins on the straight microtubule was about 1.5 s (n = 57) and that on the bent microtubule was about 2.2 s (n = 57). Therefore, kinesins, having spent significantly longer time on the bent microtubule than on straight microtubule gave slower dissociation rate constant, $k_{off}^{bent} = 0.45 \pm 0.02$ s^{-1} while detaching from the bent microtubule than from the straight microtubule ($k_{off}^{straight} = 0.67 \pm 0.04$ s^{-1}).

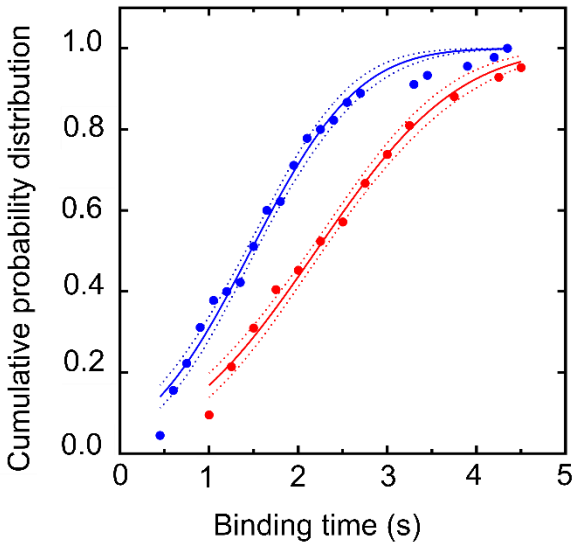

Figure 3.17. *Kinesin binding time on the microtubules.* The cumulative probability distribution of kinesin binding time on the straight (blue) and the bent (red) microtubules. The binding time is defined as the total time kinesin stays attached to the microtubule during movement. The time was limited by either the detachment of kinesin from microtubule or the end the of observation. The cumulative probability functions were fitted to F(x)=z∗dist(z); where, z = ((x-mean)/SD) and SD = (x_{max}-x_{min}). The mean binding times of kinesin on the straight and the bent microtubules are 1.5 ± 0.1 s (n=57) and 2.2 ± 0.1 s (n=57) from fitting with R^2 = 0.9857 and 0.9895, respectively. The data sets did not pass the tests for normality (at alpha = 0.01) hence were tested for statistical analysis using the non-parametric Mann-Whitney test. The results varied significantly at P<0.01.

It is to note that the binding time of kinesin is affected due to mechanical forces between the kinesin and its receptor microtubule. [55] Next, I calculated K_d (= $\frac{k_{off}}{k_{on}}$) for characterizing bindingthe of kinesin to the straight and the bent microtubules. The K_d values reflected high kinesin binding affinity of the bent microtubule than the straight microtubule. This strong binding might have taken place due to stronger intermolecular forces between the kinesin and tubulin of the bent microtubule. Such speculation stands out considering five-fold stronger affinity of a kinesin-like protein, Kip3, for curved tubulin than that for straight ones significantly lowered the ATP hydrolysis. [56]

Table 3.1. Summary of the kinetic parameters k_{on}, k_{off} and K_d of kinesin binding to the straight and the bent microtubules.

Microtubule type	k_{on} ($M^{-1}\mu m^{-1}s^{-1}$)	k_{off} (s^{-1})	K_d (M.μm)
Straight	$1.5\times10^{6} \pm 2.6\times10^{3}$	0.67 ± 0.04	$4.5\times10^{-7} \pm 3.0\times10^{-8}$
Bent	$3.6\times10^{6} \pm 5.2\times10^{4}$	0.45 ± 0.02	$1.3\times10^{-7} \pm 6.0\times10^{-9}$

Recent observation claims binding of high concentration kinesin may give rise to 1.6% axial expansion of the microtubule. [57] Converse to this results from the present study lead to conclude the following points: the deformation in the microtubule lattice by bending, may impose an effect on the kinesin-microtubule interaction. No apparent lattice defects on the bent microtubule could be observed. The bending of the microtubule may cause the constituting tubulins to undergo alteration in their native configurations and bring changes to the electronic charge distribution on the microtubule surface. Since the binding of kinesin to microtubule is directly related to the non-uniform charge distribution on kinesin and tubulin, [58] the present speculation is supported by recently explored evidence which shows, KLP10A, a member of the kinesin-13 family, is not catalytic when bound to the microtubule-lattice and becomes catalytic when bound to deformed tubulin. [59] The reports on stable and ordered complex formation by kinesin-13 and curved tubulin protofilaments stand in line to support the presented results showing the longer binding time and larger displacement of kinesin movement along the bent microtubule. [60–62] Post-translational modifications of tubulins, for example, acetylation is reported to distinctly impact the motor protein movement along the microtubule. [63] The obtained results provide an important clue on how an apparently small deformation, i.e., the bending of the microtubule, can alter its interaction with kinesins. How such change may enforce effect on the ATPase activity of kinesin motors opens a new window of investigation. [64,65]

3.3 Conclusion

I have been able to realize the visualization of single kinesins transporting along microtubule with high spatio-temporal resolution. Also, I could successfully establish the method to cause bending of microtubule in an *in vitro* environment. The curvature of bending was not controlled but persisted in the range where elastic deformation of microtubule takes place. [35,49] The curvature dependent motility behavior of kinesin reported here could facilitate our current understanding of cellular dynamics. The present approach allowed to quantify the binding affinities of kinesin to undeformed and deformed microtubule simply. The results show theoretically direct indication of altered interaction between kinesin and deformed microtubule. An alteration in microtubule-motor interaction by bending may provide an understanding of how microtubules serve as mechanotransducers in the cell. [8]

3.4 Experimental Procedure

3.4.1. Purification of tubulin and polymerization to microtubules

Tubulin was purified from fresh porcine brain using a high-concentration PIPES buffer (1 M piperazine-N, N′-bis(2-ethanesulfonic acid) (PIPES), 20 mM ethylene glycol-bis(β-aminoethyl ether)-N, N,N′,N′-tetraacetic acid (EGTA), 10 mM $MgCl_2$; pH adjusted to 6.8 using KOH) [66] and stored at -80 °C. The tubulin was polymerized into microtubules in presence of 4 mM guanosine-5'-triphosphate (GTP) at 37 °C for 30 min. Then, 1 mM paclitaxel was added and again incubated for 15 min at 37 °C. The paclitaxel-stabilized microtubules (tubulin concentration = 1.12 μM) were then suspended in a buffer with the composition of 80 mM PIPES (pH = 6.9), 2 mM $MgCl_2$, 1 mM EGTA, 1 mM GTP, 50 μM paclitaxel, and 2.74 M glycerol (20 vol%).

3.4.2. Expression and purification of kinesin

Kinesin-1 construct consisting of human kinesin (residues 1-465), an N-terminal histidine tag, and a C-terminal Avi-tag was purified. The expression and purification of kinesin were performed as done previously. [67]

3.4.3. Preparation of mica supported lipid bilayer

Lipid bilayers were prepared using lipids 1,2-dipalmitoyl-sn-glycero-3-phosphocholine (DPPC) and 1,2-dipalmitoyl-3-trimethylammonium-propane (DPTAP) (Avanti Polar Lipids, Alabaster, AL). A previously published method for the preparation of lipid bilayers was followed and is outlined here. [41] Solutions of DPPC and DPTAP in chloroform were mixed at a gravimetric ratio of 3:7. The chloroform was then evaporated under a stream of nitrogen gas. Then, Milli-Q H_2O was added to obtain a 0.5 mg/mL lipid solution. Freshly cleaved mica was placed on a circular sample stage of diameter 2 mm. A 0.5 mg/mL lipid solution was added on the mica and incubated for 10 min. The sample stage was then washed thoroughly with imaging buffer (80 mM PIPES (pH 6.9 with KOH), 2 mM $MgCl_2$, and 1 mM EGTA in Milli-Q water). A uniform lipid bilayer on mica substrate was obtained. For observing bent microtubules, 20 mM Tris-HCl (pH adjusted to 8.8 with KOH) was applied on the sample stage, incubated for 3 seconds and washed with the imaging buffer. As a result, cracks were created on the lipid bilayer and discrete islands of the lipid bilayer were formed.

3.4.4. Single kinesin transportation assay along microtubule

2.00 µL of 1.12 µM paclitaxel-stabilized microtubule solution was placed on the mica supported lipid bilayer (with or without Tris-HCl washing) and left to adsorb on the surface for 10 min. After that, the sample stage was thoroughly washed with 20.0 µL to 40.0 µL of imaging buffer. Next a solution of Avi-tag kinesin (600 nM) diluted in buffer composed of 80 mM PIPES, 40 mM NaCl, 1mM EGTA, 1 mM $MgCl_2$, 20 µM casein, 1 mM dithiothreitol, 10 mM paclitaxel; pH 6.8) was applied and allowed to stand for 5 minutes. For observation of the single kinesins moving along the microtubules, a mixture of kinesin and ATP solution was added along with the imaging buffer. The final concentrations of kinesin and ATP while imaging were 40 nM and 5 µM, respectively. All experiments were carried out at room temperature.

3.4.5. Imaging with High-Speed AFM apparatus

The measurements were performed using a laboratory-built high-speed AFM. [53] The topography images were recorded in tapping mode. BL-AC10DS-A2 (Olympus, Tokyo, Japan) cantilevers were used. These cantilevers were about 9 µm long, 2 µm wide and 130 nm thick with a spring constant between 0.01 Nm^{-1} and 0.1 Nm^{-1}, according to the supplier. All images were recorded in the above-specified imaging buffer, where the cantilevers' resonance frequencies were between 400 kHz and 500 kHz. The free oscillation amplitude of the cantilever was set to about 1.5 nm, with a set-point of approximately 80% of the free amplitude during scanning. The carbon tip at the end of the cantilever was grown using electron beam deposition and sharpened using a plasma etcher to a tip radius between 2 nm and 5 nm. The imaging rate was set to 150 and 250 ms per frame for capturing movies with straight and bent microtubules, respectively. The images were analyzed using laboratory-made analysis software and Fiji. [68]

Figure 3.18 shows the arrangement of the apparatus in HS-AFM for the present investigation

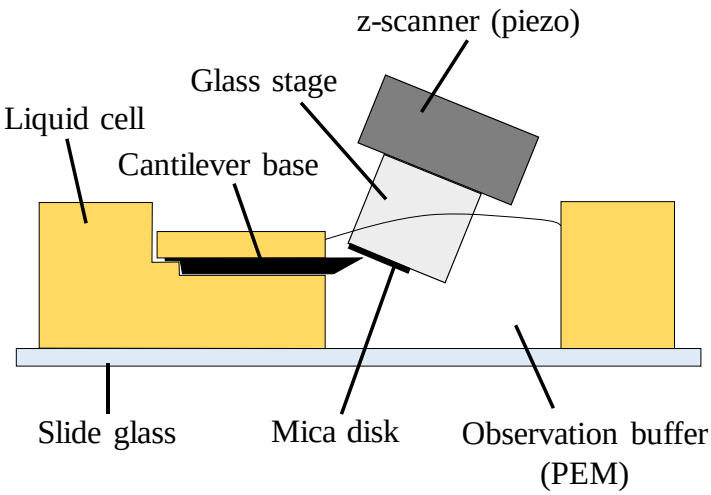

Figure 3.18. Experimental arrangement for observation in HS-AFM.

3.4.6. Estimation of parameters

The mean distance traveled were calculated by fitting the cumulative probability distribution of the distances in the equation: *Y= z*dist(z), where, z* $= \frac{x-mean}{SD}$ *and SD = (*x_{max}-x_{min}*)*. The data were normally distributed as checked from the Kolmogorov-Smirnov test for normality (alpha = 0.001). For this analysis, the coordinates of equally spaced points on the centerline of the buckled microtubules were divided into several sections. A custom-written MATLAB code fitted the coordinates to a half circle and obtained the coordinate of the circle and the radius of the curvature. Curvature was obtained by inverting the radius of curvature, since, curvature $= \frac{1}{radius\ of\ curvature}$. The pausing events by kinesins denoted in Figure 3.5 B, to take place if the kinesin is observed to remain stationary for at least 4 consecutive frames. The values of k_{on} on straight or bent microtubules were calculated as the number of bound kinesins normalized by kinesin concentration, length of microtubule, and observation time. Binding events were counted for 81.45 s and 53.50 s, respectively for straight and bent microtubules, respectively. The lengths of the microtubules were measured from the HS-AFM images using software, Fiji. k_{off} was calculated as the reciprocal of mean binding time. The binding time was defined by the duration of time starting from attachment of the kinesins to microtubule until they were detached from microtubule, or the imaging was finished. To determine mean binding times bin-independent cumulative probability distributions of the binding times were plotted. The distributions were

fitted to the function: $y = e^{\frac{x_0 - x}{t}}$; where, x_0 is the shortest binding time measured during analysis. The only fit parameter, the decay constant, *t*, gave the mean binding time in the distribution in Figure 3.7.

3.4.7. Statistical analysis

Statistical analyses were performed with GraphPad Prism 8.1.0 (www.graphpad.com). A two-tailed Student's t-test was used to compare two groups. One-way ANOVA followed by Tukey's multiple comparison test was used to compare among three or more groups of normally distributed data. Kruskal-Wallis test followed by Dunn's multiple comparison test was used to compare among three or more groups of non-normal data. The values for the number of events, P-value, and name of the statistical test performed for each analysis are included in the figure legend or in the caption. Graphs were generated using either GraphPad Prism 8.1.0 or OriginPro 2019.

3.5 Results of Statistical analysis

Statistical analysis of all data mentioned in this chapter were carried out using the software GraphPad Prism 8.1.0. Below are mentioned the results of all relevant analysis in the sequence as they appear in the chapter.

Table 3.5.1. Results of test for Normal distribution of the mean velocities of kinesins moving along straight and bent microtubules. Following are the results from tests that were carried out. (Figure 3.6)

Anderson-Darling test	Straight	Bent
A2*	0.5707	1.889
P value	0.1323	<0.0001
Passed normality test (alpha=0.01)?	Yes	No
P value summary	ns	****
D'Agostino & Pearson test		
K2	11.53	42.01
P value	0.0031	<0.0001
Passed normality test (alpha=0.01)?	No	No
P value summary	**	****
Shapiro-Wilk test		
W	0.9498	0.8366
P value	0.0243	<0.0001
Passed normality test (alpha=0.01)?	Yes	No
P value summary	*	****
Kolmogorov-Smirnov test		
KS distance	0.09195	0.1419
P value	>0.1000	0.0060
Passed normality test (alpha=0.01)?	Yes	No
P value summary	ns	**
Number of values	57	57

Table 3.5.2. Results from the statistical analysis of mean velocity data using the non-parametric Mann-Whitney test for statistical significance (Figure 3.7).

Column B	Bent microtubules
vs.	vs.
Column A	Straight microtubules
Mann Whitney test	
P value	<0.0001
Exact or approximate P-value?	Exact
P value summary	****
Significantly different (P < 0.01)?	Yes
One- or two-tailed P value?	Two-tailed
Sum of ranks in column A, B	3937, 2279
Mann-Whitney U	626
Difference between medians	
Median of column A	90.13, n=54
Median of column B	39.60, n=57
Difference: Actual	-50.53
Difference: Hodges-Lehmann	-40.16

Table 3.5.3. Results from Kolmogorov-Smirnov test for normality of distance traveled by kinesins along straight and bent microtubules (Figure 3.8).

Kolmogorov-Smirnov test	Straight	Bent
KS distance	0.1447	0.1475
P value	0.0118	0.0034
Passed normality test (alpha=0.001)?	Yes	Yes
P value summary	*	**
Number of events	57	57

Table 3.5.4. t-test results for the comparison of the mean distance traveled by kinesins along straight and bent microtubules (Figure 3.8).

Column B	Bent
vs.	vs.
Column A	Straight
Unpaired t test with Welch's correction	
P value	0.00077
P value summary	***
Significantly different (P < 0.001)?	Yes
One- or two-tailed P value?	Two-tailed
Welch-corrected t, df	t=2.731, df=83.34
How big is the difference?	
Mean of column A	115.2
Mean of column B	75.29
Difference between means (B - A) ± SEM	-39.87 ± 14.59
99% confidence interval	-78.34 to -1.392
R squared (eta squared)	0.08217
F test to compare variances	
F, DFn, Dfd	2.102, 48, 56
P value	0.00078
P value summary	***
Significantly different (P < 0.01)?	Yes
Data analyzed	
Sample size, column A	57
Sample size, column B	57

Table 3.5.5. Assignment of group number to data sets of mean velocities of the kinesins along three axial regions of the straight and bent microtubules. These groups were analyzed for the Tukey's multiple comparison test for post-hoc analysis in Table 3.5.6.

Straight			Bent		
Above	Along	Below	Above	Along	Below
1	2	3	4	5	6

Table 3.5.6. Tukey's multiple comparison test for post hoc analysis of mean velocities of the kinesins along three axial regions of the straight and bent microtubules (Figure 3.12).

Number of families				1
Number of comparisons per family				15
Alpha				0.0001
Tukey's multiple comparisons tests	Mean Diff.	99.90% CI of diff.	Summary	Adjusted P-Value
Sets 1 vs. 2	9.687	-8.335 to 27.71	ns	0.2652
Sets 1 vs. 3	9.708	-14.06 to 33.48	ns	0.5790
Sets 1 vs. 4	33.79	14.86 to 52.73	****	<0.0001
Sets 1 vs. 5	29.58	14.05 to 45.11	****	<0.0001
Sets 1 vs. 6	29.34	9.085 to 49.59	****	<0.0001
Sets 2 vs. 3	0.02063	-22.68 to 22.72	ns	>0.9999
Sets 2 vs. 4	24.11	6.529 to 41.68	****	<0.0001
Sets 2 vs. 5	19.90	6.057 to 33.73	****	<0.0001
Sets 2 vs. 6	19.65	0.6646 to 38.63	***	0.0006
Sets 3 vs. 4	24.09	0.6532 to 47.52	***	0.0006
Sets 3 vs. 5	19.87	-0.9007 to 40.65	**	0.0020
Sets 3 vs. 6	19.63	-4.878 to 44.13	*	0.0180
Sets 4 vs. 5	-4.211	-19.22 to 10.80	ns	0.8735
Sets 4 vs. 6	-4.458	-24.31 to 15.40	ns	0.9475
Sets 5 vs. 6	-0.2474	-16.88 to 16.39	ns	>0.9999

Table 3.5.7. Results of test for Normal distribution of the binding time of kinesins on straight and bent microtubules. Following are the results from tests that were carried out (Figure).

Anderson-Darling test	Straight	Bent
A2*	1.649	1.573
P value	0.0003	0.0004
Passed normality test (alpha=0.01)?	No	No
P value summary	***	***
D'Agostino & Pearson test		
K2	11.21	29.54
P value	0.0037	<0.0001
Passed normality test (alpha=0.01)?	No	No
P value summary	**	****
Shapiro-Wilk test		
W	0.8957	0.8639
P value	0.0001	<0.0001
Passed normality test (alpha=0.01)?	No	No
P value summary	***	****
Kolmogorov-Smirnov test		
KS distance	0.1377	0.1314
P value	0.0089	0.0156
Passed normality test (alpha=0.01)?	No	Yes
P value summary	**	*
Number of values	57	57

Table 3.5.8. Mann-Whitney U test to analyze the statistical significance of the difference of binding time of kinesins on the straight and the bent microtubules (Figure 3.16).

Column A	Straight
vs.	vs.
Column B	Bent
Mann Whitney test	
P value	0.0106
Exact or approximate P-value?	Exact
P-value summary	**
Significantly different (P < 0.01)?	Yes
One- or two-tailed P value?	Two-tailed
Sum of ranks in column A, B	2853, 3703
Mann-Whitney U	1200
Difference between medians	
Median of column A	1.050, n=57
Median of column B	1.750, n=57
Difference: Actual	-0.7000
Difference: Hodges-Lehmann	-0.4500
99.01% CI of difference	-1.050 to 0.05000
Exact or approximate CI?	Exact

3.6 References

1. B. Alberts, A. Johnson, J. Lewis, M. Raff, K. Roberts, P. W. *Molecular biology of cell*. (Garland Science, New York, 2008).
2. Scholey, J. M., Sharp, D. J. & Rogers, G. C. Microtubule motors in mitosis. *Nature* **407**, 41–47 (2000).
3. Cai, P. *et al.* Nanoparticles strengthen intracellular tension and retard cellular migration. *Nano Lett.* **14**, 83–88 (2014).
4. Howard, J. *Mechanics of Motor Proteins and the Cytoskeleton*. (Sinauer Associates, Inc., Sunderland, Massachusetts, 2001).
5. Kurachi, M., Hoshi, M. & Tashiro, H. Buckling of a single microtubule by optical trapping forces: direct measurement of microtubule rigidity. *Cell Motil. Cytoskeleton* **30**, 221–228 (1995).
6. Bershadsky, A. D., Balaban, N. Q. & Geiger, B. Adhesion-Dependent Cell Mechanosensitivity. *Annu. Rev. Cell Dev. Biol.* **19**, 677–695 (2003).
7. Zhang, J., Guo, W.-H. & Wang, Y.-L. Microtubules stabilize cell polarity by localizing rear signals. *Proc. Natl. Acad. Sci.* **111**, 16383–16388 (2014).
8. Wang, N., Butler, J. P. & Ingber, D. E. Mechanotransduction across the cell surface and through the cytoskeleton. *Science* **260**, 1124–1127 (1993).
9. Stamenović, D., Mijailovich, S. M., Tolić-Nørrelykke, I. M., Chen, J. & Wang, N. Cell prestress. II. Contribution of microtubules. *Am. J. Physiol. Physiol.* **282**, C617–C624 (2013).
10. Vale, R. D. The molecular motor toolbox for intracellular transport. *Cell* **112**, 467–480 (2003).
11. Ross, J. L., Ali, M. Y. & Warshaw, D. M. Cargo transport: molecular motors navigate a complex cytoskeleton. *Curr. Opin. Cell Biol.* **20**, 41–47 (2008).
12. Odde, D. J., Ma, L., Briggs, A. H., DeMarco, A. & Kirschner, M. W. Microtubule bending and breaking in living fibroblast cells. *J. Cell Sci.* **112**, 3283–3288 (1999).
13. Dogterom, M., Kerssemakers, J. W. J., Romet-Lemonne, G. & Janson, M. E. Force generation by dynamic microtubules. *Curr. Opin. Cell Biol.* **17**, 67–74 (2005).
14. Wang, N. *et al.* Mechanical behavior in living cells consistent with the tensegrity model. *Proc. Natl. Acad. Sci.* **98**, 7765–7770 (2001).

15. Brangwynne, C. P. *et al.* Microtubules can bear enhanced compressive loads in living cells because of lateral reinforcement. *J. Cell Biol.* **173**, 733–741 (2006).
16. Brangwynne, C. P., MacKintosh, F. C. & Weitz, D. A. Force fluctuations and polymerization dynamics of intracellular microtubules. *Proc. Natl. Acad. Sci.* **104**, 16128–16133 (2007).
17. Steinberg, G., Wedlich-Söldner, R., Brill, M. & Schulz, I. Microtubules in the fungal pathogen Ustilago maydis are highly dynamic and determine cell polarity. *J. Cell Sci.* **114**, 609–22 (2001).
18. Straube, A., Hause, G., Fink, G. & Steinberg, G. Conventional kinesin mediates microtubule–microtubule interactions in vivo. *Mol. Biol. Cell* **17**, 907–916 (2006).
19. Bicek, A. D. *et al.* Anterograde microtubule transport drives microtubule bending in LLC-PK1 epithelial cells. *Mol. Biol. Cell* **20**, 2943–2953 (2009).
20. Wu, J. *et al.* Effects of dynein on microtubule mechanics and centrosome positioning. *Mol. Biol. Cell* **22**, 4834–4841 (2011).
21. Weisshaar, B., Doll, T. & Matus, A. Reorganisation of the microtubular cytoskeleton by embryonic microtubule-associated protein 2 (MAP2c). *Development* **1161**, 1151–1161 (1992).
22. Waterman-Storer, C. M. & Salmon, E. D. Actomyosin-based retrograde flow of microtubules in the lamella of migrating epithelial cells influences microtubule dynamic instability and turnover and is associated with microtubule breakage and treadmilling. *J. Cell Biol.* **139**, 417–434 (1997).
23. Stichel, C. C. & Müller, H. W. Experimental strategies to promote axonal regeneration after traumatic central nervous system injury. *Prog. Neurobiol.* **56**, 119–148 (1998).
24. Hubbard, R. D., Quinn, K. P., Martinez, J. J. & Winkelstein, B. A. The role of graded nerve root compression on axonal damage, neuropeptide changes, and pain-related behaviors. *Stapp Car Crash J.* **52**, 33–58 (2008).
25. Tang-Schomer, M. D., Johnson, V. E., Baas, P. W., Stewart, W. & Smith, D. H. Partial interruption of axonal transport due to microtubule breakage accounts for the formation of periodic varicosities after traumatic axonal injury. *Exp. Neurol.* **233**, 364–372 (2012).
26. Paonessa, F. *et al.* Microtubules deform the nuclear membrane and disrupt nucleocytoplasmic transport in Tau-mediated frontotemporal dementia. *Cell Rep.* **26**, 582–

593 (2019).

27. Straight, A. F., Sedat, J. W. & Murray, A. W. Time-lapse microscopy reveals unique roles for kinesins during anaphase in budding yeast. *J. Cell Biol.* **143**, 687–694 (1998).
28. Liang, W. H. *et al.* Microtubule Defects Influence Kinesin-Based Transport in Vitro. *Biophys. J.* **110**, 2229–2240 (2016).
29. Gramlich, M. W. *et al.* Single Molecule Investigation of Kinesin-1 Motility Using Engineered Microtubule Defects. *Sci. Rep.* **7**, 44290 (2017).
30. Kent, I. A., Rane, P. S., Dickinson, R. B., Ladd, A. J. C. & Lele, T. P. Transient pinning and pulling: A mechanism for bending microtubules. *PLoS One* **11**, 1–13 (2016).
31. Kabir, A. M. R. *et al.* Buckling of Microtubules on a 2D Elastic Medium. *Sci. Rep.* **5**, 1–12 (2015).
32. Vale, R. D. *et al.* Direct observation of single kinesin molecules moving along microtubules. *Nature* **380**, 451–453 (1996).
33. Woehlke, G. *et al.* Microtubule interaction site of the kinesin motor. *Cell* **90**, 207–216 (1997).
34. Vale, R. D. The molecular motor toolbox for intracellular transport. *Cell* **112**, 467–480 (2003).
35. Unpublished. (2019).
36. Cordes, T. & Blum, S. A. Opportunities and challenges in single-molecule and single-particle fluorescence microscopy for mechanistic studies of chemical reactions. *Nat. Chem.* **5**, 993–999 (2013).
37. Ando, T., Uchihashi, T. & Fukuma, T. High-speed atomic force microscopy for nano-visualization of dynamic biomolecular processes. *Prog. Surf. Sci.* **83**, 337–437 (2008).
38. Ando, T., Uchihashi, T. & Kodera, N. High-Speed AFM and applications to biomolecular systems. *Annu. Rev. Biophys.* **42**, 393–414 (2013).
39. Ando, T. High-speed atomic force microscopy and its future prospects. *Biophys. Rev.* **10**, 285–292 (2018).
40. Ando, T. *et al.* A high-speed atomic force microscope for studying biological macromolecules in action. *ChemPhysChem* **4**, 1196–1202 (2003).
41. Yamamoto, D. *et al.* High-Speed Atomic Force Microscopy Techniques for Observing Dynamic Biomolecular Processes. in *Methods in Enzymology* **475**, 541–564 (Elsevier Inc.,

2010).

42. Amos, L. A. & Baker, T. S. The three-dimensional structure of tubulin protofilaments. *Nature* **279**, 607–612 (1979).
43. Nogales, E., Whittaker, M., Milligan, R. A. & Downing, K. H. High-resolution model of the microtubule. *Cell* **96**, 79–88 (1999).
44. Bohm, K. J., Stracke, R. & Unger, E. Speeding up kinesin-driven microtubule gliding in vitro by variation of cofactor composition and physicochemical parameters. *Cell Biol. Int.* **24**, 335–341 (2000).
45. Keya, J. J. *et al.* High-Resolution imaging of a single gliding protofilament of tubulins by HS-AFM. *Sci. Rep.* **7**, 1–7 (2017).
46. Verbrugge, S., Van Den Wildenberg, S. M. J. L., Peterman, E. J. G. Novel ways to determine Kinesin-1's run length and randomness using fluorescence microscopy. *Biophys. J.* **97**, 2287–2294 (2009).
47. Ray, S., Meyhofer, E., Milligan, R. A. & Howard, J. Kinesin follows the microtubule's protofilament axis. *J. Cell Biol.* **121**, 1083–1093 (1993).
48. Schnitzer, M. J. & Block, S. M. Kinesin hydrolyses one ATP per 8-nm step. *Nature* **388**, 386–390 (1997).
49. Deriu, M. A. *et al.* Anisotropic elastic network modeling of entire microtubules. *Biophys. J.* **99**, 2190–2199 (2010).
50. Kononova, O. *et al.* Tubulin bond energies and microtubule biomechanics determined from nanoindentation in silico. *J. Am. Chem. Soc.* **136**, 17036–17045 (2014).
51. Schaap, I. A. T., Carrasco, C., de Pablo, P. J., MacKintosh, F. C. & Schmidt, C. F. Elastic response, buckling, and instability of microtubules under radial indentation. *Biophys. J.* **91**, 1521–1531 (2006).
52. Schaedel, L. *et al.* Microtubules self-repair in response to mechanical stress. *Nat. Mater.* **14**, 1156–1163 (2015).
53. Shibafuji, Y. *et al.* Single-molecule imaging analysis of elementary reaction steps of trichoderma reesei cellobiohydrolase i (Cel7A) hydrolyzing crystalline cellulose Iα and IIII. *J. Biol. Chem.* **289**, 14056–14065 (2014).
54. Nakamura, A. *et al.* Rate constants, processivity, and productive binding ratio of chitinase A revealed by single-molecule analysis. *Phys. Chem. Chem. Phys.* **20**, 3010–3018 (2018).

55. Cross, R. A. & McAinsh, A. Prime movers: the mechanochemistry of mitotic kinesins. *Nat. Rev. Mol. Cell Biol.* **15**, 257 (2014).
56. Arellano-Santoyo, H. *et al.* A tubulin binding switch underlies Kip3/Kinesin-8 depolymerase activity. *Dev. Cell* **42**, 37–51 (2017).
57. Peet, D. R., Burroughs, N. J. & Cross, R. A. Kinesin expands and stabilizes the GDP-microtubule lattice. *Nat. Nanotechnol.* **13**, 386–391 (2018).
58. Grant, B. J. *et al.* Electrostatically biased binding of kinesin to microtubules. *PLoS Biol.* **9**, e1001207 (2011).
59. Benoit, M. P. M. H., Asenjo, A. B. & Sosa, H. Cryo-EM reveals the structural basis of microtubule depolymerization by kinesin-13s. *Nat. Commun.* **9**, 1–13 (2018).
60. Moores, C. A. *et al.* A mechanism for microtubule depolymerization by KinI kinesins. *Mol. Cell* **9**, 903–909 (2002).
61. Tan, D., Rice, W. J. & Sosa, H. Structure of the kinesin13-microtubule ring complex. *Structure* **16**, 1732–1739 (2008).
62. Asenjo, A. B. *et al.* Structural model for tubulin recognition and deformation by kinesin-13 microtubule depolymerases. *CellReports* **3**, 759–768 (2013).
63. Reed, N. A. *et al.* Microtubule Acetylation Promotes Kinesin-1 Binding and Transport. *Curr. Biol.* **16**, 2166–2172 (2006).
64. Hancock, W. O. The kinesin-1 chemomechanical cycle: stepping toward a consensus. *Biophys. J.* **110**, 1216–1225 (2016).
65. Cross, R. A. Review: Mechanochemistry of the kinesin-1 ATPase. *Biopolymers* **105**, 476–482 (2016).
66. Castoldi, M. & Popov, A. V. Purification of brain tubulin through two cycles of polymerization-depolymerization in a high-molarity buffer. *Protein Expr. Purif.* **32**, 83–88 (2003).
67. Fujimoto, K. *et al.* Colocalization of quantum dots by reactive molecules carried by motor proteins on polarized microtubule arrays. *ACS Nano* **7**, 447–455 (2013).
68. Schindelin, J. *et al.* Fiji: an open-source platform for biological-image analysis. *Nat. Methods* **9**, 676–82 (2012).

Chapter 4

Effect of Stabilization of Microtubules by Cevipabulin on Microtubule Behavior and their Interaction with Kinesins

Abstract

Cevipabulin recently gaining attention as an important drug in treatment of Alzheimer's disease has the feature to stabilize microtubules. In this chapter, I attempt to evaluate the stabilization of microtubules by cevipabulin belonging to one of the least explored class of microtubule stabilizing agents, [1,2,4]triazolo[1,5-a]pyrimidines. I have investigated the change in mechanical properties of the cevipabulin-stabilized microtubules. The results showed that cevipabulin-stabilized microtubules were more flexible compared to that of the microtubules stabilized by paclitaxel, the most commonly used antimitotic microtubule stabilizing agent. Similar to the paclitaxel-stabilized microtubules, cevipabulin-stabilized microtubules could be driven by kinesins in an *in vitro* gliding assay. The velocity of cevipabulin-stabilized microtubules was significantly higher than that of paclitaxel-stabilized microtubules. This finding will enrich the variety of microtubules with difference in mechanical and dynamic properties and widen their applications in nanotechnology.

4.1. Introduction

Microtubule-stabilizing agent to stabilize microtubules are strategically important for therapeutic intervention in neurodegenerative diseases. [1,2] Microtubule is a cytoskeletal component that provides structure and spatial organization in eukaryotic cells. [3,4] The α- and β-tubulins form heterodimers and polymerize to form a hollow cylindrical structure of microtubule with an outer diameter of 25 nm. [5] Microtubules together with their associated motor proteins such as, kinesin and dynein participate in various biological processes like, growth, development and migration. [6–8] The dynamic structures of microtubules alternate between growing and shrinking phases. Therefore, the chemical compounds that interact with microtubules are also important chemotherapeutic agents for the treatment of cancer. Microtubule associated motor proteins move along microtubules by consuming chemical energy of adenosine triphosphate (ATP) with high efficiency compared to artificial machineries. [9] Due to such attractive features the microtubule-kinesin/dynein system are considered as building blocks of actuators for molecular robots and artificial muscle. [10–15] Microtubule stabilization has found usefulness in such applications as well.

So far, a naturally occurring drug, paclitaxel has been the most commonly used microtubule stabilizing agent. However, the limited sources, complex structures of this compound limit its synthesis and thereby, restrict its application. As a result, several small synthetic compounds, such as, triazolopyrimidines, [16] Synstab A, [17] phthalimide derivatives, [18] pyridazines, [19] have emerged as microtubule stabilizing agents. Of these, cevipabulin (5-chloro-6-[2,6-difluoro-4-[3-(methylamino)propoxy]phenyl]-N-[(2S)-1,1,1-trifluoropropan-2-yl]-[1,2,4]triazolo[1,5-a]pyrimidin-7-amine), from the

class of triazolopyrimidines is reported to stabilize microtubules in a way similar to and different from the way paclitaxel does. [16,20–22] Recently, it has attracted attention as starting points for central nervous system (CNS) drug development and in treatment of neurodegenerative diseases, for example, the Alzheimer's disease. [2,23] Therefore, understanding the effect of cevipabulin on mechanical and dynamic properties of microtubules would be beneficial in the aspects of physiological application as well as in nanotechnology.

Cevipabulin has been reported to exhibit oral bioavailability, metabolic stability and water solubility. [24] But their utility in artificial environment has not yet been verified. In this work, for the first time the cevipabulin-stabilized microtubules were observed using fluorescence microscopy. Finally, I have investigated the effect of cevipabulin on the mechanical and dynamic properties of the microtubules *in vitro*.

4.2. Results and Discussion

4.2.1. Microtubule stabilization using cevipabulin

Cevipabulin belongs to triazolopyrimidines, a series of small, synthetic molecules to promote tubulin polymerization. [24] Figure 4.1 shows the chemical structures of cevipabulin and that of naturally occurring complex paclitaxel molecule, the most commonly used antimitotic agent to stabilize microtubules.

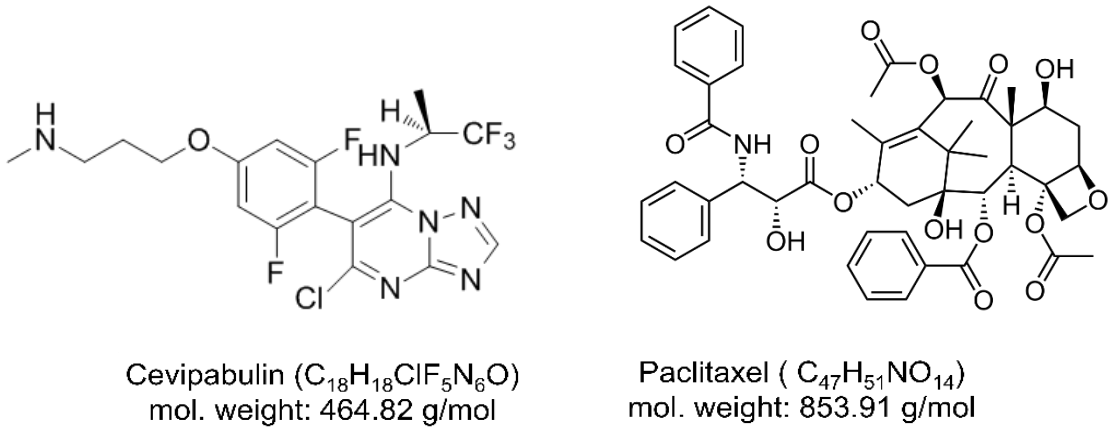

Figure 4.1. *Chemical structures of the microtubule stabilizing agents used in this study.* Chemical structures and molecular weights of cevipabulin and paclitaxel.

In order to stabilize microtubules, the microtubule stabilizing agents are classified to bind to the α-β tubulin dimer in three established drug domains: a) colchicine, b) taxoid, or c) vinca alkaloid sites. [25] Location of the binding sites on tubulins to which microtubule stabilizing drugs bind are shown in the 3-dimensional structure in Figure 4.2. Cevipabulin is reported to bind to the β-tubulin of microtubule like paclitaxel. [22] Paclitaxel binds to the intraluminal taxoid site on the β-tubulin in polymerized microtubule. The reports in favor of cevipabulin binding to the taxoid as well as the vinca alkaloid domain of β tubulin are available. [16] However, it is established that, cevipabulin does not compete with

paclitaxel for its binding to the taxoid site, rather vinblastine, a microtubule destabilizing agent. [22,24]

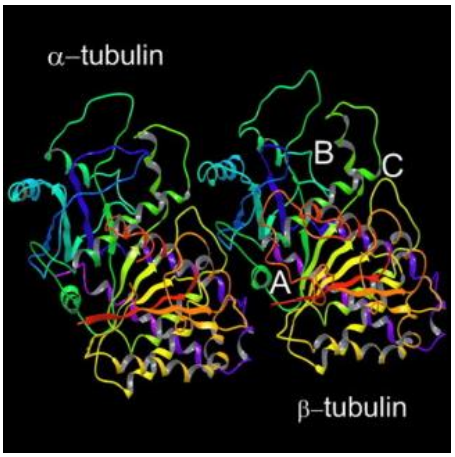

Figure 4.2. *Drug-binding sites in tubulin.* Three-dimensional model of α-β tubulin heterodimer showing microtubule stabilizing drug binding sites on α and β tubulins. The sites A, B and C denote the colchicine, taxoid, and vinca alkaloid sites, respectively.

To investigate the effect of cevipabulin on microtubule stabilization, fluorescent dye labelled tubulins were polymerized in to microtubules as described in the experimental section. The microtubules (5.6 µM) were mixed with cevipabulin (50 µM) and stored at room temperature. The fluorescence microscopy image of the fluorescent-labelled microtubules is shown in the Figure 4.3 (A), from which successful stabilization by cevipabulin was confirmed. For comparison paclitaxel-stabilized microtubules were also prepared fluorescence microscopy image of which is shown in 4.3 (B). Apparently, no considerable difference between cevipabulin and paclitaxel-stabilized microtubules was observed.

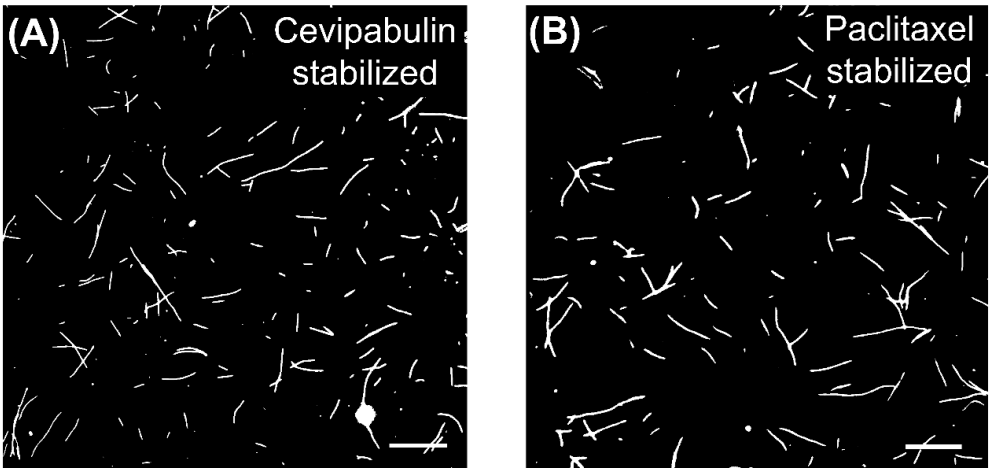

Figure 4.3. *Conditions of the stabilized microtubules.* Fluorescence microscopy images of microtubules stabilized using (A) cevipabulin and (B) paclitaxel. Concentration of tubulin for microtubule preparation was 5.6 µM and concentrations of both microtubule stabilizing agents were 50 µM. Scale bar: 10 µm.

To confirm the apparent similarity in microtubule condition further, the lengths of the microtubules were analyzed (Figure 4.4). The arithmetic average of length of microtubules stabilized by cevipabulin and by paclitaxel were found to be 10.2 ± 5.5 µm (n=174) and 10.4 ± 7.1 µm (n=161), respectively. The distribution of lengths of microtubules from two datasets were found to be not normally distributed from the results of tests for normal distribution (Anderson-Darling test, D'Agostino & Pearson test, Shapiro-Wilk test and Kolmogorov-Smirnov test). This was further validated from the fitting of the distributions to equation for Gaussian distribution as follows:

$$y = Ae^{\frac{-(x-b)^2}{c^2}} \quad \ldots\ldots\ldots\ldots (4.1)$$

here A, b and c represent height, center and variance of the fitted peaks, respectively. The fitting of the data gave low R^2 values Figure 4.4 (A,B).

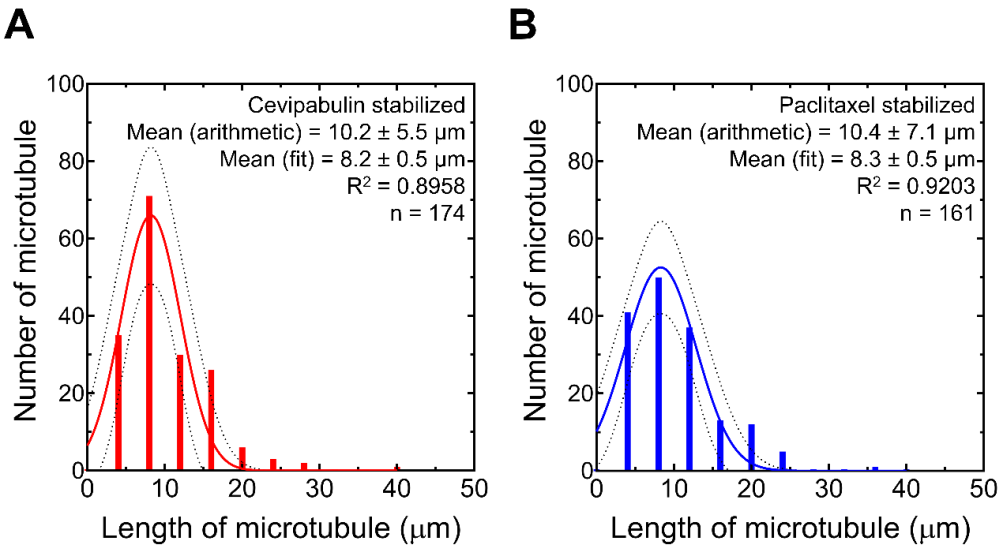

Figure 4.4. *Length distribution of the stabilized microtubules.* The histograms of distribution of lengths of the cevipabulin-stabilized microtubules (A) and the paclitaxel-stabilized microtubules (B). Bin size = 4 µm. The distributions of lengths were fitted to the Gaussian equation (equation 4.1). The fitted curves are represented by solid lines. The dotted lines indicate the deviation of the fitting. Arithmetic mean and mean from Gaussian fitting of the microtubule lengths are mentioned in the legends. The datasets did not pass the normality tests inferring that the data are not normally distributed which was also supported by the low R^2 values of the fits. Number of microtubules considered for analysis are mentioned in legends.

Since the microtubule lengths were not normally distributed, I performed the Mann-Whitney non-parametric U-test suitable for non-normal data to check the statistical significance of the difference between lengths of microtubules stabilized by cevipabulin and by paclitaxel. No significant difference in microtubule lengths was observed from Mann- Whitney test at $P < 0.01$ (Figure 4.5).

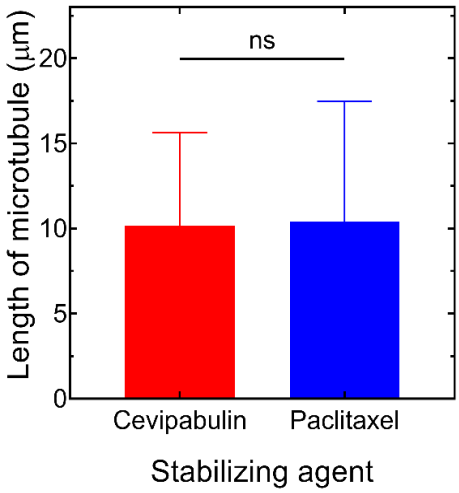

Figure 4.5. *Mean lengths of the stabilized microtubules.* Mean lengths of microtubules stabilized by cevipabulin and paclitaxel were not significantly different as obtained from the result of Mann-Whitney test at P< 0.01. P=0.7040. ns: non-significant. Error bar: standard deviation.

The polymerization of the microtubules from tubulins was carried out for the same duration of time (i.e. 30 minutes). The similar length distribution of microtubules stabilized using same treatment with cevipabulin and with paclitaxel may be indicative to the similarities between microtubule stabilization mechanism by the two drugs. [22]

4.2.2. Effect of time on the length of cevipabulin-stabilized microtubules

I investigated the effect of incubation time on the microtubules stabilized by the cevipabulin. Observation of same effect on the paclitaxel stabilized microtubules was made. The results are shown in the Figure 4.6. It was observed that in a given time the length of the microtubules stabilized by cevipabulin did not alter significantly whereas the length of microtubules stabilized by the paclitaxel became almost double upon incubation time of 24 hours.

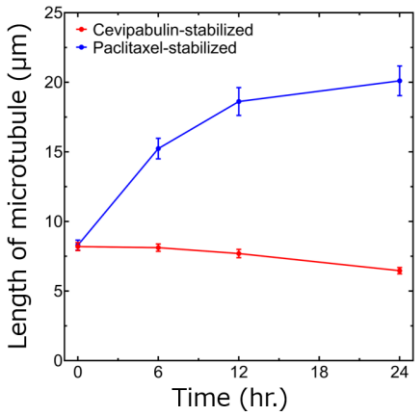

Figure 4.6. *Effect of incubation time on the lengths of the cevipabulin and paclitaxel-stabilized microtubules.* At 0,6,12, and 24 hours lengths of 174, 216, 100, 156 cevipabulin-stabilized microtubules and 161, 136, 102, 119 paclitaxel-stabilized microtubules were measured. Error bar: standard deviation.

4.2.3 Effect of stabilization by cevipabulin on the mechanical property of microtubules

Next, I investigated whether stabilization of microtubule by cevipabulin has any effect on their mechanical property. For this I estimated the persistence length of microtubules. It is the measure of the rigidity of microtubule at any constant temperature. To determine the persistence lengths of the two types of microtubules, end-to-end and contour lengths of microtubule were measured as done in literature. [26,27] The obtained data were fitted in the following equation:

$$R^2 = 2L_p^2[\frac{L}{L_p} - 1 + e^{\frac{L}{L_p}}] \quad \ldots\ldots\ldots\ldots\ldots\ldots (4.2)$$

where R is the mean squared end-to-end distance,

L is the contour length of a filament, and

L_p represents the persistence length of microtubule. The derived parameter from the fitting gave the values of persistence lengths.

The results of analysis of the persistence lengths of cevipabulin and taxol-stabilized microtubules are presented in the Figure 4.6. Fitting of the data to equation 4.2 gave that the persistence length of cevipabulin-stabilized microtubules was 59.8 ± 4.9 µm (n =174) whereas that of paclitaxel-stabilized microtubules was higher, 84.9 ± 4.8 µm (n =161). The higher value of persistence length of a filament refers to its higher rigidity.

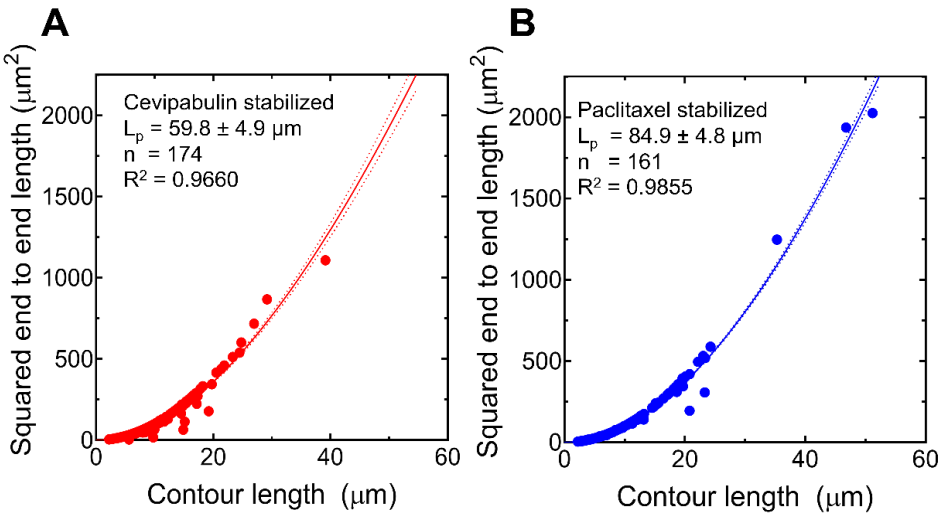

Figure 4.7. *Persistence lengths of the stabilized microtubules.* The persistence lengths of microtubules stabilized by cevipabulin (A) and paclitaxel (B). Solid lines are obtained from data fitted to the equation 4.2. Values of L_p and the goodness of fits are mentioned in the figure legends.

I performed the Student's t-test to check the statistical significance of the difference between persistence lengths of these two types of microtubules. It was found that the result is statistically significant at $P<0.0001$ (Figure 4.8).

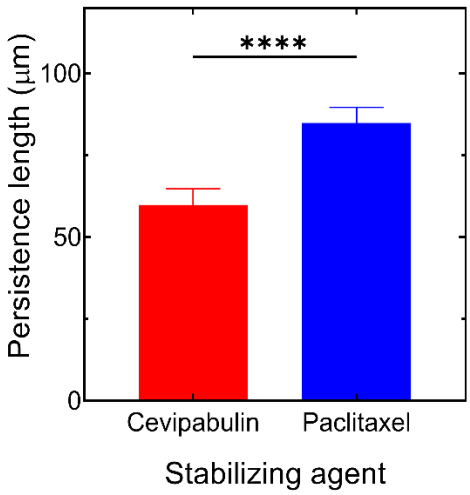

Figure 4.8. *Comparison of the persistence lengths of the microtubules stabilized by different drugs.* The persistence lengths of the microtubules stabilized by cevipabulin and paclitaxel as derived from the fitting in Figure 4.7. Statistical analysis by Student's t-test show significant difference between the two data sets at P<0.0001 indicated by ****. Error bar: standard deviation.

This result confirms that, stabilization by cevipabulin rendered microtubules more flexible compared to the paclitaxel-stabilized microtubules. The increased flexibility of the cevipabulin-stabilized microtubules may be explained by the binding of cevipabulin to β-tubulins at two binding sites, one being the same as where paclitaxel binds and the other, vinca alkaloid domain. [16]

4.2.4. Effect of stabilization by cevipabulin on the biochemical activity of microtubules

Finally, in order to investigate if the cevipabulin-stabilized microtubules retain their biochemical activity, an *in vitro* gliding assay on a kinesin coated substrate in presence of 5 mM ATP was performed. Time lapse fluorescence images from the gliding assay of cevipabulin-stabilized microtubules over 800 nM kinesin coated glass are shown in Figure 4.9 A. Figure 4.9 B shows the displacement of microtubules with time along their trajectories.

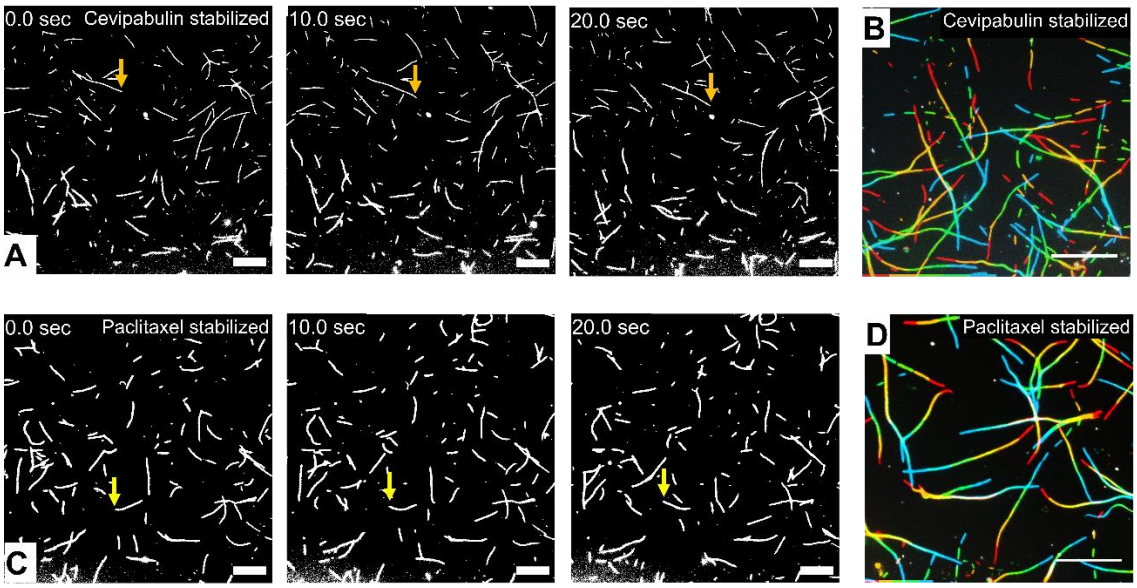

Figure 4.9. *Motility of the stabilized microtubules over kinesin coated substrate.* (A) Time lapse fluorescence microscopy images from the gliding assay of cevipabulin-stabilized microtubules over kinesin coated substrate. The movement of one representative gliding microtubule in three images are shown by the vertical arrows. Scale bar: 10 µm. (B) The change in position of cevipabulin-stabilized gliding microtubules at 10 second interval identified using ImageJ plugin 'color footprint'. 5 consecutive frames have been considered for this analysis. Here the red and blue color indicate the initial and final position of the microtubule at 10.0 sec and 50.0 sec., respectively. Scale bar: 10 µm. (C) Time lapse fluorescence microscopy images from the gliding assay of paclitaxel-stabilized microtubules over kinesin coated substrate. The movement of one representative gliding microtubule in three images are shown by the vertical arrows. Scale bar: 10 µm. (D) The change in position of paclitaxel-stabilized gliding microtubules at 10 second interval identified using ImageJ plugin 'color footprint'. 5 consecutive frames have been considered for this analysis. Here the red and blue color indicate the initial and final position of the microtubule at 10.0 sec and 50.0 sec., respectively. Scale bar: 10 µm.

From Figure 4.9 B, it is observed that all the microtubules stabilized with cevipabulin demonstrated gliding motion on the kinesin coated substrate similar to the paclitaxel-stabilized microtubules (Figure 4.9 D). This result confirms that stabilization of microtubules by cevipabulin has similar effect on the gliding behavior of microtubules

induced by kinesins.

Furthermore, the gliding velocities of the microtubules were analyzed (Figure 4.10 A-C). The velocities of cevipabulin and paclitaxel-stabilized microtubules were compared and both were found to be normally distributed (the D'Agostino & Pearson test and Shapiro-Wilk tests for normal distribution at alpha =0.01). The distributions were fitted to the Gaussian equation (equation 4.1). The average gliding velocities from the fitting were 703 ± 6 nm/s (n=30) and 486 ± 1 nm/s (n=30) for microtubules stabilized by cevipabulin and by paclitaxel, respectively. The difference in the velocity between these two types of microtubules was found to be statistically significant (Student's t-test, P<0.0001, Figure 4.9 C).

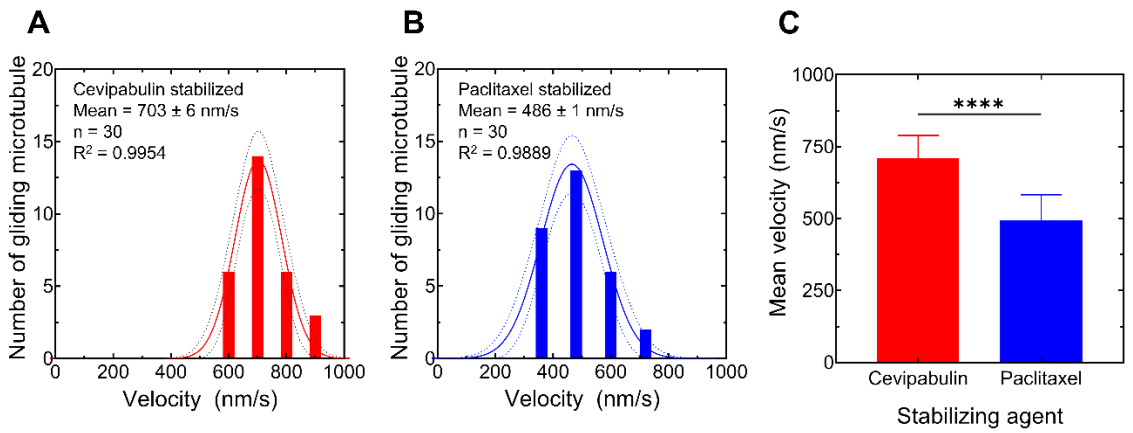

Figure 4.10. *Gliding velocities of the stabilized microtubules over kinesin coated substrate.* Distribution of velocities of gliding microtubules stabilized by 50 µM cevipabulin (A) and 50 µM paclitaxel (B). Bin size = 100 nm/s. The distributions of velocities were fitted to the Gaussian equation for normal distribution (equation 1). The fitted curves are represented by solid lines. The dotted lines indicate the deviation of the fitting. Mean velocities from the fitting, number of samples considered, and goodness of fit are mentioned in the legends. (C) Mean velocities of microtubules stabilized by cevipabulin and paclitaxel were significantly different as obtained from the result of Student's t-test at P< 0.0001 indicated by ****. Error bar: standard deviation.

This result suggests that the interaction of kinesins with cevipabulin-stabilized microtubules might be different from that with paclitaxel-stabilized microtubules.

Paclitaxel until now, is the only known microtubule stabilizing drug to increase microtubule flexibility. [28,29] Present report suggests that the microtubules stabilized by cevipabulin are more flexible than those by paclitaxel. Previous claims of cevipabulin showing similarities to paclitaxel and to vinblastine are available. [22,24] Paclitaxel binds to a hydrophobic cleft of the β-tubulin subunit and often induce the structuring of a key M loop to mediate lateral tubulin interactions in microtubules. [30] Whereas, the vinblastine binds to the β-tubulin subunit at the interdimer interface, to perturb longitudinal tubulin contacts and favor tubulin-tubulin association in a non-microtubule-like assembly fashion. [31] Since the interdimer tubulin-tubulin interaction is less strong than the intra-dimer tubulin-tubulin bond, [32,33] the difference in binding of cevipabulin and paclitaxel to the tubulin might be responsible for the increased flexibility.

4.3. Conclusion

In conclusion, the effect of cevipabulin on the mechanical properties and dynamics of microtubules was explored. Cevipabulin made the microtubules more flexible and increases their gliding velocity on kinesin coated substrate. Although paclitaxel is the most commonly used drug to stabilize microtubules, present results show similar stabilizing efficiency by cevipabulin. Moreover, the small cevipabulin molecules with simpler structure might prove to be more advantageous in tuning the mechanical properties of the microtubules. These findings will provide more opportunity to employ the microtubules in treating neurodegenerative diseases and cancers [2,23,34] as well as in nanotechnological applications [11,15].

4.4 Experimental procedures

4.4.1. Chemicals

All chemicals were purchased from Sigma unless mentioned otherwise. Cevipabulin was purchased from MedChemExpress.

4.4.2. Purification, labelling and polymerization of tubulin

Tubulin was purified from fresh porcine brain using a high-concentration PIPES buffer (1 M PIPES, 20 mM EGTA, 10 mM $MgCl_2$; pH adjusted to 6.8 using KOH). [35] ATTO 550 fluorescent dye labelled-tubulin was obtained following standard protocol. [36] Microtubule was polymerized from 56 μM tubulin (20% ATTO 550 labelled tubulin and 80% non-labelled tubulin) in BRB80 (80mM K-PIPES, 1mM $MgCl_2$, 1mM ethylene glycol-bis(β-aminoethyl ether)-N,N,N′,N′-tetraacetic acid (EGTA); pH 6.8) in presence of 5 mM Guanosine 5'-Triphosphate (GTP), 20 mM $MgCl_2$, 25% dimethyl sulfoxide at 37 °C for 30 minutes.

4.4.3. Stabilization of microtubules

The stock solutions of cevipabulin and paclitaxel were prepared using dimethyl sulfoxide as solvent. For microtubule-stabilization the polymerized microtubules (tubulin concentration 5.6 μM) and 50 μM stabilizing agents, paclitaxel or cevipabulin were mixed in BRB80.

4.4.4. Fluorescence microscopy

Samples were illuminated with a 100 W mercury lamp (Intensilight, C-HGFIE, Nikon) and observed by epi-fluorescence microscope (Eclipse Ti; Nikon) equipped with an oil-

coupled Plan Apo 60×1.40 objective (Nikon). Filter block with UV-cut specification (TRITC: EX540/25, DM565, BA606/55; Nikon) was used in the optical path of the microscope to separate the excitation light from the fluorescence and eliminate harmful effect of UV irradiation on samples. Images were captured using a complementary metal-oxide semiconductor (CMOS) sensor camera (Neo sCMOS; Andor). Neutral density or ND filters were used on the microscope eliminate photobleaching. The microscope sample stage position, shutters, filter wheels and camera were controlled using software NIS- Elements BR (version 4.50, Nikon). Movies of the gliding microtubules were captured with a frame interval of 10 seconds.

4.4.5. Data analysis

The fluorescence images were analyzed by NIS- Elements BR software (Nikon) and Fiji 1.52 J software (National Institutes of Health, USA). Gliding velocities were measured using the ImageJ plugin *MTrackJ*. Figures 4.9 B and D, showing positions of the microtubules with time were generated using the ImageJ plugin *color footprint*. Statistical analyses were performed with Prism 8 (GraphPad). Two-tailed Student's t-test or Mann-Whitney tests were carried out to compare two groups of data where appropriate.

4.5. Results of Statistical Analysis

Statistical analysis of all data mentioned in this chapter were carried out using the software GraphPad Prism 8.1.0. Below are mentioned the results of all relevant analysis in the sequence as they appear in the chapter.

Table 4.5.1. Results of test for Normal distribution of the lengths of microtubules stabilized by cevipabulin and those by paclitaxel. Following are the results from tests that were carried out (Figure 4.5).

Anderson-Darling test		
A2*	4.323	5.687
P value	<0.0001	<0.0001
Passed normality test (alpha=0.01)?	No	No
P value summary	****	****
D'Agostino & Pearson test		
K2	71.77	111.5
P value	<0.0001	<0.0001
Passed normality test (alpha=0.01)?	No	No
P value summary	****	****
Shapiro-Wilk test		
W	0.8813	0.7956
P value	<0.0001	<0.0001
Passed normality test (alpha=0.01)?	No	No
P value summary	****	****
Kolmogorov-Smirnov test		
KS distance	0.1340	0.1402
P value	<0.0001	<0.0001
Passed normality test (alpha=0.01)?	No	No
P value summary	****	****
Number of values	174	161

Table 4.5.2. Test for statistical significance of difference between the lengths of cevipabulin-stabilized microtubules and paclitaxel-stabilized microtubules using Mann-Whitney test (Figure 4.6).

Column B	Paclitaxel-stabilized
vs.	vs.
Column A	Cevipabulin-stabilized
Mann Whitney test	
P value	0.7040
Exact or approximate P value?	Approximate
P value summary	ns
Significantly different (P < 0.01)?	No
One- or two-tailed P value?	Two-tailed
Sum of ranks in column A,B	29569 , 26711
Mann-Whitney U	13670
Difference between medians	
Median of column A	8.800, n=174
Median of column B	8.980, n=161
Difference: Actual	0.1800
Difference: Hodges-Lehmann	-0.2100

Table. 4.5.3. Test for statistical significance of difference between the persistence lengths of cevipabulin-stabilized microtubules and paclitaxel-stabilized microtubules using Student's t- test (Figure 4.8).

Column B	Paclitaxel-stabilized
vs.	vs.
Column A	Cevipabulin-stabilized
Unpaired t test	
P value	<0.0001
P value summary	****
Significantly different (P < 0.01)?	Yes
One- or two-tailed P value?	Two-tailed
t, df	t=47.06, df=333
How big is the difference?	
Mean of column A	59.84
Mean of column B	84.85
Difference between means (B - A) ± SEM	25.01 ± 0.5315
99% confidence interval	23.63 to 26.39
R squared (eta squared)	0.8693
F test to compare variances	
F, DFn, Dfd	1.029, 173, 160
P value	0.8565
P value summary	ns
Significantly different (P < 0.01)?	No
Data analyzed	
Sample size, column A	174
Sample size, column B	161

Table. 4.5.4. Results of test for Normal distribution of the velocities of microtubules stabilized by cevipabulin and those by paclitaxel. Following are the results from tests that were carried out (Figure 4.10 A,B).

Test for normal distribution		
Anderson-Darling test		
A2*	1.307	0.6838
P value	0.0018	0.0666
Passed normality test (alpha=0.01)?	No	Yes
P value summary	**	ns
D'Agostino & Pearson test		
K2	2.860	2.948
P value	0.2393	0.2290
Passed normality test (alpha=0.01)?	Yes	Yes
P value summary	ns	ns
Shapiro-Wilk test		
W	0.9014	0.9331
P value	0.0106	0.0594
Passed normality test (alpha=0.01)?	Yes	Yes
P value summary	*	ns
Kolmogorov-Smirnov test		
KS distance	0.2313	0.1355
P value	0.0004	>0.1000
Passed normality test (alpha=0.01)?	No	Yes
P value summary	***	ns
Number of values	30	30

Table. 4.5.5. Test for statistical significance of difference between the velocities of cevipabulin-stabilized microtubules and paclitaxel-stabilized microtubules using Student's t- test (Figure 4.10 C).

Column B	Paclitaxel-stabilized
vs.	vs.
Column A	Cevipabulin-stabilized
Unpaired t test	
P value	<0.0001
P value summary	****
Significantly different (P < 0.01)?	Yes
One- or two-tailed P value?	Two-tailed
t, df	t=9.773, df=57
How big is the difference?	
Mean of column A	709.4
Mean of column B	493.1
Difference between means (B - A) ± SEM	-216.3 ± 22.13
99% confidence interval	-275.3 to -157.3
R squared (eta squared)	0.6263
F test to compare variances	
F, DFn, Dfd	1.269, 29, 28
P value	0.5311
P value summary	ns
Significantly different (P < 0.01)?	No
Data analyzed	
Sample size, column A	30
Sample size, column B	30

4.6. References

1. Lee, V. M., Daughenbaugh, R. & Trojanowski, J. Q. Microtubule stabilizing drugs for the treatment of Alzheimer's disease. *Neurobiol. Aging* **15 Suppl 2**, S87-9 (1994).
2. Brunden, K. R., Trojanowski, J. Q., Smith, A. B., Lee, V. M. Y. & Ballatore, C. Microtubule-stabilizing agents as potential therapeutics for neurodegenerative disease. *Bioorganic Med. Chem.* **22**, 5040–5049 (2015).
3. Wang, N., Butler, J. P. & Ingber, D. E. Mechanotransduction across the cell surface and through the cytoskeleton. *Science* **260**, 1124–1127 (1993).
4. Stamenović, D., Mijailovich, S. M., Tolić-Nørrelykke, I. M., Chen, J. & Wang, N. Cell prestress. II. Contribution of microtubules. *Am. J. Physiol. Physiol.* **282**, C617–C624 (2013).
5. Amos, L. A. & Baker, T. S. The three-dimensional structure of tubulin protofilaments. *Nature* **279**, 607–612 (1979).
6. B. Alberts, A. Johnson, J. Lewis, M. Raff, K. Roberts, P. W. *Molecular biology of cell*. (Garland Science, New York, 2008).
7. Scholey, J. M., Sharp, D. J. & Rogers, G. C. Microtubule motors in mitosis. *Nature* **407**, 41–47 (2000).
8. Cai, P. *et al.* Nanoparticles strengthen intracellular tension and retard cellular migration. *Nano Lett.* **14**, 83–88 (2014).
9. Gennerich, A. & Vale, R. D. Walking the walk: how kinesin and dynein coordinate their steps. *Curr. Opin. Cell Biol.* **21**, 59–67 (2009).
10. U, H. H. & Vogel, V. Molecular shuttles based on motor proteins : active transport in synthetic environments. 67–85 (2001).
11. Hess, H., Bachand, G. D. & Vogel, V. Powering Nanodevices with Biomolecular Motors. *Chem. - A Eur. J.* **10**, 2110–2116 (2004).
12. Van Den Heuvel, M. G. L. & Dekker, C. Motor proteins at work for nanotechnology. *Science* **317**, 333–336 (2007).
13. Keya, J. J. *et al.* DNA-assisted swarm control in a biomolecular motor system. *Nat. Commun.* **9**, 4–11 (2018).
14. Inoue, D. *et al.* Sensing surface mechanical deformation using active probes driven by motor proteins. *Nat. Commun.* **7**, 12557 (2016).
15. Matsuda, K. *et al.* Artificial Smooth Muscle Model Composed of Hierarchically Ordered Microtubule Asters Mediated by DNA Origami Nanostructures. *Nano Lett.* **19**, 3933–3938 (2019).

16. Sáez-Calvo, G. *et al.* Triazolopyrimidines Are Microtubule-Stabilizing Agents that Bind the Vinca Inhibitor Site of Tubulin. *Cell Chem. Biol.* **24**, 737-750.e6 (2017).
17. Haggarty, S. J. *et al.* Dissecting cellular processes using small molecules: Identification of colchicine-like, taxol-like and other small molecules that perturb mitosis. *Chem. Biol.* **7**, 275–286 (2000).
18. Li, P.-K. A thalidomide analogue with in vitro antiproliferative, antimitotic, and microtubule-stabilizing activities. *Mol. Cancer Ther.* **5**, 450–456 (2006).
19. Lamberth, C. *et al.* Synthesis and fungicidal activity of tubulin polymerisation promoters. Part 2: pyridazines. *Bioorg. Med. Chem.* **20**, 2803—2810 (2012).
20. Beyer, C. F. *et al.* TTI-237: A novel microtubule-active compound with in vivo antitumor activity. *Cancer Res.* **68**, 2292–2300 (2008).
21. Lou, K. *et al.* Brain-penetrant, orally bioavailable microtubule-stabilizing small molecules are potential candidate therapeutics for Alzheimer's disease and related tauopathies. *J. Med. Chem.* **57**, 6116–6127 (2014).
22. Beyer, C. F. *et al.* The microtubule-active antitumor compound TTI-237 has both paclitaxel-like and vincristine-like properties. *Cancer Chemother. Pharmacol.* **64**, 681–689 (2009).
23. Ballatore, C., Brunden, K. R., Trojanowski, J. Q., Lee, V. M. Y. & Smith, A. B. Non-Naturally Occurring Small Molecule Microtubule-Stabilizing Agents: A Potential Tactic for CNS-Directed Therapies. *ACS Chem. Neurosci.* **8**, 5–7 (2017).
24. Zhang, N. *et al.* Synthesis and SAR of [1,2,4]Triazolo[1,5-a]pyrimidines, a Class of Anticancer Agents with a Unique Mechanism of Tubulin Inhibition. *J. Med. Chem.* **50**, 319–327 (2007).
25. Stanton, R. A., Gernert, K. M., Nettles, J. H. & Aneja, R. Drugs that target dynamic microtubules: A new molecular perspective. *Med. Res. Rev.* **31**, 443–481 (2011).
26. Rashedul Kabir, A. M. *et al.* Formation of ring-shaped assembly of microtubules with a narrow size distribution at an air-buffer interface. *Soft Matter* **8**, 10863–10867 (2012).
27. Arii, Y. & Hatori, K. Relationship between the flexibility and the motility of actin filaments: effects of pH. *Biochem. Biophys. Res. Commun.* **371**, 772–776 (2008).
28. Dye, R. B., Fink, S. P. & Williams, R. C. Taxol-induced flexibility of microtubules and its reversal by MAP-2 and Tau. *J. Biol. Chem.* **268**, 6847–6850 (1993).
29. Kawaguchi, K. & Yamaguchi, A. Temperature dependence rigidity of non-taxol stabilized single microtubules. *Biochem. Biophys. Res. Commun.* **402**, 66–69 (2010).
30. Prota, A. E. *et al.* Molecular mechanism of action of microtubule-stabilizing

anticancer agents. *Science* **339**, 587–590 (2013).
31. Gigant, B. *et al.* Structural basis for the regulation of tubulin by vinblastine. *Nature* **435**, 519–522 (2005).
32. Gebremichael, Y., Chu, J.-W. & Voth, G. A. Intrinsic Bending and Structural Rearrangement of Tubulin Dimer: Molecular Dynamics Simulations and Coarse-Grained Analysis. *Biophys. J.* **95**, 2487–2499 (2008).
33. Grafmüller, A. & Voth, G. A. Intrinsic bending of microtubule protofilaments. *Structure* **19**, 409–417 (2011).
34. Zhou, J. & Giannakakou, P. Targeting microtubules for cancer chemotherapy. *Curr. Med. Chem. Anticancer. Agents* **5**, 65–71 (2005).
35. Castoldi, M. & Popov, A. V. Purification of brain tubulin through two cycles of polymerization-depolymerization in a high-molarity buffer. *Protein Expr. Purif.* **32**, 83–88 (2003).
36. Peloquin, J., Komarova, Y. & Borisy, G. Conjugation of fluorophores to tubulin. *Nat. Methods* **2**, 299–303 (2005).

Chapter 5

Conclusion

In this thesis I have presented the *in vitro* studies on the effect of deformation of microtubule on the interaction between the microtubules and their associated motor proteins. The effect of the buckling deformation on dynein-driven quantum dot transportation has been investigated. The alteration in single kinesin molecule transportation as an effect of the bending of microtubule is observed using the high-speed atomic force microscopy. How the stabilization of microtubules by a novel drug can alter their mechanical properties as well as their interaction with kinesins *in vitro* is investigated.

In chapter 2, I addressed how the microtubules respond to the compressive stress applied along the longitudinal axis of the microtubules. The microtubules undergo buckling at different compressive strains which resembles an important indispensable cellular event in living organism. The effect of the buckling deformation of the microtubules on their biophysical roles were validated by monitoring the dynein-driven Quantum dot (Qdot) transportation along the buckled microtubules. I unveiled that the dynein-based transportation is accelerated due to the buckling of microtubules. An anomalous drop in the velocity of the transportation observed at a characteristic range of compressive strain indicating a clear distinction between the dynein-microtubule interaction at lower compressive strain and higher compressive strains. This finding clearly reflects that the microtubules may serve as mechanotransducer. The affinity of the Qdot conjugated dyneins for microtubules did not change regularly as a function of the applied compressive strain. The results suggest that the basis for mechano-regulation of

cellular processes by microtubules may be formed by the mechano-kinetic preference of associated proteins for mechanically deformed microtubules. This work would benefit the current understanding of mechano-functional properties of cytoskeletal soft materials and their involvement in mechano-regulation of cellular activities.

In chapter 3, I realized the visualization of single kinesins transporting along microtubule with high spatio-temporal resolution using the high-speed atomic force microscopy. I developed a method to cause bending of microtubule in an *in vitro* environment by tuning the substrate conditions. The technique enabled me to observe the movements of single kinesins along the microtubule protofilaments. It was found that the motility of the kinesins was dependent on the curvature of the microtubule as the track. The binding affinities of kinesin to the undeformed and the deformed microtubules were determined and found to differ significantly. Higher binding affinity of the kinesins to the deformed microtubules than that to the undeformed microtubule show direct indication of altered interaction between kinesin and deformed microtubule. An alteration in microtubule-motor interaction by bending may provide understanding of how microtubules serve as mechanotransducers in cell.

In chapter 4, I explored the application of an alternative microtubule-stabilizing agent, cevipabulin. This synthetic microtubule stabilizing agent which is strategically important in the treatment of neurodegenerative diseases was found to exhibit microtubule binding properties similar to and different from paclitaxel, the most common antimitotic drug. I found that, cevipabulin softens the microtubules and increases their gliding velocity on kinesin coated substrate when compared with the paclitaxel-stabilized microtubules. Therefore, the study shows the possibility that

cevipabulin molecules with simpler molecular structure may be more advantageous in tuning the mechanical properties of the microtubules.

This dissertation describes how modification of microtubule either due to mechanical deformation or by introduction of non-conventional stabilizing agents may alter the properties of the microtubules. The compressive stress induced deformation of microtubules modulated their interaction with dyneins as observed from the altered dynamics of dynein-driven transportation along microtubules. The single kinesin molecule transportation along the straight and the bent microtubules revealed that the bending of microtubule without causing any lattice defects on the structure may induce the kinesin transportation dynamics. This knowledge would help our current understanding on how mechanical deformation of microtubules may modulate the motor protein based intracellular transportation in cells. This study is important particularly for the neurons where mechanical stress induced modulation of intracellular transportation is involved. The altered interaction between the microtubules and its associated motor proteins observed due to the application of varied microtubule-stabilizing agent may prove to essential in providing more opportunity to employ the microtubules in treating neurodegenerative diseases and cancers.

Therefore, this study presents knowledge for developing rational design principle for nature-inspired mechanoresponsive functional material with physiological and nanotechnological applications.

List of Publication

Related to Chapter 4

Nasrin, S. R., Kabir, A.M.R., Konagaya, A., Ishihara, T., Sada, K. and Kakugo, A., Stabilization of Microtubules by Cevipabulin, *Biochem. Biophys. Res. Commun., accepted*

Related to Chapter 2

Nasrin, S. R., Kabir, A.M.R., Sada, K. and Kakugo, A., *to be submitted*

Related to Chapter 3

Nasrin, S. R., Sada, K. and Kakugo, A., *to be submitted*

List of Conference Presentations

Conference (related to this dissertation)

1. Syeda Rubaiya Nasrin, Arif Md. Rashedul Kabir, Kazuki Sada, Akira Kakugo, "Microtubule Deformation has Effect on Cargo Transportation by Motor Proteins", 9th CSE (Chemical Sciences and Engineering) Summer School, Hokkaido University 2018, 15-16 July 2018, Jozenkei, Sapporo, Japan.
2. Syeda Rubaiya Nasrin, Arif Md. Rashedul Kabir, Kazuki Sada, Akira Kakugo, "Microtubule Buckling Affects Cargo Transportation by Molecular Motor", 1st International Conference on 4D Materials and Systems, Gel Symposium, 2018, 26-30 August, Yamagata University, Yonezawa, Yamagata, Japan.
3. Syeda Rubaiya Nasrin, Arif Md. Rashedul Kabir, Kazuki Sada, Akira Kakugo, "Deformation of Microtubule by External Mechanical Stress Affect its Functionality Asymmetrically", 6th International Symposium on Ambitious Leader's Program for Fostering Future Leaders to Open New Frontiers in Materials Science, Hokkaido University, 2018, 29-31 October, Hokkaido, Japan.
4. Syeda Rubaiya Nasrin, Arif Md. Rashedul Kabir, Kazuki Sada, Akira Kakugo, "Microtubule Deformation by External Stimuli Affects its Functionality", Learning Satellite Program 2018 Hokkaido University, 2018, 11-19 November, University of Strasbourg, Strasbourg, France,
5. Syeda Rubaiya Nasrin, Arif Md. Rashedul Kabir, Kazuki Sada, Akira Kakugo, "Mechanobiology in Intracellular Cargo Transportation: Effect of Deformation of Microtubule on Dynein-based Cargo Transportation", 1st Glowing Polymers Symposium, 2018, 15 December, Tokyo, Japan.
6. Syeda Rubaiya Nasrin, Arif Md. Rashedul Kabir, Kazuki Sada, Akira Kakugo, "Microtubule: Can they serve as a mechanotransducer?", 8th Conference on Exploring Next-Generation Materials Science and Nanoscience (CENG-MSM) 2019, 12-14 January, Niseko, Hokkaido, Japan.
7. Syeda Rubaiya Nasrin, Arif Md. Rashedul Kabir, Kazuki Sada, Akira Kakugo, "Effect of Mechanical Deformation of Microtubule by External Stimuli on Microtubule-Dynein

Interaction", 2nd Asian-French Workshop on Polymer Science 2019, (CSE international student symposium 2019), 18-21 July, Hokkaido University, Hokkaido, Japan.

Conference (not related to this dissertation)

1. Syeda Rubaiya Nasrin, First National Conference of Bangladesh Crystallographic Association, 5 December 2013, Nabab Nawab Ali Chowdhury Senate Bhaban, University of Dhaka.
2. Syeda Rubaiya Nasrin, International seminar on "Application of Novel Functional Materials", 14 December 2013, Conference Room, Centre for Advanced Research in Sciences (CARS), University of Dhaka
3. Syeda Rubaiya Nasrin, Kumkum Ahmed, M. Yousuf A. Mollah, Md. Abu Bin Hasan Susan, Study of Physico-chemical Properties of [EMIM][TFSI] Ionic Liquid Based Binary Systems with Polar Solvents, 36th Annual Conference Bangladesh Chemical Society, 1 March 2014, Hajee Mohammad Danesh Science and Technology University, Dinajpur, Bangladesh.
4. Syeda Rubaiya Nasrin, M. Yousuf A. Mollah, Md. Abu Bin Hasan Susan, Physico-chemical Properties of Binary Mixtures of an Imidazolium-based Ionic Liquid and Molecular Solvents, 37th Annual Conference of Bangladesh Chemical Society, 11 April 2015, Comilla University, Comilla, Bangladesh

List of Figures

Chapter 3

Chapter 4

Acknowledgments

I have always aspired for this moment when I get to acknowledge the forces that kept me advancing through this life-changing journey of obtaining the Ph.D.

To begin with, I acknowledge the opportunity to join the Doctoral Course in Hokkaido University as a *MEXT* scholar. My sincere regards go to my supervisor *Professor* Kazuki Sada for the support and guidance he had provided to me during my entire journey of acquiring the degree. I especially acknowledge his encouragement during the time of my preparation and submission of the thesis.

My humble gratitude to the *Associate Professor, Material Chemistry Laboratory, HU*, Dr. Akira Kakugo, for so many things, starting from my selection as a Ph. D. student in this lab to until training me as a qualifying applicant for the degree. I thank him for his trust, inspiration and the philosophy he has acquainted me to.

I also thank *Assistant Professors* Dr. Kento Kokado (*MCL, HU*) and Dr. Kenji Hirai (*now, Associate Professor, Laboratory of Nanomaterials and Nanoscopy, HU)* for their fruitful discussion during the regular meetings. I am grateful for having received advice from Dr. Arif Md. Rashedul Kabir, *Assistant Professor, MCL, HU,* in my research from time to time.

My thankful regards to Professor Takayuki Uchihashi and Dr. Christian Ganser (*Laboratory of Biomolecular Dynamics and Function, Nagoya University)* for their kind assistance with the High-speed atomic force microscopy observations (Chapter 3). Dr. Christian has been so patient to resolve my endless queries. I acknowledge *Prof.* Akihiko Konagaya (*Department of Computational Intelligence and Systems Science, Tokyo Institute of Technology*) and Dr. Tsukasa Ishihara (*Biomedical Research Institute, National Institute of Advanced Industrial Science and Technology*) for their helpful discussion on Cevipabulin related research (Chapter 4).

I acknowledge my root, *Dhaka University,* specifically, the *Material Chemistry Research Laboratory, Department of Chemistry.* I have been enough lucky to be taught and groomed by a great group of mentors; *Prof.* M. Yousuf Ali Mollah, *Prof.* Md. Abu Bin Hasan Susan, *Associate Professors* Dr. Md. Mominul Islam, Dr. Muhammed Shah Miran and Assistant Professor Dr. Saika Ahmed (also an *HU* graduate!). I am grateful to Prof. Susan, my supervisor during Masters' for introducing me to my Ph.D. supervisor.

I would like to take this opportunity to thank Dr. Tanjina Afrin for teaching me the ins and outs of the research in my present lab. I was lucky to be surrounded and guided by the *DU* and *HU* alumni: Dr. Sirajul Islam (*Kansai University*), Dr. Tamanna Ishrat Farhana (*Kyoto University)* and Dr. Jakia Jannat Keya (*HU*).

Japan came to me with many differences- not only as a place but also with a new environment, language, and lifestyle. Had I not received the utmost support from my fellow lab members, the differences would never fade out. I remember the kind help of Kentaro Kayano (right from Day 1!). Thanks to Nishikawa Seiji for being a kind friend inside and outside the lab. It was comforting to have Dr. Jakia around: evidence that showed, the Ph.D. life *can* be survived! I thank *Senpai* Dr. Shizuka Anan for her kind advice with the ever-smiling face. My best wishes with thanks to the upcoming Drs.: Kyohei Uenishi, Soukurou Sunaga, Masami Naya, Takashi Machida, Mousumi Akter, Farhana Afroze, Satsuki Ishii, Mst. Rubaya Rashid. Also, to Naoki Fukaya, Ayano Michibata, Xinmeng Wang, Tokiyo Katou, Yuma Tanaka, Kento Matsuda, Kouta Mishima, Danqing Yu, Tasrina Munmun, Hiroki Amaya, Akira Kabasawa, Miwa Kubota, Yugo Tsunoda, Masato Yamashita. I am grateful to all for the moments they have spent to support me, including all the smiles, thumbs-ups, and great laughs we shared.

I also thank the staff of different offices of *HU* I have interacted with regarding my endless academic and administrative issues, especially Ms. Mari Igarashi from the *OIAS, HU*.

On a personal note, I have a few more people to express my gratitude to. I feel blessed to have found the friends who were no less than a family to me during my stay in Sapporo. First is Dr. Shazia Sharmin Satter (*Fukuoka lab, HU*) for her kind support and guidance from even before I got here and of course for the 24-hour access to her home during my initial days (*literally*)! I am also grateful to Assistant Prof. Dr. SMA Hakim Siddiki and Dr. Abeda Sultana Touchy (*Shimizu lab, HU*) for allowing me to feel the warmth of their kind hearts!

The position I have reached now is all because of the endless support, inspiration, and sacrifices of the best parents in the world, my *abbu* Syed Mahfizur Rahman and *ammu* Syeda Nasreen Ara Begum. I am indebted for the values they put in me and grateful for the dream they helped me achieve. Thanks to my awesome siblings: Syed Hasibul Ahsan, Syeda Sumaiya Nasrin, my sister-in-law Shegufta Ahmed for their support. I look forward to meeting the newest part of my family, Amayra.

Last but not least, I cannot thank enough for the support, trust, patience, and love from my husband, Md. Fahad Rahman Khan.

I have been extremely lucky to always have my family by my side emotionally. I feel sorry for not being around much. But I promise I will try my best to mark my presence on the earth making all the sacrifices worth!

Syeda Rubaiya Nasrin